The Dissertation Committee for Jason Edward Hill
certifies that this is the approved version of the following dissertation:

One-dimensional Electron Systems on Graphene Edges

Committee:

Allan H. MacDonald, Supervisor

Qian Niu

Zhen Yao

Jack B. Swift

Lorenzo Sadun

One-dimensional Electron Systems on Graphene Edges

by

Jason Edward Hill, Bs.Sc. Physics

Dissertation

Presented to the Faculty of the Graduate School of

The University of Texas at Austin

in Partial Fulfillment

of the Requirements

for the Degree of

Doctor of Philosophy

The University of Texas at Austin

December 2007

To my mom, Agnes, who prayed for me before I was, and has poured herself out all her life so that I would have opportunities that she could not:

O Lord, You have searched me and known me.
You know when I sit down and when I rise up;
You understand my thoughts from afar.
You thoroughly search my path and my lying down,
And You know all my ways.
For a word is not yet on my tongue,
And, O Jehovah, already You know it completely.
You have closed me in, behind and before
And have laid Your hand on me.
O wonderful knowledge to me! It is so high; I cannot attain to it.

Where shall I go, away from Your Spirit,
And where shall I flee from Your presence?
If I ascend into heaven, You are there;
If I make my bed in the lowest pit, there You are.
If I take the wings of the dawn and settle at the limits of the sea,
There also Your hand will lead me, even Your right hand will hold me.
And if I say, "Surely darkness will hid me,
And the light around me will be as night";
Even the darkness is not dark, and night shines like day to You;
The darkness is like the light to You.

For it was You who formed my inward parts;
You wove me together in my mother's womb.
I will praise You, for I am awesomely and wonderfully made;
Your works are wonderful, And my soul knows it well.
My frame was not hidden from You when I was made in secret,
Skillfully fashioned in the depths of the earth.
Your eyes saw my unformed substance;
And in Your book all of them were written:
The days that were ordained for me,
When not one of them had yet passed.

And how precious are Your thoughts to me, O God!
How great is the sum of them!
If I should count them, they would be more than the sand.
When I awake, I am still with You.
Psalm 139:1–18

Acknowledgments

It has been an honor to work with and know my advisor Allan MacDonald. In deep gratitute, thanks is given for all the patience and guidance provided in this work. His enthusiasm for condensed matter physics and a positive attitude are contagious and truly a pattern for his students.

I also thank the MacDonald group for helping me to learn that the best way to go on in most endeavors is by being in a group with everyone functioning in their best way. Emiliano Papa, who introduced me to theoretical condensed matter physics. Janice Trinidad, for spying out the land before meand recommending the group. Hongki Min and Tami Pereg-Barnea helped much in correcting my mistakes and were patient with my ignorance. Yafis Barlas, always willing to talk and teach me the subtleties of theoretical physics and Sahu about DFT. Ion, Jeil, and Maria, always learning and asking good questions. Murat Taş, always keeping me sharp and well informed. And of course, Becky Drake who always looks out for us. I am especially full of gratitute toward Nikolai Sinitsyn, who never gave up on me and found a place where I could enter into the work. Much of this work would truly have not been possible without his guidance and insight. Thanks to the rest of the Ph.D. students and post-docs and collaborators in the work. I would also like to thank Dr. Alex de Lozanne, my TA advisor and briefly research advisor over a summer. Greg Sitz for recommending condensed matter theory. My undergraduate mentors Vic Montemayor in pedagogy, and Ron Henderson in research and my many

teachers thoughout the years.

In many ways the unwavering support of my friends, family and the church have made this possible. I would especially like to thank the church in Austin for taking care of the needs of my entire being and teaching me how to eat Christ and to know my human spirit. All of the open homes and open hearts have shepherded me more than I know. Christ as my life supply and the practical church-life have become a bright shining light to my path. I cannot but thank and praise the Lord for His wonderful provision for me and for leading me in the next step of attending the FTTA bible school in Anahiem, CA though the support of the church. I came to Austin for my degree and myself; I leave for the Lord because of those who were faithful to the end and taught me to live a life with no regrets. Johnny Melton, always a friend. My step-dad and mom, Mr. and Mrs. Steven C. Meredith have always been my safety net and have provided a home for me to return to and a future to appreciate.

Jason Edward Hill

The University of Texas at Austin
December 2007

One-dimensional Electron Systems on Graphene Edges

Publication No. _____

Jason Edward Hill, Ph.D.
The University of Texas at Austin, 2007

Supervisor: Allan H. MacDonald

In this dissertation several aspects of one-dimensional edge states in graphene are studied. First, a background in the history and development of graphitic forms is presented. Then some novel features found in two-dimensional bulk graphene are presented. Here, some focus is given to the chiral nature of the Dirac equation and the symmetries found in graphene. Magnetism and interactions in graphene is also briefly discussed. Finally, the graphene nanoribbon with its two typical edges: armchair and zigzag is introduced. Gaps due to finite-size effects are studied. Next, the problem of determining the zigzag ground state is presented. Later, we develope this in an attempt to add the Coulomb interaction to the zigzag flat-band states. These nanoribbons can be simulated with a tight-binding code on a lattice model in which many different effects can be added, including an A/B sublattice asymmetry,

spin-orbit coupling and external fields. The lowest Landau level solutions in the different ribbon orientations is of particular current interest. This is done in the context of understanding new physics and developing novel applications of graphene nanoribbon devices.

Adding spin-orbit coupling to a graphene ribbon Hamiltonian leads to current carrying electronic states localized on the sample edges. These states can appear on both zigzag and armchair edges in the semi-infinite limit and differ qualitatively in dispersion and spin-polarization from the well known zigzag edge states that occur in models that do not include spin-orbit coupling. We investigate the properties of these states both analytically and numerically using lattice and continuum models with intrinsic and Rashba spin-orbit coupling and spin-independent gap producing terms. A brief discussion of the Berry curvature and topological numbers of graphene with spin-orbit coupling also follows.

Contents

List of Tables

List of Figures

Chapter 1

Graphitic Forms

1.1 Introduction

Inasmuch as the ages of human history are rather objectively labeled by the wide-spread use of certain materials, the opening up of the use of a new material, such as graphene (a single layer of graphite), has possibly wide-spread implications. The stone, bronze, iron and steel ages have passed, and from the point of view of micro-electronics this is certainly the age of silicon. There has been a growing desperation to develop technologies using other materials to supplement silicon and to meet modern society's increasing need and appetite for fast, efficient and cheap micro-electronics. One class of materials of increasing interest are graphitic materials, which are constituted with carbon, the atom of life. Broadly speaking, graphitic materials are crystals of carbon atoms that have a structure derived from a planar honeycomb lattice of carbon atoms (AKA graphene, see Tab. 1.1). From a material science point of view we have already entered into the age of carbon, where carbon fibers are widely used to reinforce plastics and concrete along side silicates. In fact, the most immediate application for graphene is probably its use in composite materials.[1] Carbon-silicon polymers have been developed to produce flexible and

resilient materials such as silicone. This development of using silicon-organic material combinations to gain advances may be mirrored in the fields of microelectronics and nanotechnology in the not-too-distant future. By this prospect, a compelling case can be made for the study of graphitic materials from the perspective of applications.

Condensed matter physics is the study of the various properties and emergent phenomena found in systems of a liquid or solid state due to the structure and the collective (or many-bodied) behavior of its constituents. From the perspective of condensed matter physics the study of graphitic materials is an interesting problem in and of itself. Each type of crystalline material can be thought of as a different universe with its own laws of physics governing its own "fundamental" particles, e.g. quasi-particles. A honeycomb lattice of strongly bonded carbon atoms allows for a truly two-dimensional structure in an atomic sense, as realized first in fullerenes (1985), then carbon nanotubes (1991), and now graphene (2004). Interestingly, the low energy quasi-particles in graphene behave as massless relativistic particles, so all the machinery of two-dimensional quantum electrodynmics (QED) can be brought to bear on the problem. Low dimensional condensed matter physics has always been a profitable arena full of interesting problems, peculiar physics and now the truly atomically flat two-dimensional system or graphene avails itself for study.

What is graphene?

> Imagine a piece of paper but a million times thinner. This is how thick graphene is. Imagine a material stronger than diamond. This is how strong graphene is. Imagine a material more conducting than copper. This is how conductive graphene is. Imagine a machine that can test the same physics that scientists test in, say, CERN, but small enough to stand on top of your table. Graphene allows this to happen. Sounds like a magic? Indeed: sometimes, even I cannot believe that this is true.

> Having such a material in hand, one can easily think of many useful things that can eventually come out. As concerns new physics, no one doubts about it already... *Andre Geim.*

[2]

From a simple model (see Section 1.6.1) undoped graphene is shown to be a zero band-gap semiconductor and to have a linear spectrum over a relatively wide energy range. Hence, the density of states varies strongly with energy. In fact the carriers behave in a way analogous to particles in a two dimensional relativistic universe with the speed of light reduced by a factor of about 300. This analogy is useful and has been further developed along many lines, e.g. the Dirac equation and chirality. This kind of "relativistic" electron gas is remarkably different from that found in conventional semiconductors with a quadratic band structure. As a result the quantum Hall effect (QHE) in graphene is of a different character (a half integer quantization) and can be even observed up to room-temperature! Wide-spread use of graphene-based electronic maybe a few decades off, but graphene shows promise in its use as a field-emitter, a mechanically and chemically active probe and even in battery technology. An extremely weak spin-orbit coupling and the absence of hyperfine interaction in ^{12}C-graphene make it an excellent if not ideal material for making spin qubits. This guarantees graphene-based quantum computation to become an active research area.[1]

Furthermore, single-walled nanotubes (SWNTs) and the states along the physical edge of graphene flakes and ribbons provided novel one-dimensional electron systems. The SWNTs provide a model system for the conventional one-dimensional Luttinger liquid theory. The graphene edge states, however, are more peculiar and are potentially useful in spintronic applications, which utilize the spin degree of freedom of the electrons. Devices have been proposed based on a spin Hall effect in graphene using these edge states.[106] Also the possibility of having a quantum Hall

ferromagnet in graphene seems quite likely. Manufacturing conventional transistors, spin-valves and superconducting field-effect transistor devices are obvious research targets that may involve edge physics.[1] Determining the ground state of these edge states with interactions and in an applied field is also currently a topic of much interest. In short, graphene is not only a potentially useful new material, but it also provides fundamentally new kinds of problems for low-dimensional condensed matter physics.

1.2 The Bonding of Carbon Atoms

Carbon (C) is the atom of life. The richness of organic chemistry comes from the various kinds of bondings that carbon makes with itself and other atoms. Carbon's unique chemistry is illustrated by the fact that it forms a larger number of compounds than the sum total of all other elements combined. To understand the structure and properties of graphitic materials, the bonding of carbon atoms is discussed first. Carbon is the sixth element of the periodic table and is listed at the top of column IV, ranks twelfth in order of natural abundance and has two stable isotopes with atomic weights 12 (98.9% abundance) and 13 (1.1% abundance) and hence an average of 12.0115 amu. A carbon atom has six electrons and the electronic structure of a free atom is $1s^2 2s^2 2p^2$ with the two p electrons having the same spin (a total spin of unity) in the lowest energy configuration by Hund's rule. See figure 1.1. In a carbon atom with six electrons, two strongly bound core electrons fill the deeply confined $1s^2$ orbital, and the remaining four valence electrons occupy the $2s^2 2p^2$ orbitals. In the crystalline phase the valence electrons give rise to $2s$, $2p_x$, $2p_y$, and $2p_z$ orbitals which form the covalent binds in carbon materials. [3, 4]

When the energy difference between two atomic orbitals is small compared to the bonding energy, such as the $2s$ and the three $2p$ atomic orbitals in carbon, they can form hybridized orbitals to allow different bonding symmetries when forming

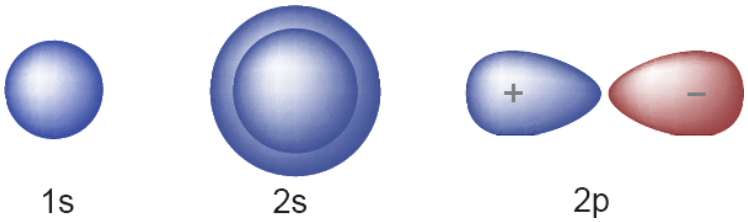

Figure 1.1: A cartoon of the electron densities in carbon's atomic orbitals. Positive phase amplitude is indicated by blue and negative by red. Adapted from [5]

molecules and crystals.[6] This hybridization is a mixing of the electronic wavefunctions that enhances the binding energy of the carbon atom with its neighboring atoms. The mixing of a single $2s$ electron with n = 1,2,3 $2p$ electrons is called sp^n hybridization. Other group IV elements exhibit primarily sp^3 hybridization. Carbon is different because there are no nearby inner atomic orbitals, since the $1s$ orbital is relatively deep compared to the valence electrons. This accounts for carbon's unique organic chemistry.[4, 7]

In carbon, three possible hybridizations occur: sp^3, sp^2 or sp. The formation of the sp hybridized orbital is shown in figure 1.2. In the sp hybridization shown, a linear combination is formed of the $2s$ orbital and the $2p_x$ orbital. Two orthonormal hybridized sp orbitals, denoted by $|sp_a\rangle$ and $|sp_b\rangle$, are expressed as linear combinations of the $|2s\rangle$ and $|sp_x\rangle$ wavefunctions,

$$\begin{aligned} |sp_a\rangle &= \frac{1}{\sqrt{2}}\left(|2s\rangle + |2p_x\rangle\right) \\ |sp_b\rangle &= \frac{1}{\sqrt{2}}\left(|2s\rangle - |2p_x\rangle\right). \end{aligned} \tag{1.1}$$

In diamond all four valence electrons form the sp^3 hybrid orbital with tetragonal

symmetry. The sp^3 hybridized orbitals explicitly are as follows:

$$\begin{aligned}
\left|sp_a^3\right\rangle &= \frac{1}{2}\left(|2s\rangle + |2p_x\rangle + |2p_y\rangle + |2p_z\rangle\right) \\
\left|sp_b^3\right\rangle &= \frac{1}{2}\left(|2s\rangle - |2p_x\rangle - |2p_y\rangle + |2p_z\rangle\right) \\
\left|sp_c^3\right\rangle &= \frac{1}{2}\left(|2s\rangle - |2p_x\rangle + |2p_y\rangle - |2p_z\rangle\right) \\
\left|sp_d^3\right\rangle &= \frac{1}{2}\left(|2s\rangle + |2p_x\rangle - |2p_y\rangle - |2p_z\rangle\right). \qquad (1.2)
\end{aligned}$$

In graphite three of the valence electrons form the sp^2 hybrid orbital with planar trigonal symmetry and the remaining electron is by convention a $2p_z$ orbital. The sp^2 hybridized orbitals explicitly are as follows:

$$\begin{aligned}
\left|sp_a^2\right\rangle &= +\frac{1}{\sqrt{3}}|2s\rangle - \frac{2}{\sqrt{3}}|2p_y\rangle \\
\left|sp_b^2\right\rangle &= +\frac{1}{\sqrt{3}}|2s\rangle + \frac{1}{\sqrt{2}}\left|2p_x^2\right\rangle + \frac{1}{\sqrt{6}}|2p_y\rangle \\
\left|sp_c^2\right\rangle &= -\frac{1}{\sqrt{3}}|2s\rangle - \frac{1}{\sqrt{2}}|2p_x\rangle + \frac{1}{\sqrt{6}}|2p_y\rangle. \qquad (1.3)
\end{aligned}$$

[7, 4] See figures 1.3 and 1.4.

With carbon there are two bonding configurations: sigma and pi bonds. A covalent chemical bond is formed between two atoms when their orbitals overlap and share a pair of electrons. When the orbitals overlap in phase (out of phase) along an axis between the atoms, i.e. the orbitals overlap in an end-to-end fashion, they form a sigma bond (sigma antibond) denoted by $\sigma(\sigma^*)$. For a $\sigma(\sigma^*)$ bond the electron density is highest (lowest) in the space between the atoms. The $2s$ and $2p$ orbitals as well as the sp^3 and sp^2 hybrid orbitals undergo σ bonding. Additionally, p orbitals can overlap in a sideway manner. When the orbitals overlap in phase (out of phase) in an side-to-side fashion, they form a pi bond (pi antibond) denoted by $\pi(\pi^*)$. [8] See figure 1.5.

Ethene and benzene are two molecules that illustrate sp^2 bonds. Ethene

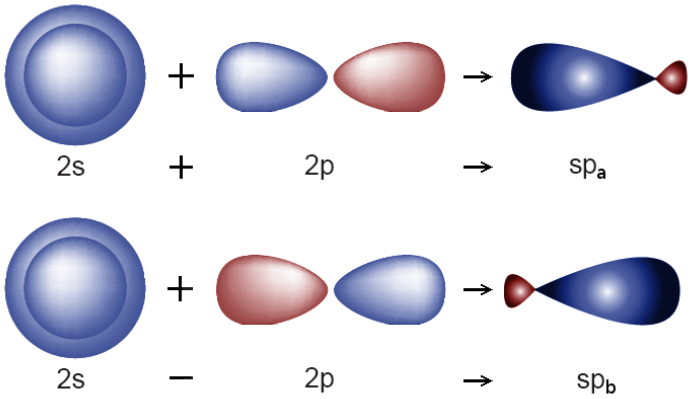

Figure 1.2: The formation of the *sp* hybridized orbitals such as found in acetylene HC≡CH. Adapted from [4] and [5]

(C_2H_4) has a double bond between the carbons, which consists of one σ bond from the head-on overlap of the two sp^2 orbitals and one π bond from the sideways overlap of the two $2p_z$ orbitals. Note that the π bond consists of two parts above and below the axis of the molecule. The four hydrogen bonds result from the overlap of the other carbon sp^2 orbitals with the hydrogen $1s$ orbitals. The overall shape of the molecule is planar (flat), with H-C-H and H-C-C bond angles of approximately 120°, see figure 1.6. Second is benzene (C_6H_6), a ring of six carbon atoms with three double bonds shared equally among them. This illustrates how the $2p_z$ orbital can lead to the delocalized carriers in graphene. The six $2p_z$ orbitals are all parallel to one another, and each contains one electron. Therefore there are three π bonds, but since there is no reason to prefer one configuration over the other (as is the case with the resonance structures) those three π bonds are delocalized over the whole molecular ring; see figure 1.7.[10, 9]

Carbon bonding allows for different kinds of crystals, even with different dimensionalities. In three dimensions there is diamond and graphite. In two dimensions a single monolayer of graphite is graphene. A rolled up monolayer or

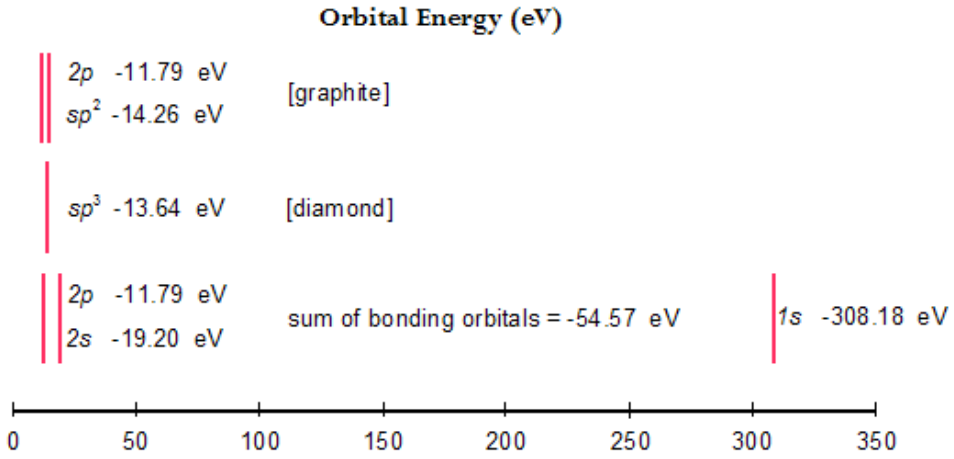

Figure 1.3: The orbital energies of carbon.

multilayer of graphite gives a carbon nanotube which has a one-dimensional character. A sheet of graphite formed into a ball is fullerene, which can be said to be "zero-dimensional"; see table 1.1.

It is remarkable how strikingly different diamond is from the graphitic forms of carbon. In diamond, the four valence electrons occupy the sp^3 hybridized orbital, which has tetragonal symmetry. Each carbon atom has four nearest neighbors to which it is bonded by σ bonds, separated by a distance of 1.5445 Å. The bond

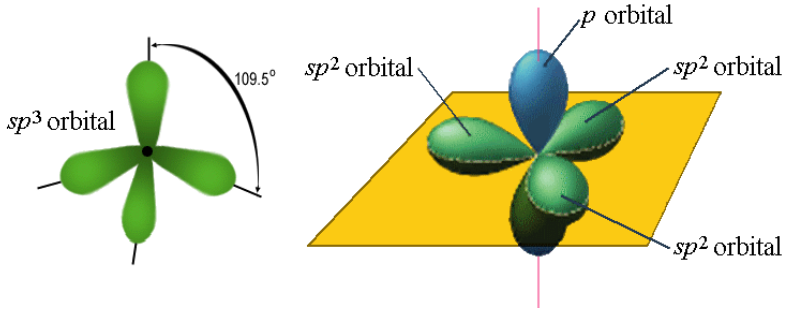

Figure 1.4: The sp^3 [diamond] and sp^2 [graphite] hybridized orbitals. Adapted from [8] and [9]

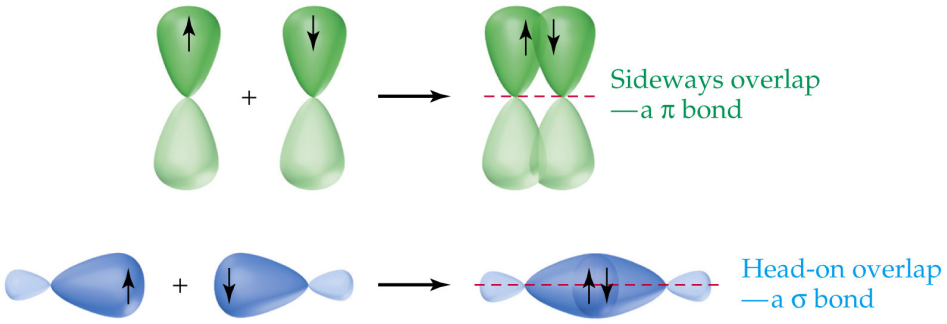

Figure 1.5: An illustration of the π bonding between two $2p_z$ orbitals and the σ bonding between two hybridized sp^2 orbitals. Figure taken from [10]

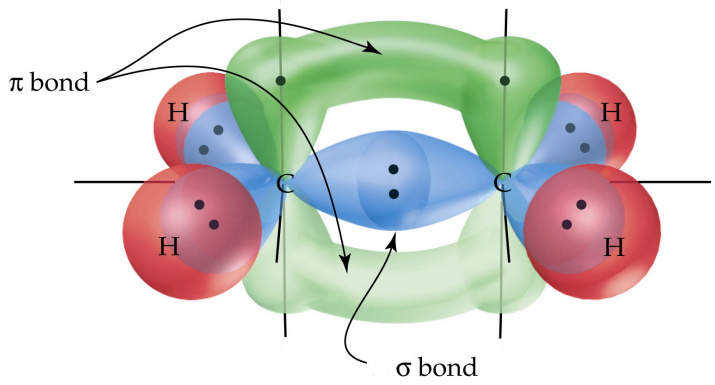

Figure 1.6: An illustration of σ and π bonding in ethene (C_2H_4). Figure taken from [10]

angles are all 109°, typical of sp^3 hybridization, see figure 1.4. The resulting three-dimensional interlocking structure constituted with only the stronger σ bonds makes diamond the hardest material known. Since there are no delocalized π bonds, diamond is electrically insulating. Diamond is transparent to visible light, with a high index of refraction and an unusually high thermal conductivity.[7, 11, 8]

Dimension	Material	Orbital	Bonding	Picture
3D	diamond	sp^3	σ only	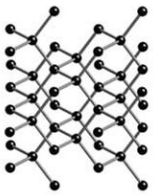
3D	graphite	sp^2	σ, π, van der Walls	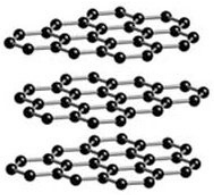
2D	graphene	sp^2	σ, π	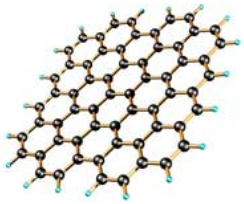
1D	CNTs	sp^2 (deformed)	more σ, less π	
0D	fullerenes	sp^2 (deformed)	more σ, less π	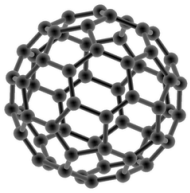

Table 1.1: The crystals of carbon.

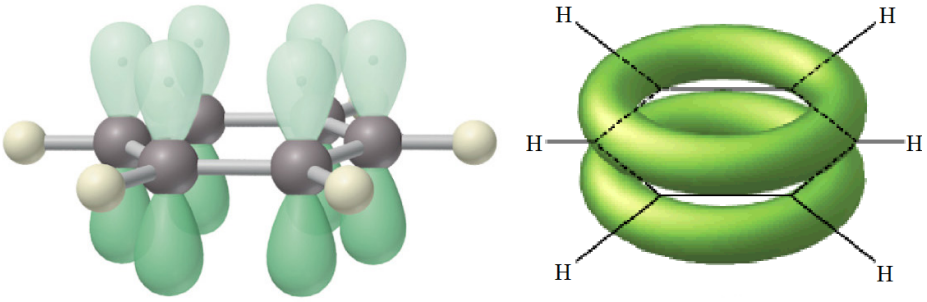

Figure 1.7: An illustration of the delocalized π bonds in benzene. Figure adapted from [10] and [9]

1.3 Graphite: Three-dimensional Carbon

1.3.1 The History of Graphite

Graphite is an allotrope of carbon, known also on occasion as *black lead* or *plumbago*, from Latin *plumbago* "acts like lead". From the earliest times this black lustrous mineral as been employed sometimes in ornaments, a strategic resource, a lubricant; but chiefly, because of its ability to mark surfaces, as a writing material. Natural graphite is found on nearly every continent and the crystalline perfection of these natural deposits varies widely from a nearly amorphous isotropic material to highly oriented graphite with isolated flakes up to $\sim$ 0.5 cm in diameter and $\sim$ 0.1 cm thick.[3]

Carbon black and soot are composed of extremely small crystals of imperfect (amorphous) graphite. Carbon black is produced by burning hydrocarbons in the absence of air, while soot is made in the presence of air. Coal is graphitic in the sense that it contains fused benzene rings, with the eventual stable metamorphosis product being graphite, i.e. graphite is the highest grade of coal. Coke is amorphous graphite prepared by heating coal in the absence of air, and it is used to make iron.

These crude forms of graphite have been known about and used since ancient times.

The history of natural graphite begins in the carboniferous era from about 354 to 290 million years ago which was characterized by forests of gigantic ferns, trees, and grasses covered vast swamp lands. The decay of the great forests yielded, under sedimentary pressure over time, the coal deposits common throughout the Earth. Not so common are the graphite seams formed by more extremes of pressures, and sometimes heat was also applied to remove all moisture content. The first graphite ever known to be discovered was found on the side of the mountain Seathwaite Fell in Borrowdale, near Keswick, England in 1564. The popular story is that, following a very violent storm, the shepherds went out in the morning to see their sheep on the mountain side and found a number of trees had been blown down tearing away the subsoil as they fell and leaving exposed to view large masses of black material. These same shepherds immediately put the black material to good use by marking their sheep.[12]

The value of the material was quickly discovered and the mines were taken over by the English government during Queen Elizabeth I's reign. The pure graphite of the Borrowdale mines was the only such deposit ever found, and its value was found to be fantastic. It was mined only six weeks a year; armed guards escorted the wagons to London; and export of the ore was prohibited. Although it was found most useful for medicinal purposes, its chief use, due to its high melting point and ease to carve, was as molds for the manufacture of cannon balls. So early on, graphite became a strategic resource.[12]

Graphite's most familiar application is as the 'lead' in pencils. The Romans first used a lead stylus to make a very light mark. Graphite left a darker mark than lead so it was called *plumbago*, but was so soft and brittle that it required a holder. The deposit of graphite found at Borrowdale was so solid and uniform that it could be sawn into sheets and then cut into thin square sticks. At first, the

sticks of graphite were wrapped in string. Later, the English Guild of Pencilmakers hand-carved wooden cases for the writing sticks, and enjoyed a world monopoly on the first wood-cased pencils.[12]

The first mass-produced pencils were made in Nuremberg, Germany in 1662. In 1779, K.W. Scheele made a chemical analysis of plumbago that proved it to be a form of carbon, not of lead. The present name *graphite* was coined 1789 by the German mineralogist Abraham Gottlob Werner from the Greek verb $\gamma\rho\alpha\varphi\epsilon\iota\eta$ "to write or draw".[12] Ironically, the author is from Shelbyville, TN, a small industrial town known as "The Pencil Capital of the World." The mills there processed the local hard cedar tree wood that is ideal for making pencils and shipped it to the German pencil factories. When these shipments ceased because of World War I (1917-18), Shelbyville got into the pencil business itself using British graphite. After the Empire-Berol company moved to Shelbyville it invested in the research to develop the different grades of graphitic pencil lead used in modern mechanical pencils. The author's father worked as a manager there.

Naturally occurring graphite can be purified, but generally contain substantial impurities. There are two prevalant ways to make artificial graphite that have been developed though the centuries. The older way is Acheson graphite and the newer is highly oriented pyrolytic graphite. Acheson graphite is made artificially with a wide range of crystalline perfections and properties. It is manufactured from processed coke. The final graphitization procedure is carried out at $\sim 3000^{\circ}$C in an Acheson furnace, which utilizes a conducting coke bed to heat the material over a period of 15 days.[3]

Acheson artificial graphite finds use as a matrix and moderator within nuclear reactors. Its low neutron cross section also recommends it for use in proposed fusion reactors. In 1939 the first report of fission (of uranium) was reported. In World War II (1939-45) the initial application that was envisaged was an explosive of

unprecedented power, and both Allied and Axis powers mobilized their scientists and engineers to that end. At the National Research Council (NRC) in Ottawa, Canada in 1940 George Laurence started experiments with uranium and a graphite moderator aimed at producing a chain reaction. Had his materials been purer, he might have achieved this first. On December 2, 1942, at the University of Chicago, Enrico Fermi first initiated a self-sustaining nuclear chain reaction, and controlled it by using machined graphite and graphitic bricks.[14] It was found that care must be taken that reactor-grade graphite is free of neutron absorbing materials such as boron, widely used as the seed electrode in commercial graphite deposition systems– this caused the failure of the Nazi Germany's World War II graphite-based nuclear reactors. Since they could not isolate the difficulty they were forced to use far more expensive heavy water moderators.[13]

The second kind of artificial graphite is pyrolytic graphite. The main imperfection in pyrolytic graphite is the occasional presence of cross-linking carbon bonds between the graphitic basal planes. Carbon fibers and cloth are prepared by heating textiles like rayon. At low temperatures, the textile fiber pyrolyzes, i.e. it decomposes into carbon and gas by-products. At higher temperatures, the carbon becomes graphitized. This produces carbon fibers (AKA pyrolytic carbon) that have great strength and are also used in composites such as carbon-fiber-reinforced epoxy plastic used in aircraft parts, golf clubs, fishing rods, etc. The cross-sectional structure of carbon-fibers resembles tree rings or a carrot. Carbon cloth is used in spacecraft to dissipate atmospheric heat. In 1962, efforts to develop a new bulk synthetic form of carbon with properties approaching single crystal graphite led to the development of highly oriented pyrolytic graphite (HOPG) by Ubbelohde and co-workers.[16] HOPG is formed by cracking a hydrocarbon at high temperature and subsequent heat treatment, often combined with the application of pressure. The resulting material is highly oriented along the c-axis (orientational deviations less

than 1°) but in the layer planes consists of a randomly ordered aggregate of small crystallites of $\sim$ 1 mm average diameter separated by regions with translational and rotational disorder.[17] Most of the experimental studies to date still rely on HOPG material. HOPG only mimics the perfect arrangement found in true single crystals.[82] HOPG is an ideal benchmark material for carbon fibers and a useful cleavable and cleanable substrate for microscopy probes.[4] One of the first scanning tunneling microscope (STM) images was of graphite, see figure 1.8. In STM images of HOPG graphite, there are two possible images. The image normally obtained looks like a hexagonal close-packed array; in this array, each atom is surrounded by six nearest neighbors. The distance between any two of these atoms is 2.46 Å, thus some asymmetry cause only every other atom to be imaged distinctly. Under ideal conditions, particularly if the probe tip is truly a single atom, you will see the honeycomb structure that shows the hexagonal rings that are the real structure of graphite; the center to center atomic distance in this image is 1.415 Å. HOPG is also often used as a substrate for organic samples in atomic force microscopy (AFM).

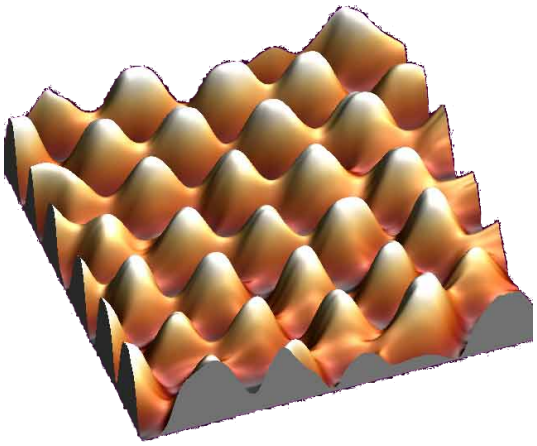

Figure 1.8: An STM scan of HOPG graphite with only half of the surface atoms clearly imaged, from [18].

1.3.2 The Ideal Structure and Characteristics of Graphite

Graphite holds the distinction of being the most stable form of solid carbon under standard conditions with an energy difference between graphite and diamond of ~ 0.02 eV per atom. Due to the high energetic barrier between the two phases of carbon, the transition from diamond to the most stable phase of graphite at normal conditions is extremely slow, but this transition can also occur more rapidly at high temperature, see figure 1.9. Due to the high anisotropy in the graphite structure as compared to that of diamond, the electronic, mechanical and optical properties of these two phases of carbon are very different. The electron mobility in diamond is only 1800cm^2/V-s were as the in-the plane graphite electron mobility is 20×10^3 cm^2/V-s. The band gap in diamond is 5.47 eV while in semi-metallic graphite is only -0.04 eV.

Graphite is a stacked structure of planes, where each plane is a hexagonal lattice of Carbon atoms. A basal plane is the plane that is perpendicular to the principal axis (c axis) in a tetragonal or hexagonal structure. A basal plane in graphite is constructed of a planar hexagon network, constituted by a honeycomb lattice of sp^2 hybridized carbons. Several of the basal planes stack with some specific order relative to neighboring planes; in this way the graphite lattice structure is defined. Bonds between Carbon atoms in the plane are σ and π bonds from the hybridized sp^2 orbitals that produce an effective C-C bond length of $d_{CC} = 1.422$ Å and results in 120° bond angles and the lattice unit vector $a = 2.463$ Å, see figure 1.10. These bonds are very short and extremely strong (420 kcal/mol) in the plane (bonds in diamond are longer at 1.54 Å). Therefore, a graphitic basal plane is stronger than diamond. An isolated graphitic plane is known as *graphene*, and it has longer bonds with $d_{CC} = 1.44$ Å and $a = 2.49$ Å. The remaining $2p_z$ electron plays a role in the interplanar bonding (this longer σ-like bond is very weak) and forms the co-planar π bonds which are delocalized, hence providing a donor site

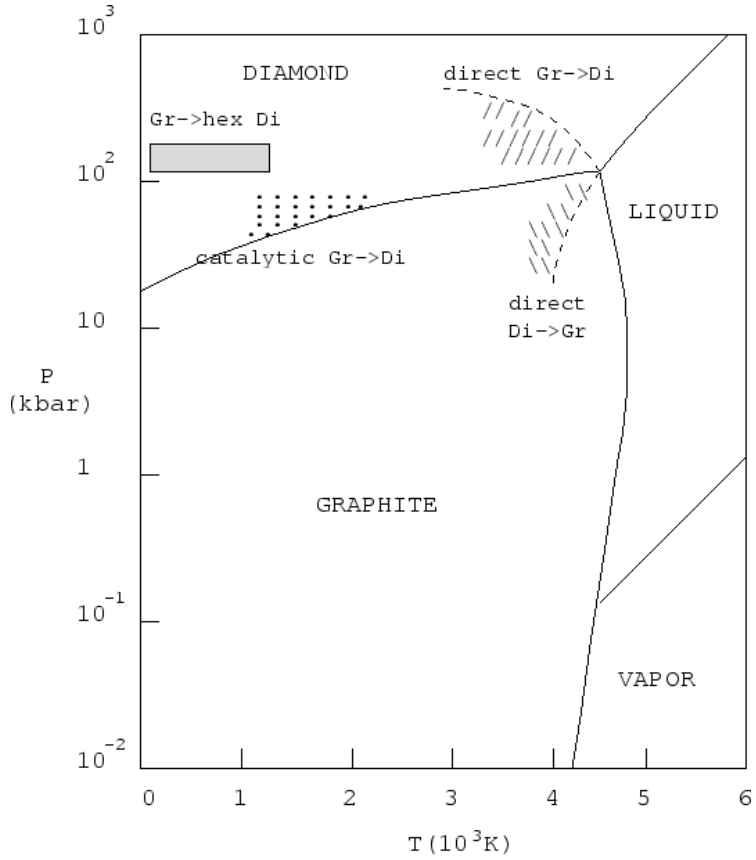

Figure 1.9: The pressure-temperature phase diagram of carbon, reproduced from [15].

for electrical and thermal conduction. The interaction of the delocalized π electron and light causes graphite to appear black.[7] The forces that hold the basal planes together and keep them parallel consist of van der Waals forces (weak electrostatic attractions) as well as some loose overlap of the $2p_z$ orbitals perpendicular to the basal planes.[20, 19] This mechanism is what allows the graphitic planes to be easily moved past one another; thereby causing some of the outward characteristics, such as it being a soft, highly durable, low friction material in most common environmental conditions. This is why graphite is an excellent material for use in pencils, in high temperature industrial applications and as a dry lubricant.

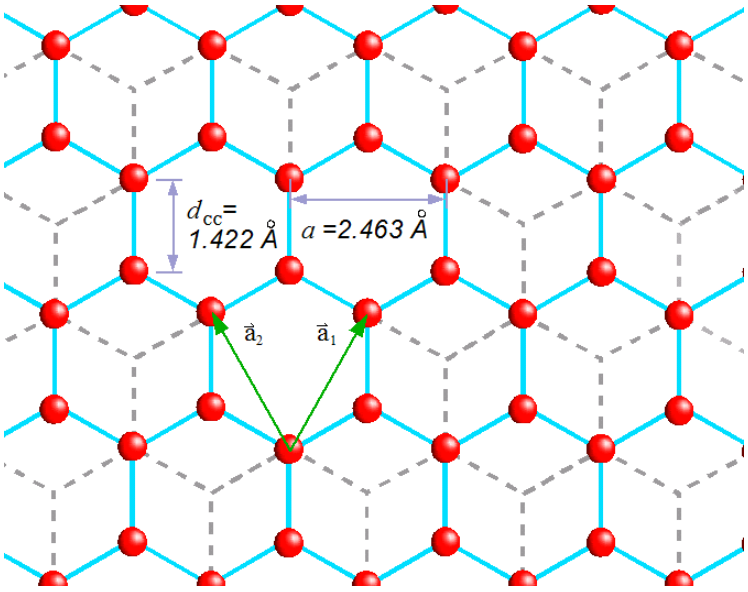

Figure 1.10: A basal plane in graphite with the planar unit vectors and the relative position of the neighboring plane in indicated by the dashed lines.

The normal structure in graphite is the AB stacking sequence of honeycomb planes with an average interplanar distance $\frac{1}{2}c = 3.3539$ Å. Graphite's hexagonal structure with D_h^6 symmetry was apparently first proposed by Hull in 1917.[21] Graphite was one of the first materials to be studied by X-ray diffraction. Bernal *et. al.*[22] used this to determine graphite's structure to indeed be hexagonal planes in an planar stacking sequence A-B-A-B-A ..., henceforth called *Bernal stacking*, which if flat has a space group of $P6_3/mmc$.[23] The atom locations in Bernal stacked graphite are labeled in terms of fractions of the unit cell dimensions a, b and c, see figure 1.11. The AB stacked unit cell is almost twice the volume of the simple hexagonal AA stacking. [3, 19, 20]

Superlubricity is a certain phenomenon in which friction can vanish almost completely. Superlubricity occurs when two crystalline surfaces slide over each other in dry, incommensurate contact. It is an effect that has been already suggested in 1991 but has recently been measured with great accuracy between two graphite

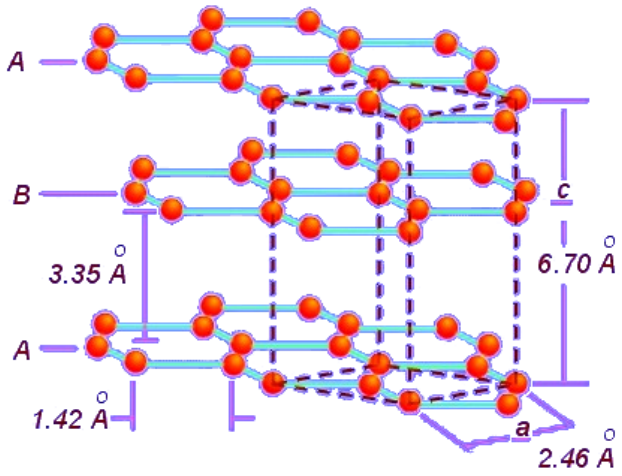

Figure 1.11: The Bernal or AB stacking of basal planes in graphite with the unit cell in dashed lines.

surfaces. One should note that the similarity of the term superlubricity with terms such as superconductivity and superfluidity is misleading; other energy dissipation mechanisms can lead to a finite (normally small) friction force. When the two graphite surfaces are in registry (every 60 degrees), the friction force is high. When the two surfaces are rotated out of registry, the friction is largely reduced to the point of almost vanishing.[24]

1.3.3 Imperfections in Graphite

Though an number of probing techniques a whole range of imperfections are found in graphite. The most common defects to be found in very perfect materials such as graphite flakes are dislocations, tilt and twist boundaries.[3] Consider dislocations in a solid. A dislocation line runs along the core of the dislocation, where the distortion with respect to the perfect lattice is greatest. There are two basic types of dislocations about a dislocation line in a solid. One type is and *edge* dislocation

and the other type is a *screw* dislocation. The Burgers vector characterizes the type of dislocation, since it quantifies the magnitude and direction of the lattice distortion of the dislocation in a crystal lattice. An edge dislocation has its Burgers vector perpendicular to the dislocation line. Secondly, in a screw dislocation the Burgers vector is parallel to the dislocation line.[25]

The four possible extended dislocations in graphite[26] are classified by:

1. Screw dislocation line in the basal plane.
2. Edge dislocation line in the basal plane.
3. Edge dislocation line parallel to the hexagonal c-axis.
4. Dislocation line and Burgers vector in non-basal directions.

The dislocation structures in graphite have been studied thoroughly. Many dislocations observed lie in the basal planes and appear in pairs, each member of the pair being a partial dislocation and the total is $\frac{1}{3}a\langle 11\bar{2}0\rangle$. The separation between the partials varies from about 50-100 nm. The simple straight split dislocation may be found in edge or screw orientation. The partial dislocations repel each other, but the stacking fault between them amounts to an opposing force. The stacking fault enclosed by the partials is, in fact, a region of the crystal in the A-B-C stacking structure that can be best described by a rhombohedral unit cell. Features of the rhombohedral graphite crystal structure, which if flat has a space group of R$\bar{3}$m,[23] are sometimes seen in X-ray diffraction.[3, 19]

Non-basal dislocations can lead to macroscopic structural features and can be studied with optical microscopy. The non-basal dislocations are present in graphite at density in the range of 10^{-3}– 10^{-5} per square cm. A number of studies have demonstrated the existence of screw dislocations with dislocation lines parallel to the hexagonal c-axis, see figure 1.12. A peculiarity of these dislocations is that they have large Burgers vectors from 15–100 nm.[3]

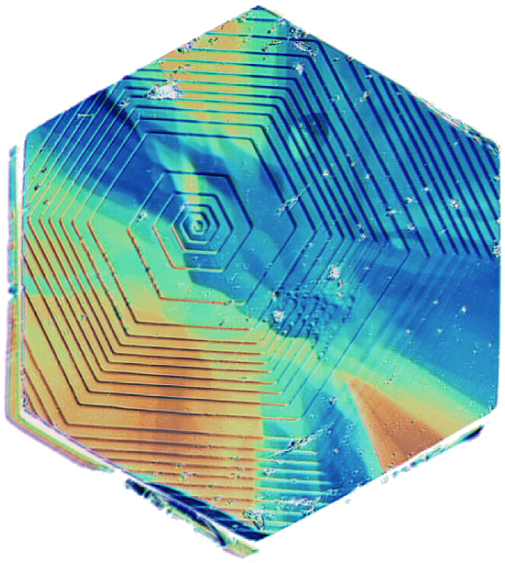

Figure 1.12: A graphite crystal with a screw dislocation, from Dr. John Jaszczak of the Dept. of Physics at Michigan Technological University.

The last kind of impurity to discuss is a local or point defect. Lattice vacancies and interstitial atoms in graphite have been studied. Another class of local lattice defects are topological defects that involve pentagon and heptagon combinations; although only those combinations that do not induce a significant curvature defect in the basal planes are allowed in graphite crystals. The behavior of point defects are completely described by their formation energy and entropy and the energy and entropy of the motion of the defect in the lattice. The energies for a single vacancy and interstitial are shown in table 1.2. The energy release in forming a di-vacancy from two single vacancies is about 5 eV, see figure 1.13.[3]

Why is graphite a good material to use as a neutron moderator in nuclear reactors? The reason is due to the Wigner effect in graphite. The Wigner effect is the displacement of atoms in a solid caused by radiation. High energy neutrons that collide with the Carbon atoms in graphite have enough energy to displace them

Energy	Vacancy [eV]	Interstitial [eV]
formation	7.0 ± 0.5	7.0 ± 1.5
basal plane motion	3.1 ± 2.1	< 0.1
c-axis motion	> 5.5	> 5.0

Table 1.2: Defect formation and migration energies in graphite, from [27].

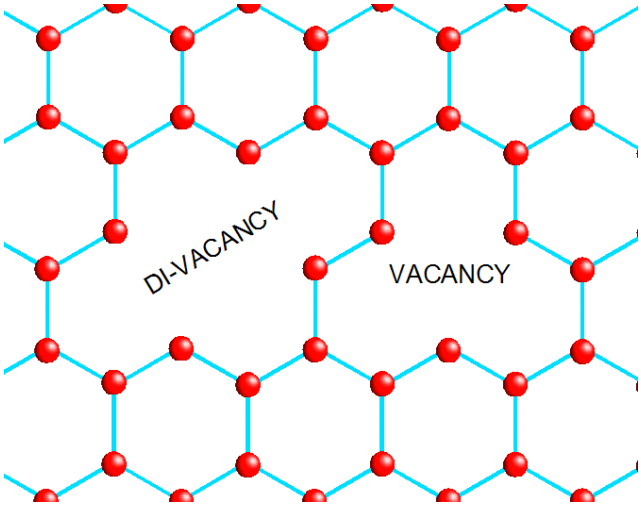

Figure 1.13: The vacancy and di-vacancy in a graphite basal plane.

from the lattice. A neutron's energy can have energies $\sim$ 10 MeV in the center of a nuclear reactor. So the way a neutron moderator slows down fast neutrons is though multiple lattice displacement which each chip away at the kinetic energy. In fact, an MeV neutron striking graphite will create $\sim$ 900 displacements, however not all displacements will create new defects because some of the struck atoms will fill existing vacancies. An interstitial atom and its associated vacancy are known as a Frenkel defect. When large amounts of Frenkel defects have accumulated they pose a risk of releasing all of their energy suddenly through a kind of mass recombination, creating a temperature spike. This build up of energy referred to as Wigner energy can be relieved by annealing, i.e. heating the material. In graphite this occurs at

the relatively low temperature of 250°C, well below its melting point.[28] It is this flexibility of the graphite lattice that makes it and excellent neutron moderator, and a modern strategic resource.

The possibility of energy storage via the formation of Frenkel defects in graphite has been recently studied.[30] They examine structures and recombination routes for interstitial-vacancy (Frenkel) pairs in graphite. Interaction results in the formation of a new metastable defect (an intimate interstitial-vacancy pair) or a Stone-Wales defect. The theoretical results are consistent with the experimentally measured first Wigner energy release peak. Similar defects are expected to form in carbon nanostructures such as nanotubes, nested fullerenes, and onions under irradiation. So graphitic materials could be used to store Wigner energy.

1.4 Fullerenes: Zero-dimensional Carbon

Until the past few decades it was thought that the only pure forms (allotropes) of carbon in nature were diamond and graphite. The evidence of the first fragile all-carbon chains were noted in the 1940's in experiments by Otto Hahn involving a carbon arc lamp. In the 1970's, in radio signals generated by vast interstellar clouds, were found strange molecules that had not been yet synthesized on earth. In 1980, in England, Harry Kroto and Dave Walton synthesized long carbon chains, terminated with hydrogen on one end and with nitrogen on the other.[29] They found that the spectroscopic patterns, of these substances were identical to certain absorption/emission peaks seen in the vast gas clouds. Spectroscopic data hinted at even longer carbon chains produced from red giant stars.[31]

Eventually, in 1985, Kroto persuaded an American colleague, Rick Smalley, to collaborate on a project to simulate conditions of such red giant stars in the laboratory. In Smalley's machine, a powerful laser evaporated a bit of graphite into a hot cloud of particles that were cooled with a stream of helium gas, allowing atoms to

condense into clusters. The mixture was analyzed with a mass-spectrometer, which indicated a large number of molecules had a mass of 720 amu, which must be composed of some combination of 60 carbon atoms. The peak at 720 amu on the graph produced by the mass spectrometer was strong, much stronger than neighboring peaks, which means that C_{60} can form and survive in the high-energy environment of a mass-spectrometer, where many other molecules break up (fragment) in a characteristic way, allowing identification. This could only mean that a collection of 60 carbon atoms was somehow extraordinarily stable.[31]

The mass-spectrum showed clear evidence of C_{60}, but the amounts detected were by far too small to allow a structural analysis. Thus came the hypothesis: the 60 carbon atoms arranged themselves to look like a football or an American soccer ball. Due to its structural symmetry, which featured prominently at the time in the geodesic dome constructions of the architect R. Buckminster Fuller, the molecule C_{60} was named in his honor as buckminsterfullerene (AKA buckyball). Experiments with a carbon-arc in a helium filled bell-jar yielded a soot that contained C_{60} in surprisingly large quantities. This C_{60} soot was purified and then crystalized in order to verify its proposed structure by X-ray crystallography.[31]

This discovery saw the dawn of a new class of carbon clusters, the *fullerenes*. Fullerenes can be thought of as rolled up balls formed from a graphitic sheet. Fullerenes exist in discrete molecular form, and consist of a hollow spherical cluster of carbon atoms. Each molecule is composed of groups of carbon atoms that are bonded to one another form both hexagons and pentagons geometrical configuration. The first discovered and most familiar fullerene is C_{60} is made of 20 hexagons and 12 pentagons, like a soccer ball. Later other kinds of fullerenes were discovered, such as C_{70} which looks like a rugby ball.[7]

The bonding in fullerenes is deformed sp^2, and it has some sp^3 character because of the high curvature. The single bond (C-C) length is 1.46 Å and the double

bond (C=C) length is 1.40 Å. Buckyballs (C_{60}) are semiconducting with a band gap of 1.9 eV. The special bonded structures in fullerene molecules have provided several surprises such as metal-insulator transition, unusual magnetic correlations, very rich electronic and optical band structures and properties, chemical functionalizations, and molecular packing. In the solid state, the C_{60} units form a crystalline structure and pack together in a face-centered cubic array. It is anticipated that, with further developments, the fullerenes will become technologically important materials. Because of their properties, fullerenes have been widely exploited for electronic, magnetic, optical, chemical, biological and medical applications.[7, 4, 32]

1.5 Carbon Nanotubes: One-dimensional Carbon

1.5.1 A Brief History of CNTs

A carbon nanotube (CNT) is a hollow cylinder formed by rolled graphite sheets. The history of CNTs connects to that of graphite with the history of carbon fibers and also later to fullerenes. The earliest application of carbon fiber was to provide a filament for a prototype of the incandescent light bulb by Thomas A. Edison.[33] This first carbon fiber filament was prepared from spiral coils of Kyoto bamboo and then was pyrolyzed to create the first coiled carbon resistor. This peculiar application of Kyoto bamboo is the earliest connection of the history of graphitic materials to Japan, a country which would later become a pioneer in graphitic materials research. Later efforts focused on the vapor growth of carbon filaments, growing filaments from the thermal decomposition of hydrocarbons.[4]

The current line of carbon fiber research and applications come from the needs of the aerospace industry in the 1950's. From this stimulus it was found that a way to prepare continuous carbon fibers from polymer precursors like rayon. From the late 1950's through the 1960's there was intense activity at the Union Carbide

Corporation and the Aerospace Corporation that culminated in the development of the single crystal carbon whisker, a benchmark for the mechanical properties of carbon fibers. The development of HOPG, as described earlier, soon followed. To reduce defects and improve material properties, synthesis of carbon fibers by a catalytic chemical vapor deposition (CVD) process proceeded, laying the ground work for the vapor phase growth of carbon fibers in the 1960's and 1970's. Improved industrial control lead to the commercialization of vapor grown carbon fibers (VGCFs) in the 1990's for various applications.[4]

The discovery of fullerenes became a direct stimulus to systematically study carbon filaments of very small diameter. In December 1990, at a carbon-carbon composites workshop, discussions there stimulated Rick Smalley to speculate about the existence of carbon nanotubes of dimensions comparable to C_{60}. Following this lead, there began experimental investigations based on the established methods to produce fullerenes. When the carbon arc power supply was changed to direct current instead of alternating current, strange tubular structures could be found in one of the electrode's deposits. These tubes are entirely made out of carbon and are called nanotubes, referring to their diameters, which are only a few nanometers wide. These carbon nanotubes (CNTs) were first observed and reported in 1991 by Sumio Iijima of Japan using transmission electron microscopy (TEM).[34] This bridged the framework from the work on fullerenes to this new one dimensional system. Since then, several methods have been devised to produce CNTs, e.g.:

- Electrolysis using graphite electrodes in molten salts
- Catalysed pyrolysis of hydrocarbons
- Laser vaporization of graphite

Threads spun from nanotubes are incredibly strong - three to four times stronger than spider silk, seventeen times stronger than kevlar, and scores of times

stronger than steel. This is partly because of the hexagonal geometry, which can distribute forces and deformations widely and partly because of the strength of the carbon-carbon bond. Materials made from such CNT threads could be used to make bullet-proof vests as light as a T-shirt.[35] They also have unusual electronic properties. Already simple electronic devices, such as diodes, switches and transistors have been realized using nanotubes, which are much smaller than their silicon equivalents.

1.5.2 The structure of CNTs

Broadly speaking there are two types of carbon nanotubes, single-walled and multi-walled carbon nanotubes. Single-wall nanotubes (SWNTs) can be considered to be formed by the rolling of a single layer of graphite (called a graphene layer) into a seamless cylinder. A multiwall nanotube (MWNT) can similarly be considered to be a coaxial assembly of cylinders of SWNTs, like a Russian doll or an onion, one within another; the separation between tubes is about equal to that between the layers in natural graphite. Hence, nanotubes are one-dimensional objects with a well-defined direction along the nanotube axis that is analogous to the in-plane directions of graphite.[36]

The bonding in CNTs is a deformed sp^2 where the circular curvature will case quantum confinement and σ-π rehybridization in the three σ bonds that are slightly out of plane; for compensation, the π bond becomes more delocalized to the outside of the tube. This makes nanotubes mechanically stronger, electrically and thermally more conductive, and chemically and biologically more active than graphite.[7] The first CNTs discovered were multiwalled nanotubes, but later single-walled nanotubes were also isolated.

A straight single-walled nanotube can be made by rolling a flat graphitic sheet into a cylinder. This rolling can be in an arbitrary direction with the only

distortion being due to the curvature of the CNT. This rolling can be done in various ways, resulting in three different kind of nanotubes (called *armchair*, *zigzag* and *chiral*), see figure 1.14. An achiral CNT has mirror image symmetry, while a chiral CNT lacks mirror symmetry, but does have a spiral symmetry. The word chiral here is utilized because in chemical nomenclature such molecules are called axially chiral. There are two cases of achiral tubes; armchair and zigzag nanotubes, which are named for the shape of the cross-sectional ring. Depending on the exact arrangement they exhibit different electronic properties, some are predicted to be metallic while others are semiconductors.[31]

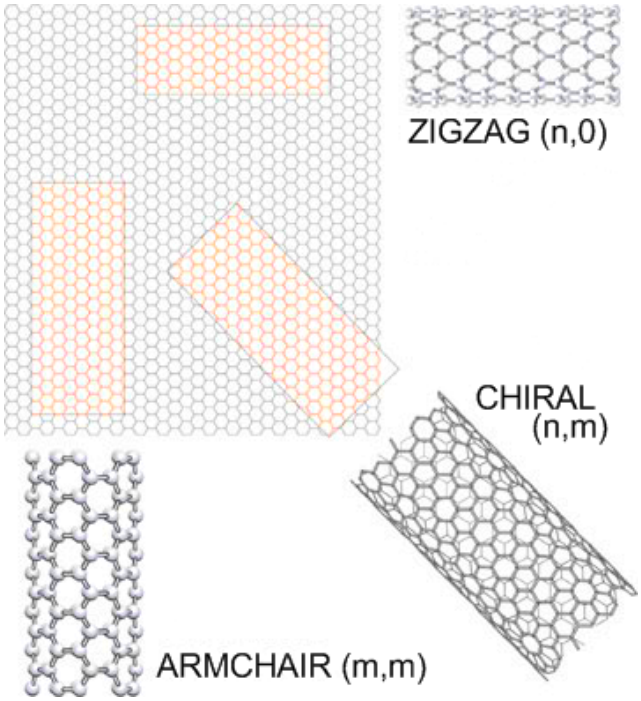

Figure 1.14: By rolling up a graphene sheet in different directions, three types of SWNTs can be formed (with chiral vectors in parentheses): zigzag (n,0), armchair (n,n) and chiral (n,m) where $n > m > 0$ by definition.[7]

A SWNT can be uniquely characterized by the chiral vector $\mathbf{C}$ in terms of a set of two integers (n, m) corresponding to the honeycomb lattice unit vectors $\mathbf{a}_1$

and $\mathbf{a}_2$ (Figure 1.10),

$$\mathbf{C} = n\,\mathbf{a}_1 + m\,\mathbf{a}_2 \equiv (n, m). \tag{1.4}$$

and because of the hexagonal symmetry of the honeycomb lattice we need to only consider $0 \leq |m| \leq n$ to uniquely classify tubes with the chiral vector $\mathbf{C}$, see Figure 1.15. When rolling up a graphene sheet to make a SWNT, it is constructed in such a way that the two end points of $\mathbf{C}_\mathrm{h}$ become superimposed. So a simple single-walled tube is uniquely specified by the chiral vector, denoted (n, m), with its magnitude being the circumference of the tube. The diameter of a tube is then given by

$$D = |\mathbf{C}|/\pi = \frac{a}{\pi}\sqrt{n^2 + nm + m^2}, \tag{1.5}$$

where $a = 2.46$ Å is the honeycomb lattice constant found in CNTs. From energetic considerations stable SWNTs are expected to have diameters between 0.4 nm to 3.0 nm and these have been observed experimentally. The chiral angle θ of a tube is defined as the angle between $\mathbf{C}$ and the zigzag direction $\mathbf{a}_1$,

$$\tan\theta = \sqrt{3}m/(m + 2n). \tag{1.6}$$

Zigzag tubes are characterized by having $m = 0$ and $\theta = 0$, armchair tubes by $m = n$ and $\theta = 30°$ while all others with $0 < \theta < 30°$ are chiral tubes, see Figure 1.16. Lastly, to fully describe the CNT unit cell the translational vector $\mathbf{T}$ is also

needed. It is uniquely specified by the chiral vector $\mathbf{C}$:

$$\begin{aligned}
\mathbf{T} &= t\,\mathbf{a}_1 + s\,\mathbf{a}_2, && (1.7)\\
t &= \frac{2m+n}{d}, \qquad s = -\frac{2n+m}{d}, && (1.8)\\
d &= \begin{cases} \gcd(m,n) & \text{if } n-m \text{ is not a multiple of } 3\gcd(m,n), \\ 3\gcd(m,n) & \text{if } n-m \text{ is a multiple of } 3\gcd(m,n), \end{cases} && (1.9)\\
T &= |\mathbf{T}| = \sqrt{3}C/d. && (1.10)
\end{aligned}$$

Finally, the number of hexagons in a CNT unit cell is given by

$$N_{hex} = \frac{|\mathbf{C}\times\mathbf{T}|}{|\mathbf{a}_1\times\mathbf{a}_2|} = \frac{2(m^2+nm+n^2)}{d}. \qquad (1.11)$$

This fully describes the CNT unit cell as shown in Figure 1.15.[7, 4]

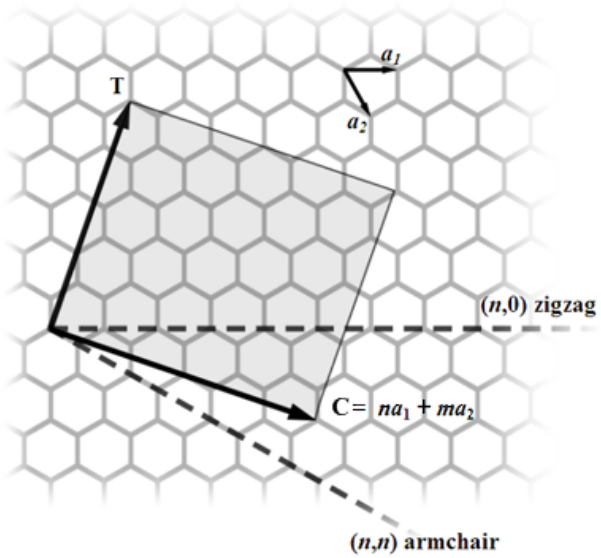

Figure 1.15: The CNT unit cell with the chiral vector $\mathbf{C}$, translational vector $\mathbf{T}$ shown as well as the honeycomb unit vectors. Zigzag $(n,0)$ and armchair (n,n) nanotubes are shown. Based upon similar diagrams found in [37].

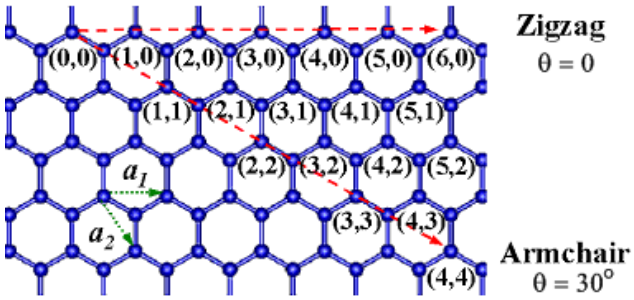

Figure 1.16: Some examples of zigzag $(n,0)$ and armchair (n,n) nanotubes are shown.

When a graphene strip is rolled up to form a nanotube, a periodic boundary condition must be imposed along the tube circumference along the direction of $\mathbf{C}$. Thus the two-dimensional graphene sheet wave vector $\mathbf{k} = (k_x,\ k_y)$ is quantized so that it must satisfy the condition that $\mathbf{k} \cdot \mathbf{C} = 2\pi q$, where $q \in \mathbf{Z}$. From this the condition for having metallic conductance can be derived from a simple π-band model to be

$$n - m = 3q. \tag{1.12}$$

That is, a metallic tube has the difference between the components of its chiral vector, n and m, to be multiples of three. So all armchair tubes and a third of zigzag tubes are conducting. For 1 nm wide SWNTs the semiconducting gap is typically $\sim .8$ eV. Except for the narrowest tubes where σ-π hybridization induces a small correction, this simple π-band model describes all the data well. So the chiral vector $\mathbf{C} = (n, m)$ has a direct relation with the electronic properties of a nanotube. An STM can be used to measure the tube geometry (D, θ), which can be used to derive (n, m). The chiral vector is also related to the optical, magnetic and material properties of CNTs. Controlling the production of a pure population of (n, m) tubes is outstanding nanotechnological problem.[7]

CNTs also come in the form of MWNTs, and SWNT bundles. The tubes in a MWNT are all concentric with one another with a required intertube spacing

$d_{tt} \approx 3.4$ Å, see Figure 1.17. This requirement prohibits zigzag MWNTs, but allows all armchair MWNTs. A typical MWNT has an inner diameter of about ≥ 2 nm and an outer diameter of about ≤ 100 nm. Because the tubes stablize each other the outer diameter of a MWNT can be hundreds of nanometers. MWNTs have been made as the ideal limit of a carbon fiber since 1952. A SWNT bundle or rope can be formed through a self-organized way in which van der Waals forces hold the individual SWNTs in place to form a triangular lattice with a separation of about 3.4 Å.

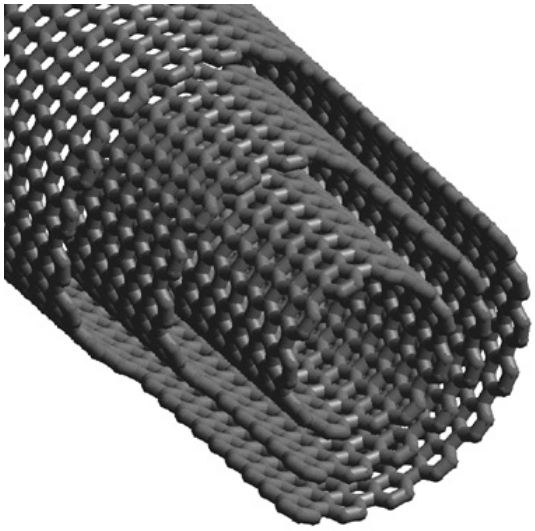

Figure 1.17: A cut away view of a mulit-walled nanotube. From the Polymer and Nanomaterials Group at the Macromolecular Materials Laboratory.

One can also introduce topological defects into the straight tube, which is made up from carbon atoms binding exclusively in hexagon patterns by reducing or adding one carbon bond. The resulting pentagons and heptagons can introduce kinks and local curvature. From these defects, it is possible to create bent tubes, tube junctions, nano-spirals, nano-doughnuts, capped-ends on tubes. Carriers will be localized at a topological defect due to a redistribution of the π electrons. Han *et al.* have developed approaches to model these kind of structures.[38] As an illustration,

consider a SWNT with a single bend junction. The bend angle between the two connected SWNTs follows a simple relation:

$$\Phi = |\theta_1 \pm \theta_2| \,, \tag{1.13}$$

where θ_1 and θ_2 are the chiral angles of the tube segments. For example, any zigzag tube (n_1,0) can be connected with any armchair tube (m_2,n_2) with a $\Phi = 30^\circ$ bend angle when $m_2 = -2n_2$. It is a simple matter to construct branched, toroidal, and helical nanotubes (see Figure 1.18) from bent nanotubes through the topological operations of fusion, rotation, and connection. [7, 31]

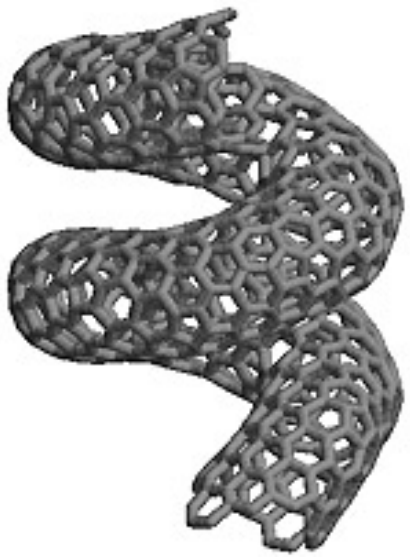

Figure 1.18: A helical nanotube with pentagons and heptagons incorporated to provide curvature.

1.6 Graphene: Two-dimensional Carbon

The discovery of zero-dimensional fullerenes and one-dimensional nanotubes left one form of carbon conspicuous by its absence - the two-dimensional form of graphite

called graphene. Ideal graphite can be thought of as a stacking of weakly bonded basal planes, where each basal plane is a honeycomb lattice comprised of strongly bonded carbon atoms. In isolation, one of these planes is called graphene. The history of the theory and methods to isolate graphene is intiguing and full of surprises. In 2004, by the Manchester group, free-standing graphene became the first atomically two dimensional crystal ever isolated.[39] It was surprising that a truly two-dimensional material, a single atomic layer thick, could exist at all, apparently confounding long-standing predictions that a strictly two-dimensional crystal was structurally unstable in a thermodynamic sense. Subtle deviations from the ideal two dimensional form or a stabilizing substrate is what makes it possible for graphene to exist in a quasi-stable state. Taking the various details into account then requires the discussion of several 'species' of graphene:

- Theoretical graphene (1947)
- Mechanically exfoliated/cleaved graphene (1997-2004)
- Epitaxially grown graphene (1986-2004)
- Chemically exfoliated and intercalated graphene (c.1980-2004)
- Chemical decomposition graphene (1997-still under development)

Graphene research is currently the most prevailing new topic in solid-state physics, stirring up much excitement in the field. The reason is that it offers new inroads into low-dimensional physics, that has never ceased to surprise and continues to provide a fertile ground for novel applications. This new kind of material exhibits exceptionally high crystal and electronic quality and already revealed new physics. In particulat, it is remarkable that the charge carriers behave like massless relativistic particles with a chirality, and an anomalous half integer quantum Hall effect that even persists at room temperature. Due its unusual electronic spectrum,

graphene has provided a new model system to the new concept of a relativistic condensed matter system, where quantum relativistic phenomena, some of which are unobservable in high energy physics, can now be "simulated" in graphene system. Thus, graphene provides an excellent condensed-matter analog toy model of (2+1)-dimensional quantum electrodynamics (QED).[40, 41, 42] Graphene is a marginal conductor that lies at the metal-semiconductor transition point, i.e. it can be viewed equally as a zero-overlap semi-metal or a zero-bandgap semiconductor. It also exhibits a breakdown (or is a marginal case) of the Fermi liquid picture, has ballistic transport and has a high degree of controllability of the carrier density through external fields. Graphene ribbons, bilayers, multilayers, and chemical activations further expands the horizons of this rising star of condensed matter physics. Graphene research also has a newly found importance in regards to fundamental physics.[1, 43, 44] Andre Geim, of the Manchester group, recently said, "What is ... certain is that graphene allows some particle physics and astrophysics ideas to be tested in conceptually simple bench-top experiments rather than in those multibillion dollar machines."[2]

1.6.1 Theoretical graphene

Since graphite makes such a good nuclear moderator, this piqued the interest of many researchers, but any work had to wait until after World War II. The newly burgeoning field of solid state physics proffered a systematic way to study graphite in detail. So it was not until 1947, when Philip R. Wallace, a Canadian, pioneered the calculation of the band structure of graphite in a two-dimensional approximation.[45] This was then very important work with an aim to explain how graphite behaved under neutron irradiation. At the time, the fact that graphite made such a good moderator was surprising. During the war, Wallace was invited to the Canadian labs to take part in an allied international effort to explore the feasibility of graphite-

moderated nuclear reactors. When the Montreal war time laboratory closed, Wallace joined McGill University in 1946 as an Associate Professor in the Department of Mathematics. As reviewed and recounted by M.M.R. Williams, E.P. Wigner had predicted that graphite would shrink under neutron bombardment.[46] As there was no experience in Canada of such matters, Wallace was sent to Bristol, England for several months to work in Sir Neville Mott's department. This led to his first paper on the band structure of graphite published in 1949.[47] This was followed by another paper dealing with radiation effects which suggested a result contrary to that of Wigner: Wallace predicted an expansion of the lattice in the direction perpendicular to the planes by about 15%, which was verified experimentally. The trick was that interstitial atoms formed diamond bonds with the carbon atoms of the layers. This must have been one of the rare occasions, when Wigner was wrong.[48] These papers are all now considered foundational. In the 1947 paper, Wallace developed the theory for the two-dimensional graphitic plane (i.e. graphene) and then used the large anisotropy of the three-dimensional crystal structure to approximate the band structure for graphite. Thus, Wallace inadvertently discovered theoretical graphene.[17]

This two-dimensional approximation describes how the hybridized sp^2 orbitals form the strongly coupled trigonal bonds in the honeycomb lattice. These trigonal orbitals give rise to three bonding and three antibonding σ bands in the graphene band structure. In this model, the weakly coupled $2p_z$ atomic wavefunctions give rise to the two π bands, which are degenerate by symmetry at the six Brillouin zone corners at the K point, which is at the Fermi level. The points K, M and Γ of the graphene Brillouin zone correspond respectively to HKH, LML and $A\Gamma A$ of the three-dimensional graphite Brillioun zone, shown in Figure 1.20. Further calculations of the graphene electronic structure have been made since Wallace: Coulson from 1947 to 1952[49], Córbato from 1956-59[50] in an extensive

calculation using all the carbon atomic orbitals, the Pastori Parravicini group from 1967 to 1969[51], Painter and Ellis in 1970[52]. The dispersion relations for a two-dimensional band structure are shown in Figure 1.21. The degenerate π bands at the K point are of particular interest since the Fermi level goes through this K point degeneracy, and the dispertion relation away from the K point is linear in respect to the wavenumber $\mathbf{k}$ for the π bands. Also note that at the K point the σ-bands lie far away from the π bands in energy. More detailed three-dimensional band models confirm these features. Therefore two-dimensional band models have been extensively applied to provide a qualitative description of much of the experimental data on graphite.[17, 3] In fact, a tight-binding model build on the hopping of the p_z orbitals that give rise to the π bonds provides an amazingly simplified low energy description of two-dimensional graphite and graphene. The Wallace model for graphitic electronic behavior is remarkably successful as a theory for graphene. This theory has been prevailing for describing the properties of the various graphitic materials reviewed so far. Hence, Andre Geim's statement that graphene is the "mother of all graphitic forms" applies in a theoretical as well as a structural sense, see Figure 1.19.[1] In fact, it was the discovery of CNTs in the 1990's that motivated further theoretical work on graphene, much of which can be found in the Journal of the Physics Society of Japan (JPSJ) by various groups, e.g. Ando's group and Saito's group. At the time, these papers where viewed as mostly academic in nature, but now they are commonly referenced or even rehashed in the burgeoning graphene literature. 1.19.[1]

In the next decade, a more complete three-dimensional theory of the graphite band structure was developed that also described how graphite behaved under an intense magnetic field. This is now called the Slonczewski-Weiss-McClure (SWMcC) model.[54] They took into account the weaker interlayer overlaps as well (for details and up-to-date parameters see [17]). Although the interlayer interaction is small, it

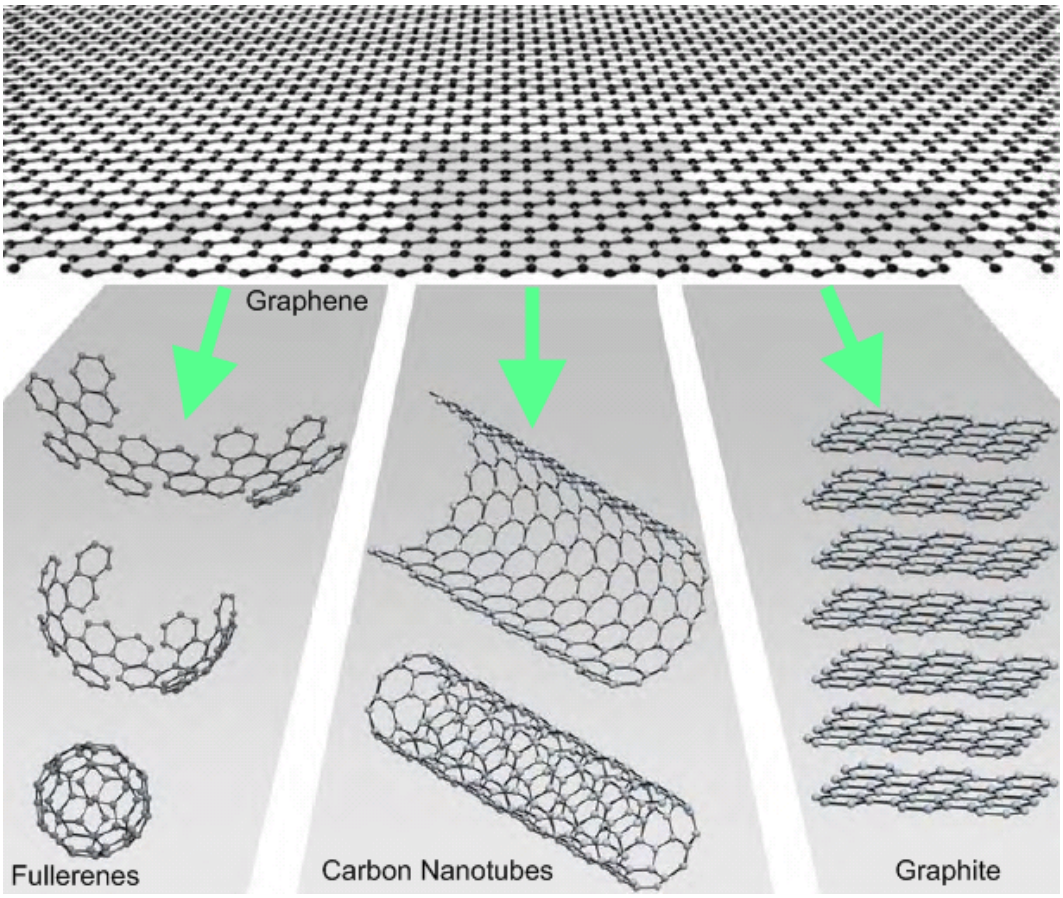

Figure 1.19: Graphene: the mother of all graphitic forms. From [1]

has a profound effect on the four π-bands near the Brillouin zone edges, causing a band overlap that is responsible for the semi-metallic properties of graphite, whereas the two-dimensional model only gives gap semiconductor for graphite.[17] Otherwise, despite having many more parameters the SWMcC model is qualitatively approximated well by the two-dimensional models, see Figure 1.22. The three-dimensional SWMcC model provides the basis for the theory of graphene bilayers, graphene multilayers, and MWNTs.

So why did not the quest for graphene begin a half a century ago? Because a decade before Wallace's seminal work on graphite, Landau and Peierls argued

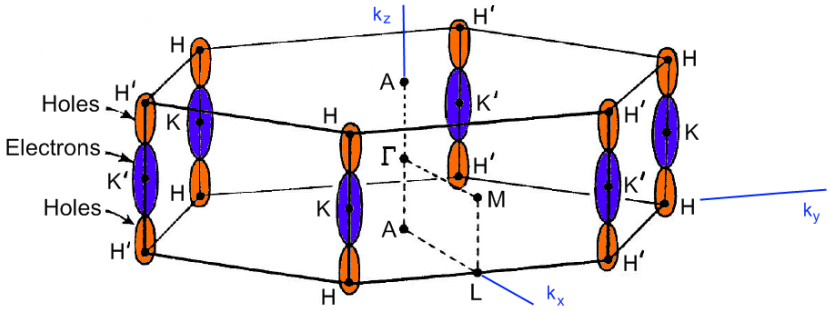

Figure 1.20: The three-dimensional graphite Brillouin zone showing the high symmetry points and a schematic of the graphite electron and hole Fermi surfaces located along the HK axes. Adapted from [17].

that a strictly two-dimensional crystal was thermodynamically unstable and could not exist[56]. They pointed out that a divergent contribution of thermal fluctuations in a low-dimensional crystal lattice should lead to its destruction at any finite temperature[57]. The argument was later extended by Mermin[58] and is strongly supported by a multitude of experimental observations. For example, it is typically observed that thin films segregate into islands or decompose at a thickness of a few dozen of atomic layers[59]. For this reason, atomic monolayers have thus far been known when supported by neighboring 3D structures, usually being formed on crystals with matching lattice constants[59]. Without such a base structure, true 2D crystals were not presumed to exist, until 2004 with the experimental discovery of graphene[39].

Importantly, these continuous graphene crystals were found to exhibit high crystal quality.[39, 60, 61, 62, 63, 64] This means that charge carriers in graphene can travel thousands interatomic distances without scattering.[39, 60, 61, 62] It has been realized that the experimentally obtained graphene flakes are quenched in some metastable state because they are extracted from graphite, whereas their small size ($\ll$1 mm) and the strong carbon-carbon bonds assure that they are stable against thermal fluctuations up to relatively high temperature.[57, 58] It has been

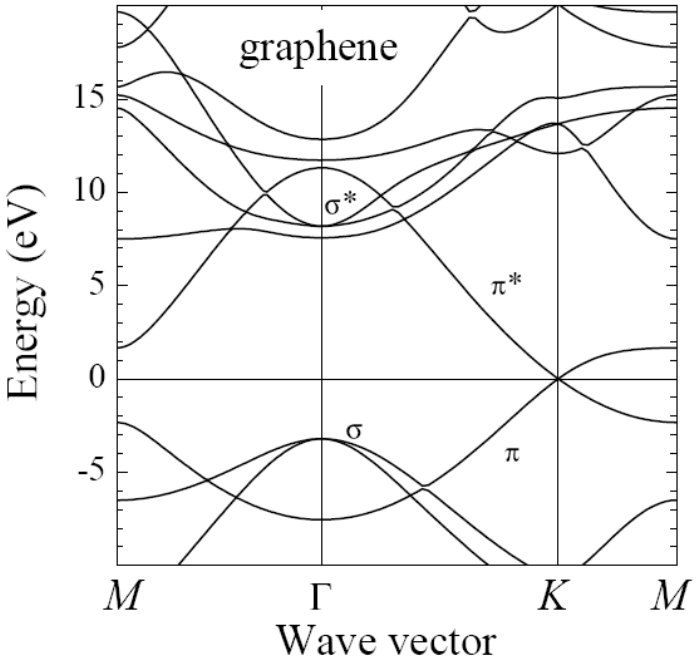

Figure 1.21: Band structure *ab initio* calculation for graphene along the K-Γ-M directions of the two-dimensional zone, in which K corresponds to the HKH axis and the M corresponds to the LML axis of the three-dimensional zone seen in Fig. 1.20. There are six σ bands and two π bands shown. The Fermi level passes through the degenerate π bands at the K point, giving rise to a dispersion relation linear in $\mathbf{k}$ near that point. Adapted from [53].

observed that extracted graphene crystals become intrinsically stable by a gentle crumpling and rippling into the third dimension on a lateral scale of .10 nm.[64, 65] Such 3D warping, at high enough temperature, can actually minimize the total free energy,[65] since although there is a gain in elastic energy it significantly suppresses the thermal vibrations that are anomalously large in a strictly 2D system.[1]

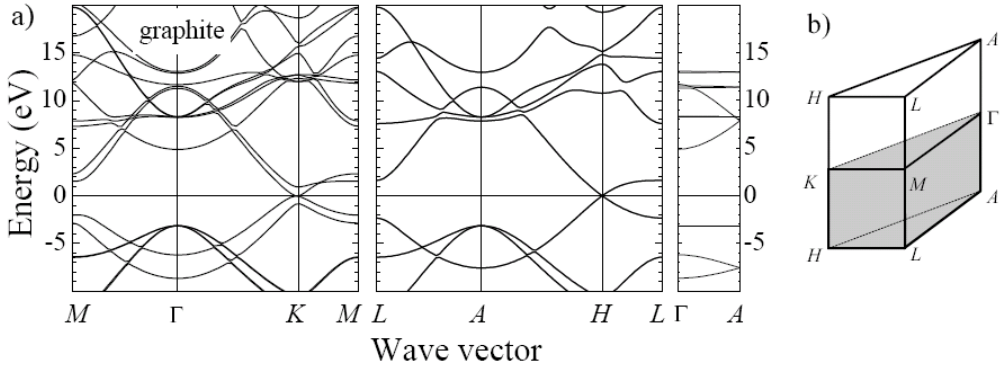

Figure 1.22: (a) Electronic band structure of graphite from *ab initio* calculation in the ΓKM and the AHL plane. The panel to the right shows the interlayer dispersion from the Γ to the A point of the graphene Brillouin zone. The doubling of the carbon atoms in the unit cell splits the electronic bands of graphene in the ΓKM plane for graphite. Note the strong dispersion of the σ and π bands in the ΓA direction. (b) Graphite Brillouin zone. The irreducible domain is shaded, from [53].

1.6.2 Mechanically exfoliated graphene

A free-standing 50×20 μm graphene flake was first observed by the Manchester group in 2004[39, 60] and were soon followed by the Columbia group[62] to the surprise of all. Perhaps the biggest surprise is that this graphene was obtained by extracting single carbon sheets from graphite in an incredibly simple way. Anyone with Scotch tape can jump on this field, remarked Philip Kim of Columbia.[66, 43] This method is called mechanical exfoliation or mechanical cleavage. Most experimental groups are currently using samples obtained by micromechanical cleavage of bulk graphite. After fine-tuning, this technique[60] now provides high-quality graphene crystallites up to 100 μm in size, which is sufficient for most research purposes. Superficially, the technique looks as nothing more sophisticated than drawing by a piece of graphite[60] or its repeated peeling with adhesive tape[39] until the thinnest flakes are found, see Figure 1.23.[1]

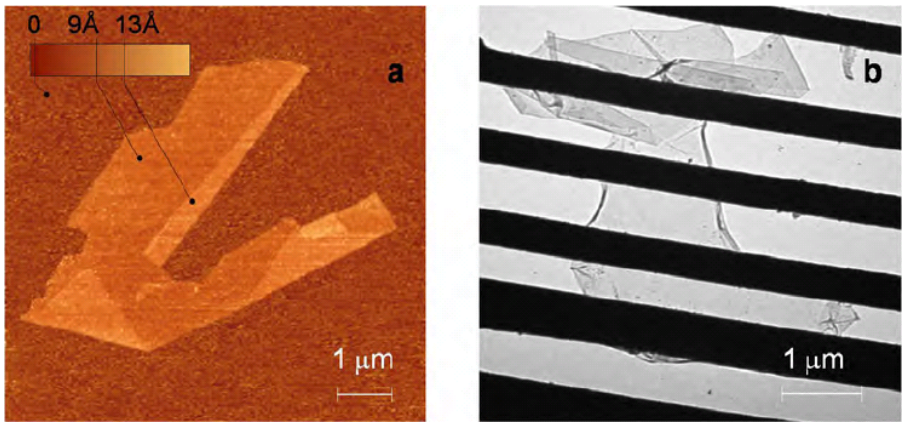

Figure 1.23: Graphene crystallites: (a) Graphene visualized by atomic-force microscopy (AFM), adapted from [60]. (b) A graphene sheet freely suspended on a micron-size metallic scaffold as visualized by transmission-electron-microscopy (TEM). Adapted from [64].

The Manchester group followed a similar approach as was tried by other groups. Earlier the Ohashi group produced graphite flakes from 1000 layers down to 50 layers thick.[67, 44] The next year (2005), Philip Kim's group at Columbia[62] and Paul McEuen's group[68] independently reproduced this work but initially only graphite flakes 20 to 100 layers thick were found. The problem is that a graphene crystallite left on the substrate is extremely rare and is like the proverbial needle hidden in a haystack of graphite flakes. So, even if one were deliberately searching for graphene by using modern microscopy techniques, as commonly done for ultra-thin films, it would be impossible to find the micron-size crystallites dispersed over a 1 cm^2 area.[1]

The critical ingredient for success was the observation[39, 60] that graphene becomes visible in an optical microscope if placed on top of a Si wafer with a carefully chosen thickness of SiO_2, owing to a feeble interference-like contrast with respect to an empty wafer. The layered graphene structures appeared in different hues of blue; it just so happens that the human eye has its highest color sensitivity to this

range of the spectrum due to the color of the sky and ocean. If it was not for this providentially simple and effective way to scan substrates in search of graphene crystallites, they probably would have remained undiscovered even today. Indeed, even knowing the exact recipe[39, 60], it requires special care and perseverance to find graphene. Its detection is very sensitive to small variations in the SiO_2 thickness and the selection of the initial graphite material and the use of freshly-cleaved and -cleaned surfaces of graphite and SiO_2.[1]

Philip Kim's group has continued to develop the mechanical exfoliation method by the use of a *nanopencil*. The technique involves placement of a nanocrystal onto a mechanical cantilever and then sliding the crystal along a substrate to deposit thin layers, somewhat analogous to writing with a pencil. So far the group has succeeded in preparing crystalline graphite down to about 15 layers thin, see Figure 1.24. Because of the nanoscale size of the crystal, it is possible to apply an electric potential to these crystals uniformly altering the chemical potential of the crystal. The researchers have for the first time been able to explore the electrical conduction properties as a function of the chemical potential and in a magnetic field. [62, 69]

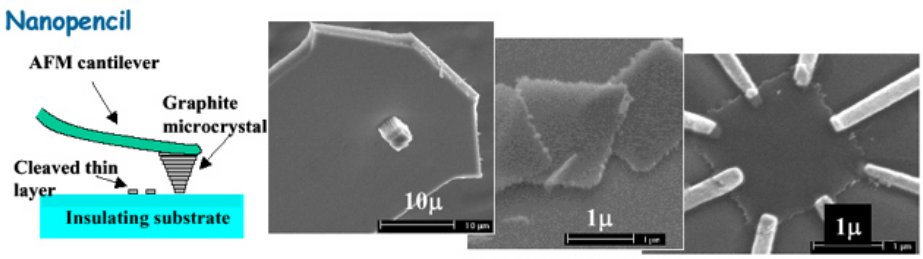

Figure 1.24: The nanopencil used by the Columbia group to fabricate graphene devices. From [69].

Finally, graphene was recently[70] found to have a clear signature in Raman microscopy, which makes this technique useful for quick thickness inspection, although the sample hunting is still done through a optical microscope.[1] The op-

tical and Raman scattering methods may soon be eclipsed by a Rayleigh scattering technique. Cinzia Casiraghi of Cambridge recently demonstrated how Rayleigh scattering can be used to pinpoint graphite sheets on a surface and reveal how many carbon layers are present. The method shows up graphene better than optical microscopy and is much quicker than atomic force microscopy for finding samples.[43]

1.6.3 Epitaxially grown graphene

There have been a number of attempts to grow graphene. Epitaxial growth is where atoms are deposited on a substrate in a controlled manner and continue with a similar crystal structure as the substrate. Epitaxial growth of graphene offers probably the only viable route towards electronic applications and a rapid progress in this direction is expected. Two epitaxial techniques are known of for achieving the formation of graphene so far: 1) chemical vapor deposition (CVD) 2) thermal decomposition resulting in carbon segregation from the substrate to the surface.[1, 71]

In CVD the carbon atoms are supplied from a gas phase. The first experiment was carried out 40 years ago[72]: graphite multilayers grew on various substrates when the substrates were exposed to hydrocarbon gases such as benzene, ethane, and methane, with a suitable reaction temperature maintained.[71] Since the surface dehydrogenation reactivity in the CVD process decreased drastically with the growth of a single graphene monolayer, the growth rates are reduced by one or two orders of magnitude when forming a single monolayer, which makes it possible to precisely control the thickness of the graphene films, i.e. the growth of a graphene bilayer required one or two orders of magnitude more exposure than the growth of the graphene monolayer.[73, 71] Graphene films have been grown epitaxially by CVD of hydrocarbons on metallic substrates: Ni by McConville in 1986,[74] Pt by Land in 1992,[75] HOPG by Affonne in 2001,[77] TiC by Nagishima in 1993.[76] However,

this synthesis has been possible only under some limited conditions.[87] Also, the CVD technique is not useful for all substrates. A typical exception is Si, which forms the stable compound, SiC, by reaction with C.[71]

The second way to grow graphene is by the thermal decomposition of a carbon-bearing substrate.[78, 79] This is done by annealing the samples until some of the carbon atoms migrate to the surface inteface and form graphene layers at the surface. This was first investigated around 1975 by Blakely in Ni doped with C, which segregation onto the Ni(111) surface.[80] Next, this was done on SiC substrates by Bommel *et al.* in 1975[81], the Forbeaux group from 1998 to 2002[82]. The epitaxial growth technique was first widely taken noticed when, starting in 2004, Walt de Heer's group announced their devolopement of monolayer and bilayer graphene films on SiC substrates.[79] This approach using the SiC subtrates seems at present to be the most promising, but what may turn out to be better is to use the previously demonstrated epitaxy on metallic surfaces followed by the deposition of an insulating support on top of graphene and then the chemical removal of the primary metallic substrate. [1]

Epitaxial graphene has been studied by surface science techniques and well characterized with respect to their electronic properties, revealing high-mobility charge carriers.[79] The Lanzara group, at UC Berkeley, has shown angle-resolved photoelectron spectroscopy (ARPES) of graphene grown epitaxially on SiC substrates. This technique is able to map out the electronic structure below the Fermi energy and reveals that the SiC substrate apparently breaks the symmetry of the single graphite layer, leading to a bandgap.[43, 83] Epitaxial graphene films are generally composed of several graphene layers of which the first layer is electron doped due to the built-in electric field and the other layers are essentially undoped. Unlike graphite the charge carriers show Dirac particle properties (i.e. an anoma- lous Berrys phase, weak anti-localization and square root field dependence of the Landau

level energies). Epitaxial graphene shows quasi-ballistic transport and long coherence lengths; properties which may persists above cryogenic temperatures. One point of controversy, versus exfoliated graphene, is that the quantum Hall effect is not observed in high mobility epitaxial graphene. Walt de Heer claims that the effect is suppressed due to absence of localized states in the bulk of the material and that this not a problem with the relatively dirty exfoliated graphene. He further elaborates that damaged samples *do* show a QHE. Others question these assertions and wonder if this is a peculiarity to epitaxial graphene itself. Epitaxial graphene can be patterned using standard lithography methods and characterized using a wide array of techniques. These favorable features indicate that interconnected room temperature ballistic devices may be feasible for low dissipation high-speed nanoelectronics.[84]

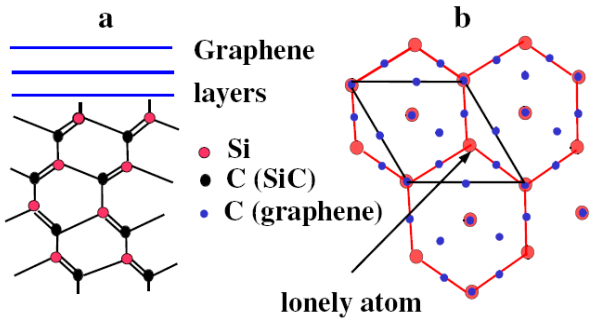

Figure 1.25: An epitaxial graphene film interface geometry. (a) side view, (b) top view of a Si-terminated SiC substrate. From [85].

1.6.4 Chemically exfoliated and intercalated graphene

The earliest attempts to isolate single graphene sheets was based on the method of chemical exfoliation.[86] First, bulk graphite was made into intercalated graphite, a novel new class of materials where the graphene planes are separated by layers of intervening atoms or molecules. Extending the techniques in making intercalated

graphite, sometimes large molecules can be inserted between atomic planes, providing even greater separation so that the product could be considered as isolated graphene layers embedded in a 3D matrix. Next, one can often get rid of the intercalating molecules by a chemical reaction to obtain a soot or sludge consisting of randomly restacked and scrolled graphene sheets.[1, 17, 86, 87]

The synthesis of a graphite intercalation compound was first reported by Schaffäutl in 1841.[88] However, the first systematic studies of these compounds began in the early 1930s with the introduction of X-ray diffraction techniques.[89] Though the systematic study of their physical properties began in the late 1940s, it is only in the past few decades that research on graphite intercalation compounds has intensified. Graphite intercalation compounds are formed by the insertion of atomic or molecular layers of a different chemical species called the intercalant between layers in a graphite host material. Of the various types of intercalation compounds, the graphite compounds are of particular physical interest because of their relatively high degree of structural ordering. Graphite intercalation compounds are classified by a stage index n denoting the number of graphite layers between the adjacent intercalate layers. Because the free carrier concentration of graphite is quite low ($\sim 10^{-4}$ free carriers/atom at room temperature), intercalation with different chemical species and concentrations permits wide variation of the free carrier concentration and thus of the electrical, thermal and magnetic properties. Notably, one intercalation compound (CXAsF5) has been reported with a room temperature conductivity exceeding that of copper[17]

In the preparation of graphite intercalation compounds, exfoliation can be induced by a rapid cooling. So intercalated graphite can used in the preparation of very thin graphitic sheets, known as carbon films.[17] Recently, very thin carbon films with a nanometer thickness have been prepared through a chemical process in two stages, oxidation of graphite and purification to produce a brown graphite

sludge. In the latter stage exfoliation prominently occurs. Techniques have been developed to determine the stage index n all the way down to $n = 1$, detection of a graphene sheet. Although single graphene sheets have been recently detected among these carbon films,[87] at present, this method still lacks enough control to be a viable path to produce isolated graphene crystals.[1] However some interesting properties, such as the observed high T_c superconductivity seen in intercalated graphene, will keep this research ongoing.

1.6.5 Chemical deposition graphene

The same methods for growing carbon nanotubes (the pyrolysis of hydrocarbons in a carbon arc) can be applied to produce graphite films. This breakdown of molecules is called chemical decomposition. This line of research has been probed by the Krishan group over the last decade. Examination with TEM showed a mixture of discs, cones and open tubes, each of about 80 stacked graphene sheets. Devices made from these graphitic films has begun to be evaluated. [90, 1]

Chapter 2

Bulk Graphene

2.1 Introduction

Bulk graphene is a two-dimensional honeycomb lattice of carbon atoms. A honeycomb lattice is not a Bravais lattice, since it has two atoms in its unit cell, henceforth label 'A' and 'B' site. The relative coordinates of A's nearest neighbors are flipped 180° from B's. The nearest neighbors of A sites are always B sites and vice versa, see Figure 2.1. The A and B sites form a triangular lattice among themselves. The carbon atoms form σ and π bonds from the sp^2 hybridized orbitals and $2p_z$ orbital respectively, see Sec. 1.2. It is the $2p_z$ orbital electron that is delocalized throughout the network of shared π bonds that covers the entire honeycomb lattice. So these delocalized electrons basically act as free-particles and hence are primarily responsible for conduction in low fields. The electrons have an added property called pseudospin, which labels whether or not they are on the A sublattice or B sublattice. The surprise is that at low energy the delocalized electrons behave like two-dimensional *relativistic* free-particles; this is due to the quirk of the honeycomb lattice being comprised of two interlocking sublattices. The simplest low energy theory of the π band electrons then is completely analogous to a massless two-

dimensional Dirac equation, with the pseudospin playing the role of real spin. It is this property of bulk graphene having massless Dirac quasi-particles that makes it a remarkable system. The Fermi level in undoped graphene lies at Dirac cone apex, and can be moved by applying gate voltage underneath the graphene sample.[39] The best samples are very clean, with mobilities as high as $\mu = 15000$ cm^2/(Vs) at room temperature,[60] more thatn ten times greater than that seen in silicon. Charge transport is ballistic for long distances across in graphene samples. In fact the electron can go about a third of a μm without scattering. From the observed mobilities in good samples, it seems that impurity scattering is weak.[91] This is also true for CNTs, but it is easier to connect high-quality leads to graphene.

2.2 The Tight-Binding Model: The Least Common Orbital Approximation

Calculating the band-structure of a crystal is one of the seminal problems in solid state physics. In 1928, Bloch[92] provided the initial framework to solve this problem. In the single electron approximation, the total electronic wavefunction is taken as a product of the single electron wavefunctions. The single-particle equation for electrons with mass m_e in the j^{th} band is

$$\hat{H}|\psi_j\rangle = \epsilon_j(\mathbf{q})|\psi_j\rangle, \tag{2.1}$$

where $\mathbf{q}$ is the total wave vector and

$$\hat{H} = -\frac{\hbar^2}{2m_e}\nabla^2 + V_c(\mathbf{r}). \tag{2.2}$$

Bloch's approach is based on the fact that the crystalline potential $V_c(\mathbf{r})$ is periodic in a lattice as controlled by the tiling of the unit cell. In fact, it was Bloch who

first modeled electrons as being tightly bound to particular atoms, overlapping only weakly with neighbors. This *tight-binding model* was further developed and established by Wannier in 1937,[93] who showed how Bloch eigenfunctions could always be summed together to obtain a complete set of wavefunctions, peaked in amplitude on the atoms. Despite the fact that the conduction electrons are delocalized, the tight-binding model has proven to be a simple yet effective starting point for the modeling of metallic solids.[25]

When the quantum theory of solids was developed, graphite was one of the earliest materials to which it was applied. The first calculations of the energy band structure of graphite appears to have been made by Hund and Mrowska[95] in 1937 as an academic exercise. In 1947, Wallace[45] considered both the two- and three-dimensional approximations in graphite using the tight-binding model and made the first attempts to relate such calculations to properties, see Sec. 2.3.[3]

2.2.1 Bloch Wavefunctions

Bloch's theorem states that because of the translational symmetry of the unit cells in the direction of a lattice vector $\mathbf{a}_i$, an eigenfunction of the lattice, Ψ should satisfy the symmetry requirement

$$\hat{T}_{\mathbf{a}_i}\,\Psi = \mathrm{e}^{i\,\mathbf{q}\cdot\mathbf{a}_i}\,\Psi, \tag{2.3}$$

where $\hat{T}_{\mathbf{a}_i}$ is the translation operator along the lattice vector $\mathbf{a}_i$ and $\mathbf{k}$ is the wave vector, which is related to the quantized crystal momentum by $\mathbf{p} = \hbar\mathbf{q}$. The number of lattice vectors, indexed by i, depends on the type and dimensionality of the crystal.[4]

2.2.2 Linear Combination of Atomic Orbitals

Following Bloch, the lattice wavefunction Ψ is usually written in a plane-wave basis, but plane-wave solutions are awkward when relating to the atomic orbitals in a

solid. Alternatively, a functional form Φ_j can be constructed from a j^{th} atomic-like orbital of an atom in the unit cell which satisfies Eqn. (2.3). Hence, some also call this procedure the linear combination of atomic orbitals (LCAO) method. Practically, these are typically constructed by a variational approach and built from hydrogenic wavefunctions.[94] The tight-binding, Bloch function $\Phi_j(\mathbf{q}, \mathbf{r})$ is given by

$$\Phi_j(\mathbf{q}, \mathbf{r}) = \frac{1}{\sqrt{N}} \sum_{\mathbf{R} \in G}^{N} \mathrm{e}^{i\,\mathbf{q}\cdot\mathbf{R}}\, \varphi_j(\mathbf{r} - \mathbf{R}), \qquad (j = 1, \ldots, n_b), \tag{2.4}$$

where here $\mathbf{R}$ is the atomic position and G is the set of allowed lattice vectors, n_b is the number of bands or the number of atomic wavefunctions used in a unit cell, N is the number of unit cells, and φ_j is the atomic wavefunction in state j that provides the modulation of the wavefunction.[4, 97]

A crystal with N unit cells has a length of about $L_i = N_i a_i$ per side, where $N_i \sim N^{1/d}$. The periodic boundary conditions are

$$\hat{T}_{\mathbf{a}_i} \Phi_j(\mathbf{q}, \mathbf{r}) = \Phi_j(\mathbf{q}, \mathbf{r} + \mathbf{L}_i) = \Phi_j(\mathbf{q}, \mathbf{r}), \tag{2.5}$$

which from Eqn. (2.4) implies that

$$q_i = \frac{2\pi n_q}{L_i}, \qquad n_q \in [0, M-1], \tag{2.6}$$

which is applicable for a large enough crystal.[4]

2.2.3 Eigenfunctions and the Secular Equation

Next, we want to solve for the eigenvalues, which in a crystalline solid corresponds to its band structure. The number of atomic orbital wavefunctions in a unit cell, n_b, is also the number of energy bands in the band structure. Hence, there are n_b atomic-like eigenfunctions $\Psi_j(\mathbf{k}, \mathbf{r})$ in the solid which are expressed in terms of the

Bloch basis functions as

$$\Psi_j(\mathbf{q},\mathbf{r}) = \sum_k^{n_b} C_{jk}(\mathbf{q})\,\Phi_k(\mathbf{q},\mathbf{r}), \tag{2.7}$$

where the C_{jk} are constants that depend on the basis.[4]

Given the Hamiltonian operator $\hat{H}$, the eigenvalue $\epsilon_j\mathbf{q})$ of the j^{th} band is

$$\hat{H}|\Psi_j\rangle = \epsilon_j(\mathbf{q})|\Psi_j\rangle \tag{2.8}$$

which for a complete basis of states can be rewritten as

$$\epsilon_j(\mathbf{q}) = \frac{\langle\Psi_j|\hat{H}|\Psi_j\rangle}{\langle\Psi_j|\Psi_j\rangle} \overset{(2.7)}{=} \frac{\sum_{k,\ell=1}^{n_b} C_{jk}^* C_{j\ell}\, H_{k\ell}(\mathbf{q})}{\sum_{k,\ell=1}^{n_b} (\mathbf{q}) C_{jk}^* C_{j\ell}\, \mathcal{S}_{k\ell}}, \tag{2.9}$$

where the transfer integral (or Hamiltonian) matrix is specified by

$$H_{k\ell}(\mathbf{q}) \equiv \langle\Psi_k|\hat{H}|\Psi_\ell\rangle = \int \mathrm{d}\mathbf{r}\, \Psi_k^\dagger \hat{H} \Psi_\ell, \tag{2.10}$$

and the overlap integral matrix is

$$S_{k\ell}(\mathbf{q}) \equiv \langle\Psi_k|\Psi_\ell\rangle = \int \mathrm{d}\mathbf{r}\, \Psi_k^\dagger \Psi_\ell. \tag{2.11}$$

Next, define the vector

$$\mathbf{C}_j \equiv \begin{pmatrix} C_{j\,1} \\ \vdots \\ C_{j\,n_b} \end{pmatrix} \tag{2.12}$$

to give

$$\hat{H}\mathbf{C}_j = \epsilon_j(\mathbf{q})\,\hat{S}\,\mathbf{C}_j, \tag{2.13}$$

which for non-vanishing wavefunction solutions yields the secular equation

$$\det\left[\hat{H} - \epsilon_j(\mathbf{q})\,\hat{S}\right] = 0. \tag{2.14}$$

From this equation of degree n_b, the eigenvalues $\epsilon_j(\mathbf{q})$ can be found, and then the energy dispersion can be plotted with $\mathbf{q}$ along the highly symmetric directions of the first Brillouin zone (FBZ), the irreducible momentum space unit cell. This is the solution for the band structure in a crystal.[4]

2.3 The Simple Two Band Model: Application to Graphene

Although remarkably simplified, the Simple Two Band (STB) model of graphene described the low energy band structure of graphene quite well. It uses the fact that the only delocalized electrons at low energy are the $2p_z$ electrons. The STB aims only at describing the π-bands in graphene, and is also called by some the π tight-binding (πTB) model. This band structure calculation begins by constructing two Bloch functions for the $2p_z$ orbitals of the two inequivalent atoms at A and B in the honeycomb lattice unit cell. The Bloch wavefunctions for graphene in the STB are

$$\Psi_\alpha(\mathbf{r}) = \frac{1}{\sqrt{N}} \sum_{\mathbf{R}_\alpha} \mathrm{e}^{i\,\mathbf{q}\cdot\mathbf{R}_\alpha}\, \varphi_\alpha(\mathbf{r} - \mathbf{R}_\alpha), \qquad (\alpha = A, B), \tag{2.15}$$

where α is called the pseudospin index, and the summation is taken over the set of atomic sites in the A or B sublattice. In Fig. 2.1, the (a) unit cell and (b) Brillouin zone of graphene are shown. The honeycomb lattice unit vectors are $\mathbf{a}_{1/2}$ and the unit vectors of the reciprocal lattice are found by

$$\mathbf{b}_1 = \frac{2\pi(\mathbf{a}_2 \times \hat{z})}{\mathbf{a}_1 \cdot (\mathbf{a}_2 \times \hat{z})}, \qquad \mathbf{b}_2 = \frac{2\pi(\hat{z} \times \mathbf{a}_1)}{\mathbf{a}_2 \cdot (\hat{z} \times \mathbf{a}_1)}, \tag{2.16}$$

where $\hat{z}$ denotes the unit vector normal to the graphene plane.[4, 98]

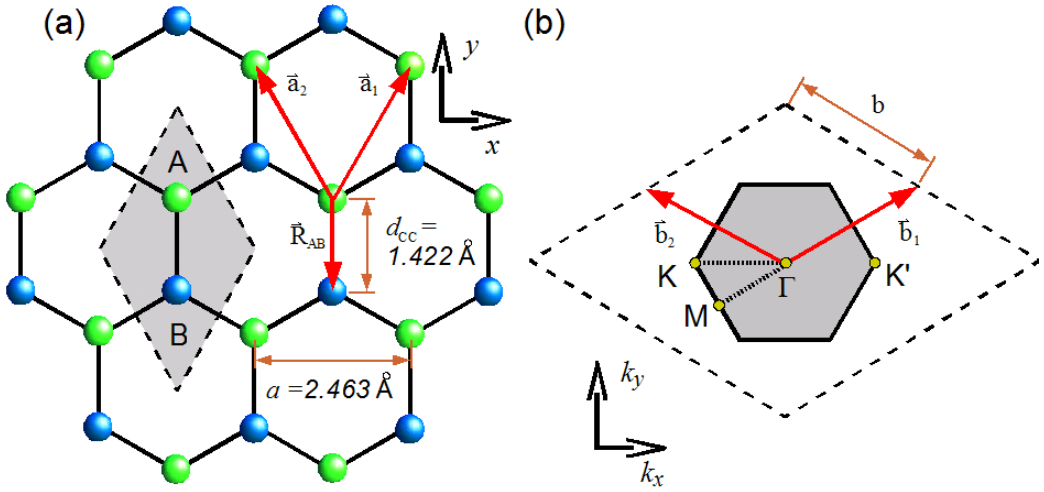

Figure 2.1: The (a) unit cell of graphene shown as the dotted rhombus, and (b) Brillouin zone of graphene shown in the shaded hexagon. Band structure calculations are taken along the perimeter of the K-Γ-M triangle. Note, that of the six vertices of the first Brillouin zone hexagon there are only two inequivalent points K and K'.

Since the STB has $n_b = 2$ then the operators $\hat{H}$ and $\hat{S}$ are 2×2 matrices, here in the pseudospin basis. This allows the secular equation (2.14) to be solved:

$$\epsilon_{\pm}(\mathbf{q}) = \frac{1}{E_3}\left(E_0 - E_1 \pm \sqrt{(E_0 - E_1)^2 - E_2 E_3}\right), \tag{2.17}$$

with

$$E_0 = H_{AA}S_{AA}, \qquad E_1 = \frac{1}{2}\left(H_{AB}S^*_{AB} + S_{AB}H^*_{AB}\right), \tag{2.18}$$

$$E_2 = H^2_{AA} - H_{AB}H^*_{AB}, \qquad E_3 = S^2_{AA} - S_{AB}S^*_{AB} \tag{2.19}$$

All that is left is the determination of the matrices, which depends on the degree of

the approximation.[96]

2.3.1 The Nearest-Neighbor Approximation

From the Bloch states (2.15) and Eqn. (2.10) a 2×2 Hamiltonian matrix $H_{\alpha\beta}$ ($\alpha, \beta \in$ A,B) can be constructed as

$$H_{\alpha\beta}(\mathbf{r}) = \frac{1}{N}\sum_{\mathbf{R}_\alpha,\mathbf{S}_\beta} \mathrm{e}^{i\,\mathbf{q}\cdot(\mathbf{R}_\alpha-\mathbf{S}_\beta)}\langle\varphi_\beta(\mathbf{r}-\mathbf{S}_\beta)|\hat{H}|\varphi_\alpha(\mathbf{r}-\mathbf{R}\alpha)\rangle. \tag{2.20}$$

Now let us denote the three vectors from an A site to the nearest-neighbor B site as $\mathbf{R}_i$ for $i = 1, 2, 3$. So keeping only the nearest-neighbor term from Eqn. (2.20) the off-diagonal matrix element is

$$H_{AB}(\mathbf{r}) = t_0\left(\mathrm{e}^{i\,\mathbf{q}\cdot\mathbf{R}_1} + \mathrm{e}^{i\,\mathbf{q}\cdot\mathbf{R}_2} + \mathrm{e}^{i\,\mathbf{q}\cdot\mathbf{R}_3}\right) \equiv t_0 f(\mathbf{q}), \tag{2.21}$$

where the transfer integral is

$$t_0 \equiv \langle\varphi_B(\mathbf{r}-\mathbf{R}_A-\mathbf{R}_i)|\hat{H}|\varphi_A(\mathbf{r}-\mathbf{R}_A)\rangle \tag{2.22}$$

that by symmetry is the same for any i. The other off-diagonal matrix element $H_{BA} = H^*_{AB}$, since $\hat{H}$ is Hermitian.[4]

Next, consider also the six vectors to the next-nearest neighbors(NNNs) which are the unit vectors $\mathbf{a}_{1/2}$ along with $\mathbf{a}_3 = \mathbf{a}_1 - \mathbf{a}_2$ and there negatives. Next-nearest neighbor atomic sites are in the same sublattice as the original site. So for the case of the diagonal $\alpha = \beta$ matrix elements we have

$$H_{\alpha\alpha}(\mathbf{r}) = \epsilon_{2p} + 2t_1\left(\cos(\mathbf{q}\cdot\mathbf{a}_1) + \cos(\mathbf{q}\cdot\mathbf{a}_2) + (\cos\mathbf{q}\cdot\mathbf{a}_3)\right) + \text{ more distant terms;} \tag{2.23}$$

[4] where ϵ_{2p} is a characteristic energy of the π bonds between two $2p$ orbitals and t_1

is a next-nearest neighbor (NNN) hopping parameter. Since there is no asymmetry between the sublattices here then $H_{AA} = H_{BB}$. The second quantized form of the Hamiltonian including both NN and NNN hopping is

$$\mathcal{H}_{\mathrm{NNN}} = \epsilon_{2p} \sum_{j,\alpha} c^{\dagger}_{j\alpha} c_{j\alpha} + t_0 \sum_{\langle jk \rangle \alpha} c^{\dagger}_{j\alpha} c_{k\bar{\alpha}} + t_1 \sum_{\langle\langle jk \rangle\rangle \alpha} c^{\dagger}_{j\alpha} c_{k\alpha}, \tag{2.24}$$

where $\bar{\alpha}$ is the opposite pseudospin from a and $c^{\dagger}_j$ (c_j) is the creation (annihilation) operator for a carrier at atomic site j.

Similarly from Eqn. (2.11) the overlap integral matrix elements are found to be $S_{AB} = s_0 f(\mathbf{k})$ and $S_{\alpha\alpha} = 1$, where

$$s_0 \equiv \langle \varphi_B(\mathbf{r} - \mathbf{R}_A - \mathbf{R}_i) | \varphi_A(\mathbf{r} - \mathbf{R}_A) \rangle. \tag{2.25}$$

In summary, the explicit pseudospin representations of $\hat{H}$ and $\hat{S}$ keeping only out to nearest neighbor contributions are

$$H = \begin{pmatrix} \epsilon_{2p} & t_0 f(\mathbf{q}) \\ t_0 f^*(\mathbf{q}) & \epsilon_{2p} \end{pmatrix}, \qquad S = \begin{pmatrix} 1 & s_0 f(\mathbf{q}) \\ s_0 f^*(\mathbf{q}) & 1 \end{pmatrix}. \tag{2.26}$$

[4]

Lastly, solving the secular equation (2.14) gives the solution for the energy dispersion of the STB model in the NN approximation

$$\epsilon_{\mathrm{NN}}(\mathbf{q}) = \frac{\epsilon_{2p} \pm t_0 |f(\mathbf{q})|}{1 \pm s_0 |f(\mathbf{q})|} \tag{2.27}$$

for the π band ($+$) and π^* band ($-$) and here $|f(\mathbf{q})|$, using the vectors in Fig. 2.1 is explicitly

$$|f(\mathbf{q})| = \sqrt{1 + 4\cos(\sqrt{3} q_y a/2)\cos(q_x a/2) + 4\cos^2(q_x a/2)}. \tag{2.28}$$

From the dispersion (2.27) the energy values at high symmetry points in the FBZ:

$$\epsilon(\Gamma) = \frac{\pm 3t_0}{1 \pm 3s_0}, \quad \epsilon(M) = \frac{\pm t_0}{1 \pm s_0}, \quad \epsilon(K) = 0; \tag{2.29}$$

with a band width of

$$D_{\mathrm{NN}} = \left| \frac{6t_0}{1 - 9s_0} \right| \tag{2.30}$$

The best fit for the entire band from the *ab initio* calculation of the graphene π bands is

$$\epsilon_{2p} = 0, \qquad t_0 = -3.033\,\mathrm{eV}, \qquad s_0 = 0.129\,\mathrm{eV}, \tag{2.31}$$

which gives the band structure in Fig. 2.2[4]

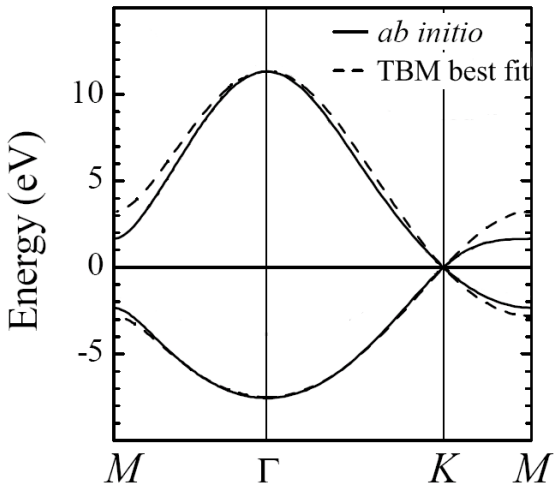

Figure 2.2: The band structure for graphene comparing the *ab initio* calculation (solid line) with that of the NN tight-binding model best fit (dashed line). Adapted from [53].

Now consider some characteristics of this band structure. There are two electrons per unit cell shared by the covalent π bonds. The upper anti-bonding π^* band and the lower bonding π band are degenerate at the K points, through which the Fermi energy passes. Further detailed calculations show that the dispersion near

low energy deviations from the Fermi level at the K points is linear and that the density of states at the Fermi level vanishes; thus graphene is a zero-gap semiconductor. Note, that of the six corners of the hexagonal first Brillouin zone that there are actually only two inequivalent points K and K'.[4]

2.3.2 The Effective Low Energy Hamiltonian: The Dirac Equation

The STB description of graphene was originally developed to study the low-energy properties of graphite, with a focus on modeling the coupling between the graphene sheets. But as interest in carbon nanotubes rose, $s_0 \to 0$ was adopted for the electronic band structure throughout the entire Brillouin zone. The reason for this is that if we are only interested in a good qualitative low-energy description of the graphene band structure near the K or K' points then we can simply use

$$\epsilon_{2p} = 0, \qquad t_0 = -2.7\,\mathrm{eV}, \qquad s_0 = 0.0\,\mathrm{eV}, \tag{2.32}$$

which yields from Eqn. (2.27)

$$\epsilon_{\mathrm{NN}}(\mathbf{q}) = \pm t_0 |f(\mathbf{q})|, \tag{2.33}$$

and this best fits the slopes of the dispersion near the K points from first-principles calculations. [96, 4]

In Fig. 2.3(a) we show an *ab initio* calculation of the two graphene π bands by full lines,and the tight-binding dispersion Eqn. (2.33) by dashed lines. In Fig. 2.3(b) the difference between the two calculations is shown.[96] Note, that as $s_0 \to 0$, the π and π^* bands become symmetrical, see Fig. 2.4.[3, 4]

Now to derive the effective low energy Hamiltonian, also called the $\mathbf{k} \cdot \mathbf{p}$ approximation, first it is helpful to have an explicit representation of the vectors.

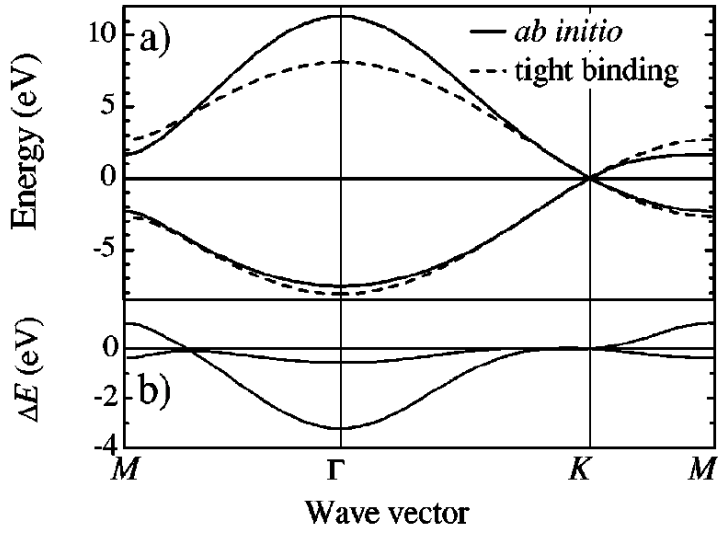

Figure 2.3: The *ab initio* and NN tight-binding dispersions for graphene. (a) The first-principles calculation of the graphene π bands is shown by the full lines. The dashed lines show the tight-binding dispersion of Eqn. (2.33) with the parameters given by (2.32). (b) The difference ΔE between the *ab initio* and tight-binding band structures. Taken from [96].

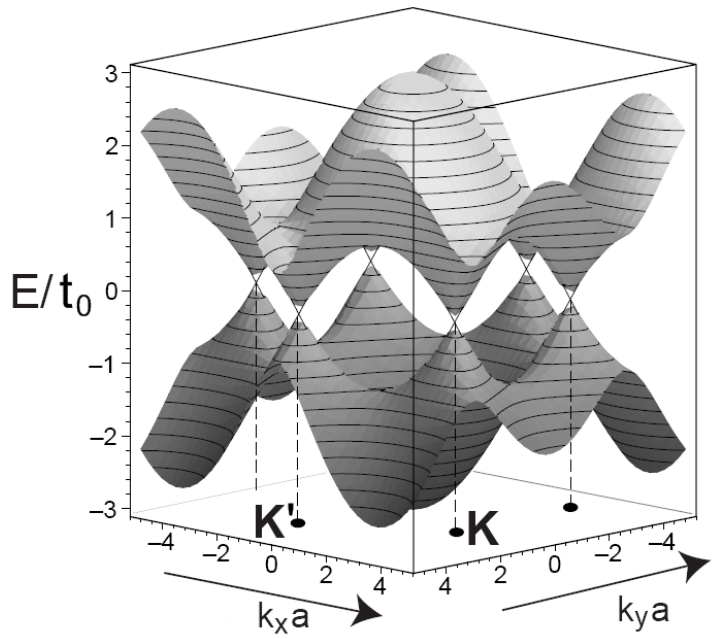

Figure 2.4: The two-dimensional π bands as determined from the STB model best fit near the low energy K points. Adapted from [97].

The vectors in Fig. 2.1 are explicitly

$$\mathbf{a}_{1/2} = \frac{a}{2}\left(\pm 1, \sqrt{3}\right), \qquad \mathbf{R}_{AB} = \frac{a}{\sqrt{3}}\left(0, 1\right), \tag{2.34}$$

where $a = \sqrt{3}\, d_{CC} = 2.463$ Å is the graphene lattice constant and we have denoted the vector from an A site to a neighboring B site aligned along the y-axis as $\mathbf{R}_{AB}$. So now we can rewrite $f(\mathbf{q})$ in Eqn. (2.21) as

$$f(\mathbf{q}) = \left(1 + \mathrm{e}^{i\,\mathbf{q}\cdot\mathbf{a}_1} + \mathrm{e}^{i\,\mathbf{q}\cdot\mathbf{a}_2}\right)\mathrm{e}^{i\,\mathbf{q}\cdot\mathbf{R}_{AB}} \tag{2.35}$$

Next, we need to expand the momentum about the K point $\mathbf{q} = \mathbf{K} + \mathbf{k}$, where explicitly we have that

$$\mathbf{b}_{1/2} = \frac{b}{2}\left(\pm\sqrt{3}, 1\right), \quad \mathbf{K} = \frac{b}{\sqrt{3}}(-1, 0) = \frac{4\pi}{3a}(-1, 0), \quad \mathbf{K}' = \frac{4\pi}{3a}(+1, 0), \tag{2.36}$$

where and $b = 4\pi/\sqrt{3}a$ are the reciprocal lattice constant for graphene. Thus we can rewrite $f(\mathbf{q})$ as

$$f(\mathbf{k}) = \left(1 + \bar{\omega}\,\mathrm{e}^{i\,\mathbf{k}\cdot\mathbf{a}_1} + \omega\,\mathrm{e}^{i\,\mathbf{k}\cdot\mathbf{a}_2}\right)\mathrm{e}^{i\,\mathbf{k}\cdot\mathbf{R}_{AB}}, \tag{2.37}$$

where here $\omega = \exp\left(2\pi i/3\right)$ and $\bar{\omega} = \exp\left(-2\pi i/3\right)$. So, expanding to lowest order in $\mathbf{k}$

$$\begin{aligned} f(\mathbf{k}) &\cong \left(\overbrace{1 + \bar{\omega} + \omega}^{0} + i(\bar{\omega}\mathbf{k}\cdot\mathbf{a}_1 + \omega\mathbf{k}\cdot\mathbf{a}_2)\right)\mathrm{e}^{i\,\mathbf{k}\cdot\mathbf{R}_{AB}}, && (2.38)\\ &\cong -i\,\sqrt{3}/2(i\,k_x + k_y)\,a\,\mathrm{e}^{i\,\mathbf{k}\cdot\mathbf{R}_{AB}}, && (2.39)\\ &= \sqrt{3}/2(k_x - i\,k_y)a + \mathcal{O}(k^2) && (2.40)\\ & && (2.41) \end{aligned}$$

Keeping only to linear order in $\mathbf{k}$, the low energy effective Hamiltonian about the K point is then

$$H^K(\mathbf{k}) \cong \begin{pmatrix} 0 & \sqrt{3}t_0 a/2(k_x - ik_y) \\ \sqrt{3}t_0 a/2(k_x + ik_y) & 0 \end{pmatrix}. \tag{2.42}$$

Finally, defining the Fermi velocity as $\hbar v_{\mathrm{F}} = \frac{\sqrt{3}}{2} t_0 a$ allows the exploitation of a useful analogy. Namely, that we can rewrite the low energy Hamiltonian in the form

$$\hat{H}_{\mathrm{D}}^K(\mathbf{k}) = \hbar v_{\mathrm{F}}(k_x \sigma_x + k_y \sigma_y) = \hbar v_{\mathrm{F}}\, \boldsymbol{\sigma} \cdot \mathbf{k} \tag{2.43}$$

where σ_i are the Pauli matrices for the pseudospinors and all vectors are henceforth understood to be two-dimensional and the quantum momentum operator can be realized by taking $\mathbf{k} \to -i\nabla$. This Hamiltonian is analogous to a two-dimensional Dirac equation of a massless Fermion with the Fermi velocity $v_{\mathrm{F}} \sim c/300 \approx 10^6$ m/s used instead of the speed of light. This is like a massless electron or a classic neutrino, with charge added, embedded in a 'Flatland' universe. For the inequivalent K' point, its Dirac Hamiltonian is the same as Eqn. (2.43) except that $\boldsymbol{\sigma}$ is replaced with $-\boldsymbol{\sigma}^*$.

2.3.3 Energy Spectrum and the Particle-Hole Basis

The two-dimensional Dirac Hamiltonian can be rewritten as

$$H_{\mathrm{D}}(\mathbf{k}) = \hbar v_{\mathrm{F}} \begin{pmatrix} 0 & k\, \mathrm{e}^{-i\,\theta} \\ k\, \mathrm{e}^{+i\,\theta} & 0 \end{pmatrix} = \hbar v_{\mathrm{F}} k\, \mathrm{e}^{\sigma_y\, \theta}, \tag{2.44}$$

where $\tan\theta = \frac{k_y}{k_x}$. Squaring the Dirac Hamiltonian $\hat{H}_{\mathrm{D}}^K(\mathbf{k})$ in Eqn. (2.44) gives the low-energy linear spectrum:

$$\epsilon_b(\mathbf{k}) = b\, \hbar v_{\mathrm{F}}\, k, \tag{2.45}$$

where the $b = \pm 1$ denotes the particle (hole) Dirac cones. The normalized bulk Dirac eigenfunction at the K/K' point is

$$\psi_b^{K/K'}(\mathbf{r}, \mathbf{k}) = \frac{1}{\sqrt{2\mathcal{A}}} \mathrm{e}^{i\,\mathbf{k}\cdot\mathbf{r}} \begin{pmatrix} b \\ -\mathrm{e}^{\pm i\,\theta} \end{pmatrix}. \tag{2.46}$$

where the area of the crystal is $\mathcal{A}$. As we can see here, the bulk wavefunctions at the Dirac points are related by $\psi^{K'} = \sigma_z \psi^K$; therefore the K point is converted into the K' point and the K' point into the K point under time reversal, see Sec. 2.3.7.[99]

Now the quantized area of the reciprocal space for a crystal is $(2\pi)^2/\mathcal{A}$. Thus, the number density at low energy is

$$n = \sum_{\mathbf{k}} \theta(k_\mathrm{F} - k) \cong \int \mathrm{d}\mathbf{k}\, D(\mathbf{k}) \theta(k_\mathrm{F} - k), \tag{2.47}$$

where the factor $D(\mathbf{q}) = g_s g_v/(2\pi)^2$ is the density of levels, and the spin $g_s = 2$ and valley degeneracy $g_v = 2$. So the number density becomes

$$\begin{aligned} n &= \frac{g_s g_v}{2\pi} \int \mathrm{d}\mathbf{k}\, k\, \theta(k_\mathrm{F} - k) && (2.48) \\ &= \frac{1}{\pi} k_\mathrm{F}^2. && (2.49) \end{aligned}$$

Therefore the Fermi wave vector and free-electron radius are related to the number density by

$$k_\mathrm{F} = r_s^{-1} = \sqrt{\pi n}. \tag{2.50}$$

This means that the carrier density is linearly related to the Fermi level which is

changed through a bias or doping. The energy density of states is defined by

$$D(\epsilon) = \int \mathrm{d}\mathbf{k}\, D(\mathbf{k})\, \delta(\epsilon(k) - \epsilon'(k)) \tag{2.51}$$

$$= \frac{g_s g_v}{2\pi(\hbar v_\mathrm{F})^2} \int_0^\infty \mathrm{d}\epsilon'\, |\epsilon'|\, \delta(\epsilon(k) - \epsilon'(k)) \tag{2.52}$$

$$\tag{2.53}$$

So the total density of states becomes

$$D(\epsilon) = \frac{2|\epsilon|}{\pi\hbar^2 v_\mathrm{F}^2}. \tag{2.54}$$

[25, 99]

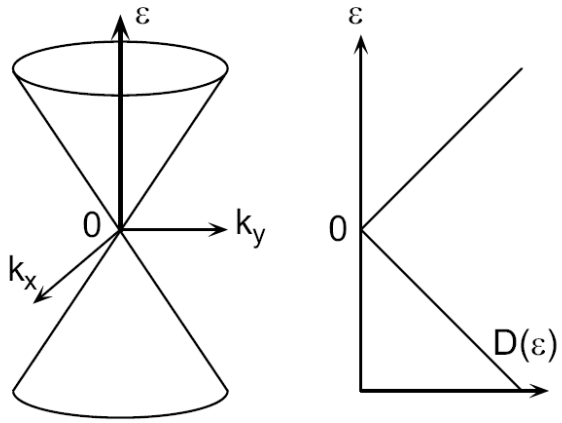

Figure 2.5: The energy dispersion and density of states in the vicinity of the K points. Taken from [99].

Next, define the transformation unitary matrix

$$\hat{U}^K(\mathbf{q}) = \frac{1}{\sqrt{2}} \begin{pmatrix} \mathrm{e}^{-i\,\theta/2} & +\mathrm{e}^{-i\,\theta/2} \\ \mathrm{e}^{+i\,\theta/2} & -\mathrm{e}^{+i\,\theta/2} \end{pmatrix} = \sigma_z \mathrm{e}^{-i\,\sigma_z\,\theta/2} + \sigma_x \mathrm{e}^{-\sigma_y\,\theta/2}. \tag{2.55}$$

Then we find that U^K transforms to the particle-hole basis

$$\hat{\tilde{H}}_{\mathrm{D}} = (U)^{\dagger}\, \hat{H}_{\mathrm{D}}\, U = \hbar v_{\mathrm{F}} \begin{pmatrix} k & 0 \\ 0 & -k \end{pmatrix} = \hbar v_{\mathrm{F}}\, \tilde{\sigma}_z\, k, \tag{2.56}$$

where the $\tilde{\sigma}$ denotes that these Pauli matrices are used in the particle-hole basis. The basis eigenvectors in Eqn. (2.15) are related by

$$\varphi_{\pm} = (\varphi_A(\mathbf{r} - \mathbf{R}_A) \pm \varphi_B(\mathbf{r} - \mathbf{S}_B))\, \mathrm{e}^{\mp i\,\theta/2}, \tag{2.57}$$

where $(+)$ denotes the antibonding (π^*) state and $(-)$ denotes bonding (π) state with eigenvalue $\pm\hbar v_{\mathrm{F}} k$ and have the eigenvalues of $\epsilon_{\pm}$ in Eqn. (2.45).

2.3.4 Chirality and Helicity

The graphene quasi-particles are analogous to two-dimensional classic neutrinos. In particle physics experiments one useful feature of the classic massless neutrinos is that they have an absolute chirality, or helicity. Generally speaking helicity is a Lorentz invariant quantity, while chirality is not. The chirality of a particle quantifies how its spin $\mathbf{S}$ is projected onto its direction of motion, *i.e.*

$$\chi = \hat{\mathbf{S}} \cdot \hat{\mathbf{p}}, \tag{2.58}$$

where its momentum is $\mathbf{p}$. Now if the particle has mass it is always possible to boost to a faster reference frame than the particle and hence change the sign of $\hat{p}$, but if it is massless then the chirality cannot change. A massive particle is said to have *relative* chirality. When the spin points into (against) the axis direction it is said to have right-(left-)handed helicity, see Fig. 2.6.[100, 99]

The low energy graphene quasi-particles near the K (K') point, like the anti-neutrino (neutrino), has a right-(left-)handed helicity. That $\hat{H}_D$ is the helicity times

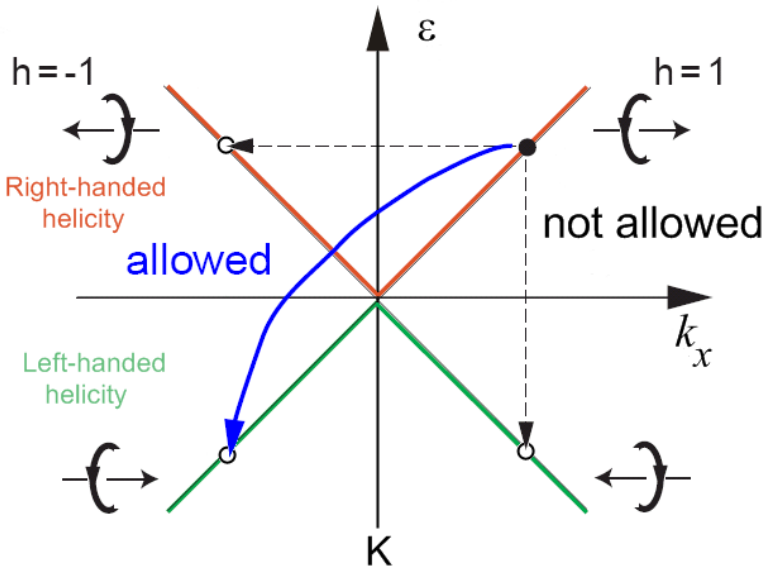

Figure 2.6: Helicity in the low energy graphene spectrum near the K point; h denotes the helicity of the pseudo-spin, where the particle band for $\epsilon > 0$ (red) has right-handed helicity and the hole band for $\epsilon < 0$ (green) has left-handed helicity. The K' point has the signs reversed. Allowed transitions have conserve helicity. Adapted from [97].

a constant shows that the allowed momentum eigenstates must have a pseudospin in the direction of motion, i.e. they are helicity eigenstates. Recall, that a spin-1/2 spinor changes its sign under a 2π rotation and does not come back to the same phase until a 4π rotation. For the graphene pseudospinor, the analogous sign change can be understood in terms of a Berrys phase[112]. That is, when a wave vector $\mathbf{k}$ of a wavefunction is rotated in an anticlockwise direction adiabatically as a function of time t around the k-space origin for the interval $0 < t < t'$, the wavefunction is transformed to $\varphi_\alpha(\mathbf{k})\mathrm{e}^{i\,\eta}$, where the Berry's phase η is given by

$$\eta = -i \int_0^{t'} \mathrm{d}t \, \langle \varphi_\alpha(\mathbf{k}(t))| \frac{\mathrm{d}}{\mathrm{d}t} |\varphi_\alpha(\mathbf{k}(t))\rangle = -\pi, \tag{2.59}$$

where $\mathbf{k}(t)$ moves along a closed contour CCW around the origin at $k = 0$ between time $t = 0$ and t'. Therefore the wavefunction acquires phase $-\pi$ when $\mathbf{k}$ is rotated around the origin. The signature change occurs only when the closed contour encircles the origin $k = 0$ but not when the contour does not contain the origin. This topological singularity at $k = 0$ and its associated Berrys phase are the origin of the absence of backward scattering (or back-scattering) in metallic carbon nanotubes and graphene ribbons. Helicity should be conserved and backscattering would violate that conservation, see Fig. 2.6. It has been suggested that the chiral nature of graphene carriers makes disordered regions transparent for these carriers independently of the disorder, as long as it is smooth on the scale of the lattice constant.[91, 101, 115] However, the absence of the back scattering disappears in magnetic fields, giving rise to a huge positive magnetoresistance. This Berry's phase is also important to getting the position of the Landau levels right, see Sec. 2.6.[99, 113]

2.3.5 Gap Inducing Effects

Now that we see that graphene offers an analogy to a massless two-dimensional Dirac spectrum, could there also be a way to add a 'mass', *i.e.* a gap between the particle and hole bands. The possible ways to induce a gap:

- A/B sublattice asymmetry
- K to K' scattering
- Quantum confinement
- Spin-orbit coupling, see Sec. 2.3.6.

One of the most well-known ways to induce a gap in bulk graphene is by introducing an asymmetry between the A and B sublattice sites. Such a gap can be added to the Hamiltonian operator (2.43) by the term

$$\mathcal{H}_{\text{gap}} = m_{\text{D}} v_{\text{F}}^2 \, \sigma_z, \tag{2.60}$$

which again follows the relativistic analogy through introducing a Dirac mass, m_{D}. This gives a low energy spectrum of

$$\epsilon_{\pm} = \pm v_{\text{F}} \sqrt{(\hbar k)^2 + (m_{\text{D}} v_{\text{F}})^2}, \tag{2.61}$$

The Hamiltonian in second quantized for is

$$\mathcal{H}_{\text{gap}} = m_{\text{D}} v_{\text{F}}^2 \sum_{i,\alpha\beta} c_{i\alpha}^{\dagger} \sigma_{\alpha\beta}^{z} c_{i\beta} \tag{2.62}$$

There is some experimental support for the existance of such gaps. The A/B asymmetry effect is most prevailing in epitaxial graphene, where on TiC this asymmetry has been seen as high as $m_{\text{D}} v_{\text{F}}^2 = 1.3$ eV. The breaking of the six-fold

symmetry to a three-fold symmetry as seen in ARPES measurements in epitaxial graphene grown on SiC accompany a measurable gap in the dispersion. The presence of scatters that break the symmetry of the Dirac Hamiltonian and cause inter-valley scattering can induce a gap. This K/K' mixing term goes like an exchange term:

$$\mathcal{H}_J = J_{\mathrm{D}}\, \sigma_z \tau_z. \tag{2.63}$$

P.N. First's group has seen such inter-valley scattering due to impurities in epitaxial graphene. Lastly, finite size effects due to quantum confinement in graphene nanoribbons can induce gaps, see Sec. 3.1.2 and Eqn. (3.11).[44]

2.3.6 Spin-Orbit Effects

The main interactions that could affect the spin degree of freedom in graphene are spin-orbit coupling and the exchange interaction. It is not known to which extent magnetic impurities are present in actual graphene samples. However, their effect seems quite small, as noticed recently when investigating weak localization and universal conductance fluctuations in graphene.[101] The spin-orbit (SO) interaction in graphene is supposed to be weak, due to the low atomic number $Z = 6$ of carbon. Therefore both spin-splitting and spin-flip scattering due to the combination of spin-orbit and scattering due to disorder can be usually ignored. As a result, in most investigations spin degenerate states are assumed and focus on the combined fourfold pseudospin plus spin degeneracy. Although it could be that electronic spin is irrelevant when studying bulk properties, for edge states this may be quite different. Stable room-temperature induced magnetism at the edges of graphite samples irradiated with protons has been reported.[102] Moreover, perspectives of spintronic applications in graphene could be very promising, so it is important to examine the role of the spin.[103]

Spin-orbit coupling is a true relativistic correction that arises whenever spinors

are in or around orbitals. The angular momentum **L** and spin **S** interact with each other through a spin-orbit interaction. The first order relativistic correction that describes how free-particle spinors behave in an spatially varying potential is called Pauli spin-orbit coupling. In a crystal this becomes the microscopic spin-orbit interaction:

$$V_{SO} = \frac{\hbar}{(m_e c)^2}(\boldsymbol{\nabla} V(\mathbf{r})) \times \mathbf{p} \cdot \mathbf{s}, \tag{2.64}$$

where **s** is the spin.

Intrinsic spin-orbit (ISO) coupling is between the electrons and the atomic nuclei on the lattice sites, so Eqn. (2.64) becomes

$$H_{\mathrm{ISO}} = \xi \sum_i \mathbf{L_i} \cdot \mathbf{S_i}. \tag{2.65}$$

where the gradient of the effective $2p$ atomic potential $V(\mathbf{r}) \sim \mathrm{e}^2/r$ is put into the atomic constant ξ. The graphite Hamiltonian including the intrinsic spin-orbit coupling was first described by the Dresselhauses[104], and McClure and Yafet[105] first estimated the magnitude of the intrinsic spin-orbit coupling in graphite to be about 2.0×10^{-4} eV (2.3 K). This value of the spin-orbit coupling in graphite is small compared to the band overlap in graphite, so it has always been neglected. The magnitude of the graphite coupling is significant because it apparently influenced the claim for the ISO in graphene made by Kane and Mele.[106] However, the ISO in graphite can be quite larger than that found in graphene because the coupling between the graphite layers is quite important and influences the effective value of the spin-orbit gap.[103] Nevertheless, in graphene ISO could possibly have some detectable effect, since this interaction does lift some of the degeneracies in the band structure, although so does the Rashba spin-orbit effect.[3]

Spin-orbit coupling in graphene has an intrinsic part, completely determined from the symmetry properties of the honeycomb lattice of carbon atoms. This is sim-

ilar to the Dresselhauss spin-orbit interaction in semiconducting heterostructures.[107] Group theoretical arguments obtain the form of the effective Hamiltonian for the intrinsic spin-orbit coupling around the K and K' points to be

$$\hat{H}_{\mathrm{ISO}} = \Delta\, \tau_z\, \sigma_z s_z, \tag{2.66}$$

where s_z is a Pauli matrix for the spin-degree of freedom and Δ is the size of the gap that this interaction opens-up.[108, 104, 106] There is also a shift $\epsilon_{2p} \leftarrow \epsilon_{2p} - \Delta$.[109] Approaches[110, 109, 103] using a multiband tight-binding model (see Sec. 2.4.2) also reproduce Eqn. (2.66) near the Dirac points and find the effective next-nearest neighbor contribution in the STB model to be

$$\mathcal{H}_{\mathrm{ISO}} = \frac{i\Delta}{3\sqrt{3}} \sum_{\langle\langle ij\rangle\rangle\alpha,\sigma\tau} c^{\dagger}_{i\alpha\sigma} \nu_{ij} s^{z}_{\sigma\tau} c_{j\alpha\tau}, \tag{2.67}$$

where the σ and τ indeces label the true spin and Δ represents the strength of the intrinsic spin-orbit coupling term and the factor $\nu_{ij} = \pm 1$ is for next-nearest neighbor hops which make a left(right)-hand turn on the honeycomb matrix, see Fig. 2.7.[106] The strength of this intrinsic spin-orbit coupling ($\sim \xi^2$) is thought to be rather small, due to the weakness of the atomic intra-atomic spin-orbit coupling of the carbon atom $\xi \approx 4$ meV.[103]

In a purely two-dimensional form, Eqn. (2.64) can also be rewritten as a Rashba spin-orbit (RSO) interaction

$$V_R^{2D} \sim \nabla_z V(z) (\mathbf{p} \times \mathbf{s}) \cdot \hat{z}. \tag{2.68}$$

In practice the potential gradient $\nabla_z V(z) \sim eE_z$ and hence is controlled by and applied electric field perpendicular to the graphene surface E_z. So the Rashba spin-orbit coupling relates how the spin-orbit coupling can be tuned by external

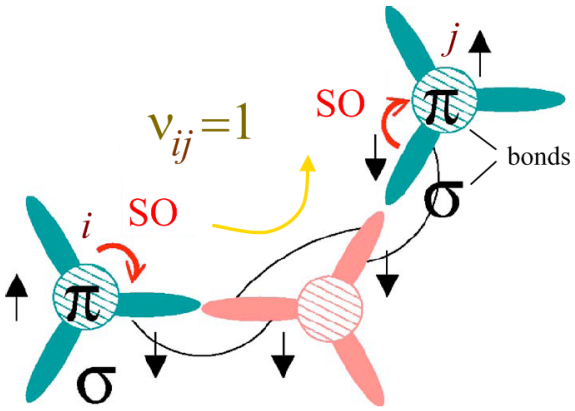

Figure 2.7: A sketch of the next nearest-neighbor processes leading to an effective intrinsic term in the π band of graphene. Transitions are drawn in red, and as indicated by SO, they are mediated by the intra-atomic spin-orbit coupling. Adapted from [103].

fields. This can also be thought of as the lowest order approximation to the local Stark effect that splits degenerate atomic angular momentum states through the application of an external field.

The π-band tight binding equivalent of Eqn. 2.68 is the nearest neighbor term,

$$\mathcal{H}_R = i\,\frac{2\Lambda}{3}\sum_{\langle ij\rangle\alpha\sigma} c^{\dagger}_{i\alpha\sigma}\hat{z}\cdot\left(\mathbf{s}_{\sigma\tau}\times\mathbf{d}_{ij}\right)c_{j\bar{\alpha}\tau}, \tag{2.69}$$

where Λ is the Rashba spin-orbit coupling strength, $\vec{s}$ is the Pauli spin matrix vector and $\vec{d}_{ij}$ is the unit vector that points from the j-site to the i-site.[111] At low energy and to lowest order in Λ the Rasbha Hamiltonian becomes[106]

$$\hat{H}_R = \Lambda(\sigma_x\tau_z s_y - \sigma_y s_x). \tag{2.70}$$

When the Rashba couplings is included the continuum limit bulk spectrum is

$$\epsilon_{\pm}^{b} = \pm\Lambda + b\sqrt{(vk)^2 + \Lambda^2} \tag{2.71}$$

where $b = \pm 1$. In graphene detailed calculations show that $\Lambda \sim \xi E_z$[109, 103], see Table 2.3.6 and can be larger than Δ at certain field strengths.

ISO 2Δ	RSO Λ ($E_z \approx \frac{50\,V}{300\,nm}$)	Group
2.4 K (20 μeV)	0.5 mK (0.043 μeV)	crude results of Kane & Mele[106]
13.2 mK (1.14 μeV)	129 mK (11.1 μeV)	Hongki Min, et.al.[109]
9.2 mK (0.8 μeV)	-	Y. Yao, et.al. [110]
10 mK (0.86 μeV)	70 mK (6.0 μeV)	D. Huertas-Hernando, et.al.[103]
10.8 mK (0.98 μeV)	99.5 mK (8.55 μeV)	average (2^{nd} order only)

Table 2.1: A comparision of the SO couplings in graphene from literature. Kane & Mele only did a first order perturbation calculation, while the others are second order in perturbation theory.

Remarkably, it has be found that curvature on the graphene sheet can be described by an effective Rashba spin-orbit coupling.[103] This arises in that a curvature breaks the planar symmetry of the in-the-plane π bands and hybridizes them with the σ bands, see Fig. 2.8. Let us say that the graphene sheet has a radius of curvature along the x axis R_x and another along the y axis R_y. Then the result from second-order perturbation theory is the effective Rashba SO coupling has

$$\Lambda_{\text{curve}} \sim \xi a \left(\frac{1}{R_x} + \frac{1}{R_y} \right). \tag{2.72}$$

In is now known that cleaved graphene samples have an undulating surface. The observed ripples seem to be several Å height and a few tens of nm laterally.[91] Taking a value of $R_x \sim R_y \sim 100$ nm, it is estimated that that the curvature induced SO couping can be on the order of $\Lambda_{\text{curve}} = 12.2$ μeV (0.14 K). Thus curvature could induce an effective Rasbha SO coupling on the order of 0.2 K,

which is possibly observable.[103] An open question is how this value is affected by interactions and how local curvature affects edge states.

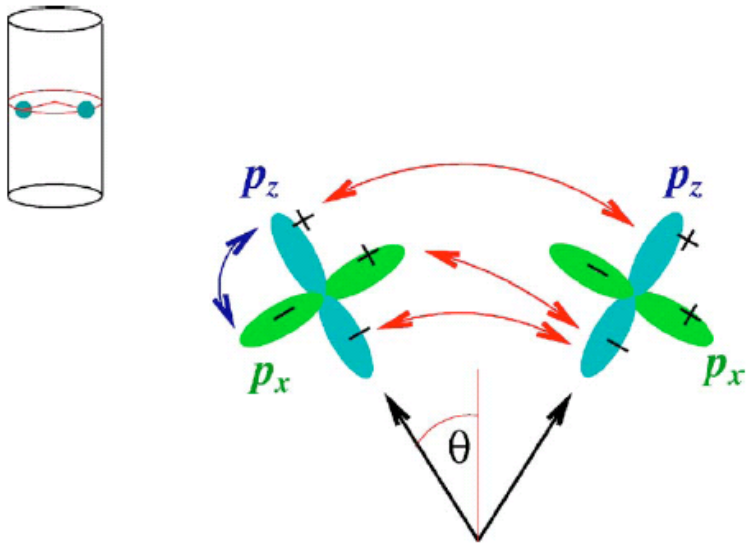

Figure 2.8: An illustration of the $2p_x$ and $2p_z$ orbitals undergoing mixing due to curvature for the analysis of spin-orbit effects in curved carbon nanotubes and graphene. The arrows stand for the different types of hoppings affected. Adapted from [103].

2.3.7 Symmetries of the low-energy Dirac model

The abundance of symmetries in the Dirac model are broken in high-order calculations or when including scattering or interaction effects. First, consider spatial inversion symmetry. In an infinitely flat honeycomb lattice, there are six distinct lines of spatial inversion symmetry. An asymmetry between A and B sites reduces this to three lines. An edge or curvature can further break this symmetry.

Next, consider time reversal symmetry. Recall that the Bloch functions at the K and K' points related by complex conjugation; thus time reversal switches

the two K points. This operator $\hat{T}$ can be represented as

$$\hat{T}\Psi_K = \mathrm{e}^{-i\,\phi}\sigma_z\Psi^*_{K'}, \qquad \hat{T}\Psi_{K'} = \mathrm{e}^{-i\,\phi}\sigma_z\Psi^*_K \tag{2.73}$$

where ϕ is an arbitrary phase factor and this immediately gives that

$$\hat{T}^2\Psi_K = \Psi_K, \qquad \hat{T}^2\Psi_{K'} = \Psi_{K'} \tag{2.74}$$

which is characteristic of the conventional orthogonal symmetry.[99] An external magnetic field or spin-orbit coupling will break time-reversal symmetry.

Next, the Dirac equation is also invariant under a special time-reversal-like operator $\hat{S}$, which can be represented as

$$\hat{S}\Psi = -i\,\sigma_y\Psi^*, \qquad \hat{S}^\Psi = -\Psi, \tag{2.75}$$

where $-i\,\sigma_y$ is an anti-unitary matrix. This symmetry operation corresponds to the time reversal in systems with spin-orbit interaction. Such a system belongs to the symplectic universality class when only $\hat{S}$ constitutes a relevant symmetry.[99, 114] This symmetry can be destroyed by various effects. In fact, it is destroyed by a weak magnetic field and also by the presence of a small amount of scatterers with potential range smaller than the lattice constant a.[116]

How do are these symmetries affect by the physics? When we can neglect inter-valley mixing and confine ourselves to states in each valley, the T symmetry is irrelevant and the special S symmetry becomes relevant. This symmetry prevails even in the presence of impurities unless their potential range is smaller than the lattice constant a. For such longer range scatterers, the effective potential is the same for the A and B sites and does not cause any mixing between valleys. In this case a quantum correction or a weak-localization correction to the Boltzmann conductivity becomes positive and diverges logarithmically.[115] This so-called anti-localization

behavior appears the same as that seen in systems with strong spin-orbit interaction. The presence of short-range scatterers, however, causes the mixing between K and K' points, the S symmetry is violated, but the T symmetry prevails. As a result the system now belongs to the orthogonal universality class. The presence of lattice strain and an gap inducing AB asymmetry also destroys the S symmetry. If the T symmetry is also broken then the system then belongs to the unitary universality class.[99, 115, 116]

By symmetry considerations, how can a gap be opened up in the spectrum near $\mathbf{k} = 0$ origin? Without spin, the degeneracy at the origin is protected by symmetry, and only two possible terms can open up a gap. These two are mentioned in Sec. 2.3.5. One is the A/B asymmetry term $\sim \sigma_z$. This staggered sublattice potential is odd under parity (which interchanges the A and B sublattices). The other term is the K/K' mixing or asymmetry term which goes like $\sim \sigma_z\tau_z$. This term is even under parity, but odd under time reversal (which from above interchanges K and K'). Including spin interactions via the SO couplings opens up other avenues. If the mirror symmetry about the plane is preserved, then the only allowed spin dependent term at $\mathbf{k} = 0$ goes like $\sim \sigma_z\tau_z s_z$, that is intrinsic SO. If the mirror symmetry is broken (either by a perpendicular electric field or curvature of the graphene lattice or by interaction with a substrate) then a Rashba term of the form $(\mathbf{s} \times \mathbf{p}) \cdot \hat{z}$ is also allowed.[106, 103]

2.3.8 Triagonal Warping

A second order correction from the STM is needed to model the triagonal warping of the bands away from ideal Dirac cones as one goes farther from the K point. For

the K point, the second order correction to the Dirac Hamiltonian is

$$\mathcal{H}_2^K = \frac{\hbar v_{\rm F}}{6t_0}\begin{pmatrix} 0 & (k_x + i\,k_y)^2 \\ (k_x - i\,k_y)^2 & 0 \end{pmatrix} = \frac{\hbar v_{\rm F}}{6t_0}(\boldsymbol{\sigma}\cdot\mathbf{k})^2 = \frac{\hbar v_{\rm F}}{6t_0}\left[\sigma_x(k_x^2+k_y^2) + \sigma_y\,k_x\,k_y\right], \tag{2.76}$$

and the correction for the K' point is given by $\mathcal{H}_2^{K'} = -(\mathcal{H}_2^K)^\dagger$. This higher order term gives rise to the trigonal warping of the dispersion, see Fig. fig:triagonalWarp. In the presence of $\mathcal{H}_2$, the special time reversal symmetry is destroyed because $\hat{S}\mathcal{H}_2 = -\mathcal{H}_2$. As a result the system now belongs to the unitary class.[99, 117]

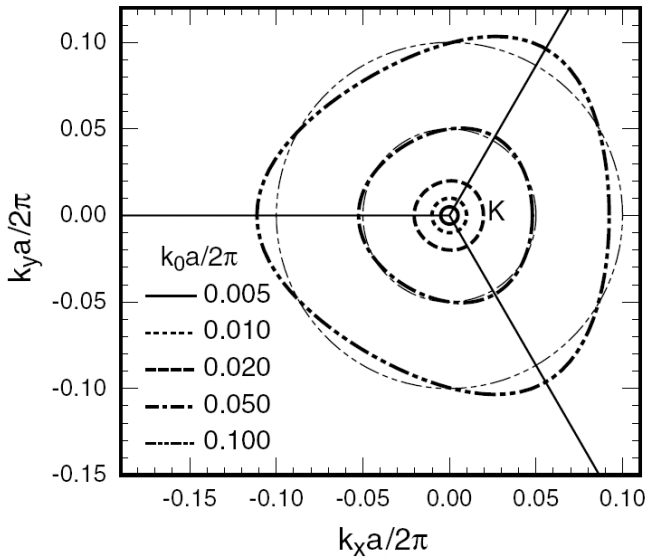

Figure 2.9: The equi-energy lines near the K point. The bold lines take into account the triagonal warping and the lighter line are the Dirac cone contours, from [99].

2.4 Improvements on the STB model

Wallace in his tight-binding study has already considered the second-NN (2NN) interaction, although at the cost of neglecting the overlap matrix.[45] The most detailed calculation was made by Corbato[50] who used a LCAO on a honeycomb

lattice. He employed all five carbon atomic orbitals, and with 2 atoms per unit cell this led to a 10×10 secular equation. The secular equation simplifies, however, because of the different symmetries between the σ and π bands prevent matrix element mixing, hence can be calculated separately. The $1s$, $2s$, $2p_x$ and $2p_y$ orbitals are all even under mirror reflection about the graphene plane, but the $2p_z$ orbital is odd under such a reflection. The crystal potential was a superposition of the atomic potentials and he used overlap integrals out to 9^{th} nearest neighbors and three center potential integrals. Corbato's work shows that the π band calculations are quite accurate with the inclusion of out to only the third nearest neighbors.[3]

2.4.1 Third-Nearest-Neighbor Two Band Model

An extension of the tight-binding interaction radius, has to include the second- as well as the third-nearest-neighbors (3NNs), since the 2NN distance 2.461 Å is very close to to the 3NN distance of 2.842 Å, see Fig. 2.10. To find the 3NN tight-binding dispersion requires that we must calculate the Hamiltonian and overlap matrix elements out to 3NN sites. The E_i's in Eqn. (2.18) are then given by

$$
\begin{aligned}
E_0 &= (\epsilon_{2p} + t_1\, u(\mathbf{k}))\,(1 + s_1\, u(\mathbf{k}))\,, && (2.77)\\
E_1 &= 2s_0t_0\, f(\mathbf{k}) + (s_0t_2 + s_2t_0)g(\mathbf{k}) + 2s_2t_2\, f(2\mathbf{k}), && (2.78)\\
E_2 &= (\epsilon_{2p} + t_1\, u(\mathbf{k}))^2 - t_0^2\, f(\mathbf{k}) - t_0t_2\, g(\mathbf{k}) - t_2^2\, f(2\mathbf{k}), && (2.79)\\
E_3 &= (1 + s_1\, u(\mathbf{k}))^2 - s_0^2\, f(\mathbf{k}) - s_0s_2\, g(\mathbf{k}) - s_2^2\, f(2\mathbf{k}); && (2.80)\\
u(\mathbf{k}) &= f(\mathbf{k}) - 3, \qquad g(\mathbf{k}) = 2u(\mathbf{k}) + u(2k_y - k_x, k_y - 2k_x). && (2.81)
\end{aligned}
$$

The t_1 and t_2 parameters are the interaction energies with the 2NNs and 3NNs respectively, and s_1 and s_2 are the corresponding overlaps. Thus from Eqns.(2.17) and (2.77) we have the tight-binding dispersion in the 3NN approximation. Including the same number of neighbors for the first-principles and tight-binding Hamiltoni-

ans gives good agreement (better than 10^{-2} eV) as seen in Fig. 2.11, where the tight-binding parameters as given in Table 2.2. This difference is partially due to numerical inaccuracies of the *ab initio* calculation, as well as the inherent difficulties of fitting a large number of parameters.

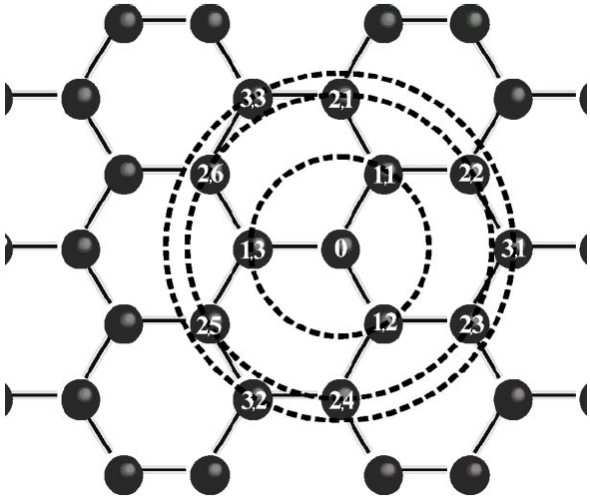

Figure 2.10: The radii of first, second and third nearest neighbors in a graphene honeycomb lattice. Note the close proximity of the second and third nearest neighbors. Adapted from [96].

We can quite accurately reproduce the first-principles results by considering only 3NNs. The difference between the *ab initio* and the empirical band structure in Fig. 2.11 is better than 250 meV along the high-symmetry lines, see bottom panel. For the optical range (transition energies $|\epsilon| < 4$ eV) there is an even better agreement (4 meV), with a slightly different set of parameters as given in Table 2.2. This illustrates how the 3NN approximation can be used to fit well the whole band along the lines connecting the high-symmetry points or just those near the low-energy spectrum.[96]

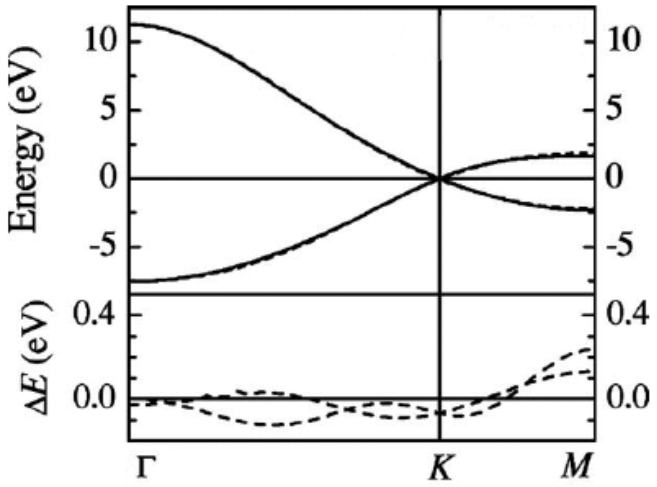

Figure 2.11: Top: the *ab initio* (full lines) and 3NN tight-binding (dashed) band structures for graphene; see Table 2.2 for the tight-binding parameters (ΓKM). Bottom: the difference between the two band structures above. Adapted from [96].

fit	ϵ_{2p}	t_0 [eV]	s_0	t_1 [eV]	s_1	t_2 [eV]	s_2
ΓKM	-0.28	-2.97	0.073	-0.073	0.018	-0.33	0.026
optical	-2.03	-2.79	0.300	0.300	0.046	-0.30	0.039

fit	ΔE_{max} [eV]	ΔE_{max} opt. [eV]
ΓKM	0.25	0.250
optical	1.37	0.004

Table 2.2: The 3NN tight-binding fitting parameters. ΓKM: fit to the first-principles calculation for all $\mathbf{k}$ along the lines connecting the high-symmetry points. optical transitions: only the $\mathbf{k}$ involved with the energy range -4 eV $< \epsilon(\mathbf{k}) < 4$ eV are included in the fit . ΔE_{max} (ΔE_{max} opt.) is the maximal deviation of the tight-binding from the *ab-initio* results for all $\mathbf{k}$ (for only those $\mathbf{k}$ in the optical range), from [96].

2.4.2 A Multiband model

For the full range of physics, of course more bands are needed. When the energy or doping approaches the σ band gap or a more complete set of interband transitions is needed or there are the presence of symmetry breaking effects that mix the π and σ bands then the STB model does not suffice. So let us next consider how to construct the tight-binding model of the σ bands in graphene. Recall from Sec. 1.2 that there are three sp^2 hybridized orbitals per carbon atom that form the strong covalent σ bonds that make the in-plane strength of graphene so great. The tight-binding model including both σ and π bands can be written in a LCAO involving the $2s$, $2p_x$, $2p_y$ and $2p_z$ atomic orbitals for the two atoms of the units cell, thus the are six additional bands added to those seen in the STB model above. We calculate these bands using 8×8 matrices to solve the secular equation Eqn. 2.14. We will find that there are three σ bonding bands below the Fermi level and σ^* antibonding bands above it.

In the NN approximation the onsite sub-blocks are

$$\mathcal{H}_{AA} = \begin{pmatrix} \epsilon_{2s} & 0 & 0 & 0 \\ 0 & \epsilon_{2p} & & 0 \\ 0 & 0 & \epsilon_{2p} & 0 \\ 0 & 0 & 0 & \epsilon_{2p} \end{pmatrix}, \qquad \mathcal{S}_{AA} = \begin{pmatrix} 1 & 0 & 0 & 0 \\ 0 & 1 & 0 & 0 \\ 0 & 0 & 1 & 0 \\ 0 & 0 & 0 & 1 \end{pmatrix}, \tag{2.82}$$

where ϵ_{2s} and ϵ_{2p} are the orbital energies in the graphene crystal. The matrix elements between the A and B sites requires an evaluation of the different combinations of the $2s$ and $2p$ orbitals that constitute the sp^2 hybridized orbital in different symmetry configurations. Decomposing the $2p_x$ and $2p_y$ orbitals into components parallel and perpendicular to the bond axis, the matrix elements only appear in four non-vanishing combinations, see Fig. 2.12. The matrix elements constructed from these combinations by projecting a $2p_i$ atomic orbital, with its own axis along $\mathbf{p}$,

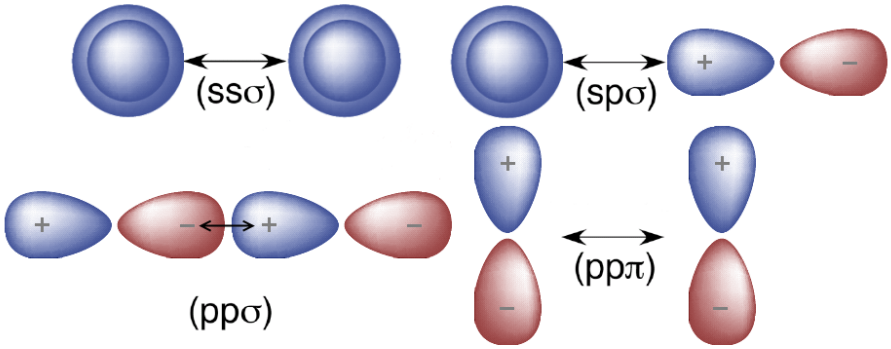

Figure 2.12: The four non-vanishing combinations of orbitals that contribute to the matrix elements between the component projections of the $2s$ and $2p_i$ carbon orbitals.

onto components along directions parallel and perpendicular to the bond axis, with the bond unit vector $\mathbf{d}$ and its normal unit vector $\mathbf{n}$. All three vectors are in the same plane. See Fig. 2.13 for a contribution to a matrix element involving a $2s$ and $2p_i$ orbital.

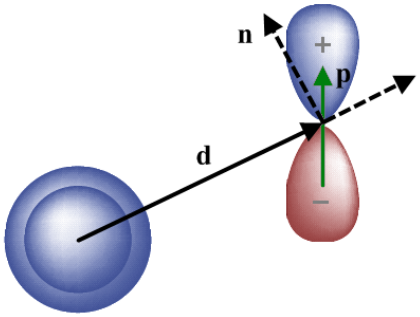

Figure 2.13: Illustrating the projection of a $2p_i$ orbital into directions parallel and perpendicular to the bond axis. The orbital axis is along the unit vector $\mathbf{p}$ and the bond unit vector is $\mathbf{d}$ with its normal unit vector $\mathbf{n}$ in the plane defined by $\mathbf{p}$ and $\mathbf{d}$.

For example, the Hamiltonian matrix element between a $2s$ orbital on one site and a $2p_i$ orbital on another (like that shown in Fig. 2.13) is

$$\langle 2s|\mathcal{H}|2p_i\rangle = \langle 2s|\mathcal{H}\left[(\mathbf{p}\cdot\mathbf{d})|2p_d\rangle + (\mathbf{p}\cdot\mathbf{n})|2p_n\rangle\right]. \tag{2.83}$$

For terms involving two $2p_i$ orbitals there will be two axis unit vectors $\mathbf{p}$ and $\mathbf{p}'$ and two normal unit vectors $\mathbf{n}$ and $\mathbf{n}'$; these terms can be put into the same form by using the relation $(\mathbf{p}\cdot\mathbf{n})\mathbf{n} = \mathbf{p} - (\mathbf{p}\cdot\mathbf{d})\mathbf{d}$. Evaluating all the contributions for NN sites then gives the general result for the Hamiltonian matrix:

$$\mathcal{H}_{AB} = \sum_{i=1}^{3} \begin{pmatrix} h_{ss\sigma} & d_{i,x}h_{sp\sigma} & d_{i,y}h_{sp\sigma} & d_{i,z}h_{sp\sigma} \\ -d_{i,x}h_{sp\sigma} & d_{i,x}^2 h_{pp\sigma} + (1-d_{i,x}^2)t_0 & d_{i,x}d_{i,y}(h_{pp\sigma} - t_0) & d_{i,x}d_{i,z}(h_{pp\sigma} - t_0) \\ -d_{i,y}h_{sp\sigma} & d_{i,y}d_{i,x}(h_{pp\sigma} - t_0) & d_{i,y}^2 h_{pp\sigma} + (1-d_{i,y}^2)t_0 & d_{i,y}d_{i,z}(h_{pp\sigma} - t_0) \\ -d_{i,z}h_{sp\sigma} & d_{i,z}d_{i,x}(h_{pp\sigma} - t_0) & d_{i,z}d_{i,y}(h_{pp\sigma} - t_0) & d_{i,z}^2 h_{pp\sigma} + (1-d_{i,z}^2)t_0 \end{pmatrix}, \tag{2.84}$$

where the four contributions are found in Table 2.3, the sum is over the three NN B sites to the A site, and the order of the rows an columns is $2s$, $2p_x$, $2p_y$, and $2p_z$ going from right to left and top to bottom respectively. The transfer matrix is constructed similarly with the s parameters in Table 2.3 used instead. This result is quite general and the inclusion of the z-component allow for the inclusion of curvature effects or a perpendicular electric field. It has been found that curvature in graphene effectively acts like a spatially varying Rashba coupling in graphene at low energy.[103] For a flat graphene sheet we have from the unit cell in Fig. 2.1 that $\mathbf{d}_1 = (0,-1,0)$ and $\mathbf{d}_{2/3} = \frac{1}{2}(\mp\sqrt{3},1,0)$. When all the matrix elements of the 8×8 matrices are found then the secular equation is used to solve for the bands. [4]

2.5 Interaction Effects in Graphene

The effect of electron-electron interactions is not included in the tight-binding models of graphene, which is based on the one-electron in a potential approximation. The electrons behave as a liquid, so that the band model actually describes the

$\mathcal{H}$	value (eV)	$\mathcal{S}$	value (eV)
$h_{ss\sigma}$	-6.769	$s_{ss\sigma}$	0.212
$h_{sp\sigma}$	-5.580	$s_{sp\sigma}$	0.102
$h_{pp\sigma}$	-5.037	$s_{pp\sigma}$	0.146
$h_{pp\pi} \equiv t_0$	-3.033	$s_{pp\pi} \equiv s_0$	0.129
ϵ_{2s}	-8.868	ϵ_{2p}	0.000

Table 2.3: The orbital coupling parameters for the π and σ bands in graphene, from [4].

quasi-particle energy spectrum.[119] So the tight-binding band models is adequate to account for the electronic component of the specific heat and the de Haas-Van Alphen effect but inadequate for calculating the diamagnetic susceptibility and cyclotron resonance. Correlation effects in π band graphene have been studied by the Linderberg group[118] using a Hubbard model. The results indicate that the density of states is not appreciably altered, but the properties of the electons far from the zone edge are significantly changed.[3] When electron-electron interactions are included, doped graphene represents a new type of many-electron problem, distinct from both an ordinary two-dimenisonal electron gas and from quantum electrodynamics. This is because the system has a quasi-relativistic spectrum, which is not bound from below and that the non-interacting eigenstates are chiral eigenstates. Hence, the interacting quasi-particles in graphene have been dubbed a chiral two-dimenisonal electron gas (C2DEG or χ2DEG) and have distinctly different properties from a conventional Fermi liquid.[120] This remains a topic of active and controversial research. The role that interactions have on graphene being a quantum Hall ferromagnet and the ground state of zigzag edge state in graphene ribbons are currently important issues.

Kane and Mele[106, 122] suggest that the long range Coulomb interaction

may substantially increase the gap due to intrinsic SO coupling. To leading order the SO potential is renormalized a diagram that physically represents the interaction of electrons with the exchange potential induced by Δ. This is similar to the gap renormalizations in 1D Luttinger liquids and leads to a logarithmically divergent correction to Δ. The divergence is due to the long range Coulomb interaction, which persists in graphene even accounting for screening.[121] To leading order they find that

$$\Delta(\epsilon) = \Delta^0 \left[1 + g^0/4 + \log(\Lambda^0/\epsilon)\right] \tag{2.85}$$

where the dimensionless Coulomb potential is $g = e^2/(\hbar v_{\mathrm{F}})$ and here g^0 and Δ^0 so are the interactions at cutoff scale Λ^0.[106] The renormalized gap is determined by $\Delta^R \sim \Delta(\Delta^R)$. Using an effective interaction $g^0 = 0.74$, a cutoff $\Lambda^0 = 2$ eV and the average value of $\Delta = 10.8$ mK from Table 2.3.6 leads to $\Delta^R \approx 70$ mK (6 μeV).[122] Also, a recent experiment on the low-field magnetoresistance[91] shows that graphene remains metallic under temperatures as low as $T = 4$ K, which restricts the gap inducing terms to be less than 340 μeV for that kind of substrate. So interactions may enhance the SO couplings by an order of magnitude, yet they still remain relatively low.[103]

2.6 An External Magnetic Field

In an external normal magnetic field electrons undergo circular motion of a radius $r = v_{\mathrm{F}}/\omega_c$ with a cyclotron frequency $\omega_c = \frac{eB}{m_c}$, where m_c is not the effective mass, but a *cyclotron* mass related to how the electrons accelerate in a magnetic field. Consider the two-dimensional massive Dirac equation

$$\mathcal{H}(\mathbf{k}) = \hbar v_{\mathrm{F}}\, \boldsymbol{\sigma} \cdot \mathbf{k} + m_{\mathrm{D}} v_{\mathrm{F}}^2 \sigma_z, \tag{2.86}$$

and in an external field the canonical momentum in MKS units becomes through the Peierls substitution $\mathbf{k} \rightarrow -i\boldsymbol{\nabla} - e\mathbf{A}/\hbar$, where $\mathbf{A}$ is the vector potential. Choosing the Landau gauge where $\mathbf{B} = B\,\hat{z}$ and $\mathbf{A} = Bx\,\hat{y}$ and assuming that the envelope wavefunction is a plane-wave of the form

$$\psi(\mathbf{r}) = \mathrm{e}^{i\,k_y y}\varphi(x).$$

gives the square of the Hamiltonian to be

$$\mathcal{H}^2 = -v_{\mathrm{F}}^2\left(\hbar\partial_x^2 - (\hbar k_y - eBx)^2 - (m_{\mathrm{D}}v_{\mathrm{F}})^2\right). \tag{2.87}$$

Next, this can be rewritten in the form of a one-dimensional harmonic oscillator equation

$$\mathcal{H}^2 = -\frac{(\hbar\partial_x)^2}{2m_c} + \frac{1}{2}m_c\,\omega_c^2(x-X)^2 + (m_{\mathrm{D}}v_{\mathrm{F}}^2)^2, \tag{2.88}$$

where $m_c^{-1} = 2v_{\mathrm{F}}$ and $X = \frac{\hbar k_y}{eB}$.[4] From this the energy of the n^{th} Landau level (LL) would be expected to be

$$\epsilon_{\pm n} = \pm\sqrt{\hbar\omega_c(n+1/2) + m_{\mathrm{D}}^2 v_{\mathrm{F}}^4}. \tag{2.89}$$

Also, the Landau radius is

$$\ell = \sqrt{\frac{X}{k_y}} = \sqrt{\frac{\hbar}{eB}}.$$

This semi-classical result for the energy is *incorrect*! This is because we are dealing with chiral Dirac Fermions. Recall, from Sec. 2.3.4 that as the electron circles about the k-space origin it picks up a phase. This Berry's phase effectively cancels the factor of $1/2$ in Eqn. (2.89), so the actual Landau spectum for a massless

system ($m_{\rm D} = 0$) is

$$\epsilon_{\pm n} = \pm\sqrt{\hbar\omega_c\, n}. \tag{2.90}$$

Thus there is a $n = 0$ LL at $\epsilon = 0$ and the quantization sequence of the Hall conductivity is half-integer relative to the conventional quantization, see Fig. 2.14. This phenomenon is peculiar to monolayer graphene.[99] This was first derived according to Onsager's quantization scheme.[123]

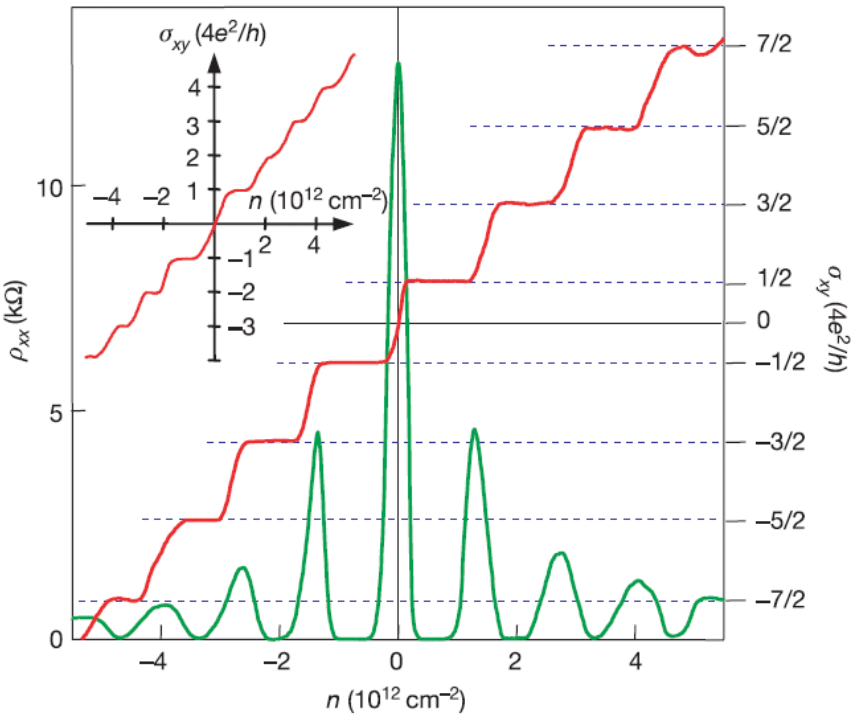

Figure 2.14: The Hall conductivity σ_{xy} and longitudinal resistivity ρ_{xx} of graphene as a function of their concentration at $B = 14$ T and $T = 4$ K. $\sigma_{xy} \equiv (4e^2/h)\nu$ is calculated from the measured dependences of $\rho_{xy}(Vg)$ and $\rho_{xx}(Vg)$ as $\sigma_{xy} = \rho_{xy}/(\rho_{xy}^2 + \rho_{xx}^2)$. Inset: σ_{xy} in a graphene bilayer where the quantization sequence is normal and occurs at integer ν. This shows that the half-integer QHE is exclusive to monolayer graphene, from [61].

Chapter 3

Graphene Ribbons

As can be seen from the work done on bulk graphene, this material's electronic properties can be manipulated in multifarious ways. It can be metallic with a tunable density of states. It can be semiconducting with a gap, and in the case of bilayers the gap is tunable via the gate voltage and doping. Furthermore substrate effects, curvature effects, chemical doping and applied magnetic fields offer further possibilities, such as the surprising room-temperature quantum Hall effect.[1] There has even been some work on superconductivity,[124, 125] spin Hall states,[106] half-metallicity[126] and quantum Hall ferromagnetism in graphene ribbons.[120] Practically, making marketable devices utilizing such phenomena will most likely involve etching epitaxially grown graphene.[1] This etching will cut-out circuit segments that are called graphene ribbons or graphene nanoribbons (GNRs).[128, 127] This introduces two new features. For one, there is quantum confinement due to the finite width of the ribbon, an this can cause gaps and shifts in the spectrum, see Sec. 2.3.5. Secondly, there can be edge state bands that are comprised of new quantum states localized to the edge of the ribbon. As it turns out both of these depend on the geometry of graphene ribbon boundary, that is, the orientation of the graphene plane compared to the line parallel to the ribbon boundary.

The two predominant edge boundaries seen in cleaved crysallites are the armchair and zigzag edge, the same names given to the two kinds of achiral carbon nanotube cross-sections, see Figs 3.1 and 3.2. All zigzag nanoribbons and one third of armchair nanoribbons with a width of $N = 3M - 1$ rows of atoms (M an integer) are metallic, see Fig. 3.2. The remaining armchair and all chiral nanoribbons have oscillating semiconducting gaps that diminish with the width.

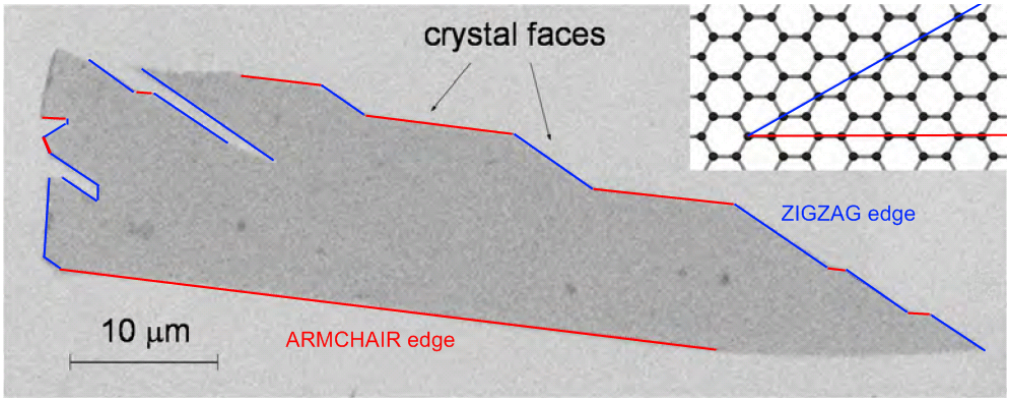

Figure 3.1: A scanning-electron micrograph of a relatively large graphene crystal, which shows that most of the crystals faces are zigzag and armchair edges as indicated by blue and red lines and illustrated in the inset, from [1].

There has been some preliminary work on graphene nanoribbons by Brey and Fertig[129, 130] which in turn build on the works of nanotube researchers like Ando[131] and others[132]. Recall from Sec. 2.3.2 that the effective low-energy theory for each K point is a 2×2 two-dimensional Dirac Hamiltonian:

$$\hat{H}_{\rm D}^{K/K'} = -i\,\hbar v_{\rm F}(\pm\sigma_x\,\nabla_x + \sigma_y\,\nabla_y), \tag{3.1}$$

where the pseudospinor $\psi = (\psi_A, \psi_B)$ is the eigenfunction. Our choice of orientation in Fig. 3.1 ensures that we can use this Dirac Hamiltonian for both armchair and zigzag ribbons, without having to rotate coordinate systems. The physical low

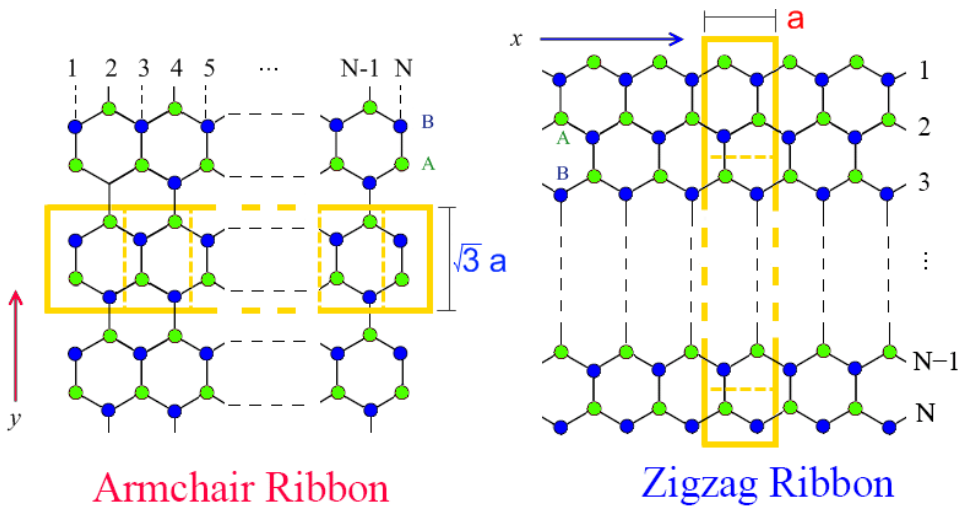

Figure 3.2: (a) armchair and (b) zigzag graphene ribbons. Top and bottom are zigzag edges, left and right are armchair edges. Atoms enclosed in the vertical (horizontal) rectangle represent the "unit strip" used in the calculation of nanoribbons with zigzag (armchair) edges, where the length along the edge is taken to infinity. A unit cell of 4 atoms tile the unit strip indicated by dashed lines. The width of the nanoribbons is a function of the number of zigzag rows (atomic columns), N, in the zigzag (armchair) unit strip, but the wavefunctions may vanish on adjacent row (column) sites not included in the simulation. So here zigzag carriers propagate along the $\hat{x}$ direction and armchair carriers propagate along the $\hat{y}$ direction. This geometry is adopted so that the we can use the same Dirac Hamiltonian universally. Adapted from [129].

energy electronic wavefunction for a graphene ribbon in the Dirac description is

$$\Psi_{\text{phys}}(\mathbf{r}) = \psi^K(\mathbf{r})\, \mathrm{e}^{i\,\mathbf{K}\cdot\mathbf{r}} + \psi^{K'}(\mathbf{r})\, \mathrm{e}^{i\,\mathbf{K}'\cdot\mathbf{r}}. \tag{3.2}$$

The physical wavefunction must vanish in amplitude at the edges:

$$\Psi_{\text{phys}}(\mathbf{r}_\perp = 0) = \Psi_{\text{phys}}(\mathbf{r}_\perp = W) = 0, \tag{3.3}$$

where $\mathbf{r}_\perp$ is the direction normal to the edge. These conditions along with solving the eigenvalue problem for Eqn. (3.1) and normalization are sufficient find the eigenfunctions for finite sized nanoribbons. The BC relates the K and K' components, while the eigenvalue solution relates the pseudospin components. The last step is to determine way that $\mathbf{k}_{\parallel,n} \sim n/W$ is quantized into discrete units. Thus the continuous conical spectrum of bulk graphene is chopped up into a series of equally-spaced, parabolic conic sections that form the GNR spectrum. If the quantization of $\mathbf{k}_{\perp,n}$ is such that the origin at $\mathbf{k} = 0$ is missed then a gap opens up in the graphene nanoribbon spectrum. This is how gaps can open up in the spectrum of graphene nanoribbons due to the quantum confinement of the wavefunction.

3.1 Armchair Ribbons

Armchair graphene ribbons are well described by the low energy Dirac model, but their electric properties are strongly dependent on the width. The geometry of an armchair graphene nanoribbon (AGNR) is illustrated in Fig. 3.2 running along the $\hat{y}$ direction, as well as the unit strip and cells used in the corresponding tight binding calculations. In this orientation the width of the nanoribbon *wavefunction* is related to the number of atomic columns in the ribbon N through the expression $W = \frac{1}{2}(N+1)a$, where N is also twice the number of unit cells uses. Now Eqn. (3.2)

explicitly becomes

$$\Psi_{\rm phys}(\mathbf{r}) = \psi^{K}(\mathbf{r})\,\mathrm{e}^{i\,K_x x} + \psi^{K'}(\mathbf{r})\,\mathrm{e}^{i\,K'_x x}, \tag{3.4}$$

and thus the only way to met the vanishing amplitude BC (3.3) requires the admixing of the valleys at the edges

$$\psi^{K}_{\alpha}(x=0,k_y) = -\psi^{K'}_{\alpha}(x=0,k_y), \qquad \psi^{K}_{\alpha}(x=W,k_y) = -\psi^{K'}_{\alpha}(x=W,k_y)\mathrm{e}^{i\Delta K\,W}, \tag{3.5}$$

where $\Delta K = 8\pi/(3a)$. Note also that since $K_y = K'_y = 0$ that the two Dirac points project onto the origin at $\mathbf{q}$

3.1.1 The Wavefunction of an Armchair Graphene Nanoribbon

Squaring the Hamiltonian, Eqn. (3.1), gives that $-\nabla^2\psi = (\epsilon/\hbar v_{\rm F})^2\psi = k^2\psi$, implying a plane wave solution. The solution to the eigenvalue problem of Eqn. (3.1) for right movers gives

$$\psi^{K/K'} = \pm \begin{pmatrix} 1 \\ b\,\mathrm{e}^{i\,\theta} \end{pmatrix} \mathrm{e}^{\pm i\,k_{x,n}x}\mathrm{e}^{i\,k_y y}, \tag{3.6}$$

with the eigenvalues $\epsilon_{b,n} = b\,\hbar v_{\rm F} k_n$, where $b = \pm 1$ for particle/hole bands, $k_n = \sqrt{k_{x,n}^2 + k_y^2}$ and recall that $\tan(\theta) = k_x/k_y$.

The sequence of $k_{x,n}$ is determined by the second BC (3.5):

$$\mathrm{e}^{2i\,k_{x,n}W} = \mathrm{e}^{i\,\Delta K W} \qquad \Rightarrow (2k_{x,n} - \Delta K)W = 2\pi\,n, \tag{3.7}$$

where n is an integer. For AGNRs N is the number of atomic columns, and the

effective width is $W = \frac{1}{2}(N+1)a$, so the quantization condition can be written as

$$k_{x,n} = \frac{\pi}{W} n, \qquad \text{for} \quad (N+1) \mod 3 = 0, \tag{3.8}$$

$$k_{x,n} = \frac{\pi}{W}\left(n - \frac{1}{3}\right), \qquad \text{for} \quad (N+1) \mod 3 = 1, \tag{3.9}$$

$$k_{x,n} = \frac{\pi}{W}\left(n + \frac{1}{3}\right), \qquad \text{for} \quad (N+1) \mod 3 = 2, \tag{3.10}$$

which has a minimum value for $n = 0$. Such wavefunction solutions are pictured in Fig. 3.3.

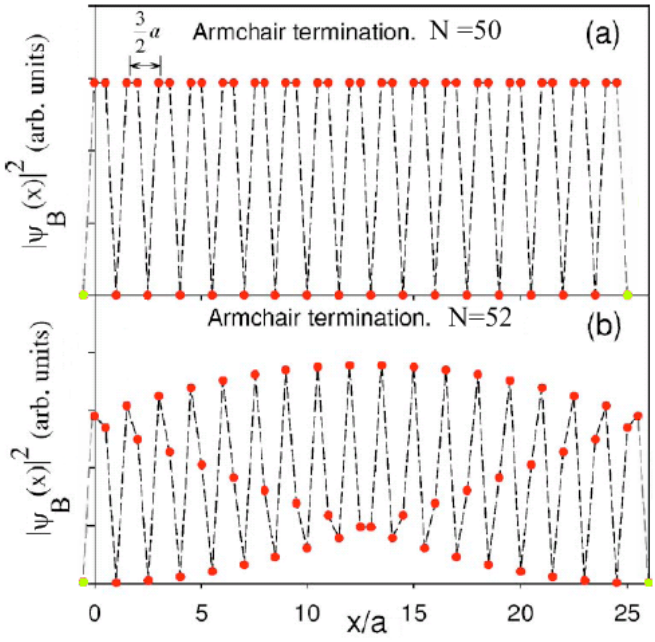

Figure 3.3: Tight-binding solutions of of the form of Eqn. (3.6) for the metallic $N = 50$ and semiconducting $N = 52$. The yellow circles are atomic sites not included in the simulation where the wavefunction amplitude goes to zero. Adapted from [129].

3.1.2 Semiconducting Armchair Graphene Nanoribbons

Thus, we see that the breaking of the continuous symmetry, caused by quantum confinement, leads to the spectrum missing the K points at $\mathbf{k} = 0$; opening a gap. From the conical Dirac spectrum we may estimate this gap for AGNRs to be

$$\delta_a = \epsilon_{\rm D}(k_x = 0, k_y = 0) = 0, \qquad \text{for } (N+1) \mod 3 = 0, \tag{3.11}$$

$$\delta_a = \epsilon_{\rm D}(k_x = \pm\frac{\pi}{3W}, k_y = 0) \approx \hbar v_{\rm F}\frac{\pi}{3W} = \frac{\pi\, t_0 a}{2\sqrt{3}(N+1)}, \qquad \text{for } (N+1) \mod 3 = 1, 2. \tag{3.12}$$

So as with CNTs a third of all AGNRs are semiconducting, see Fig. 3.4.

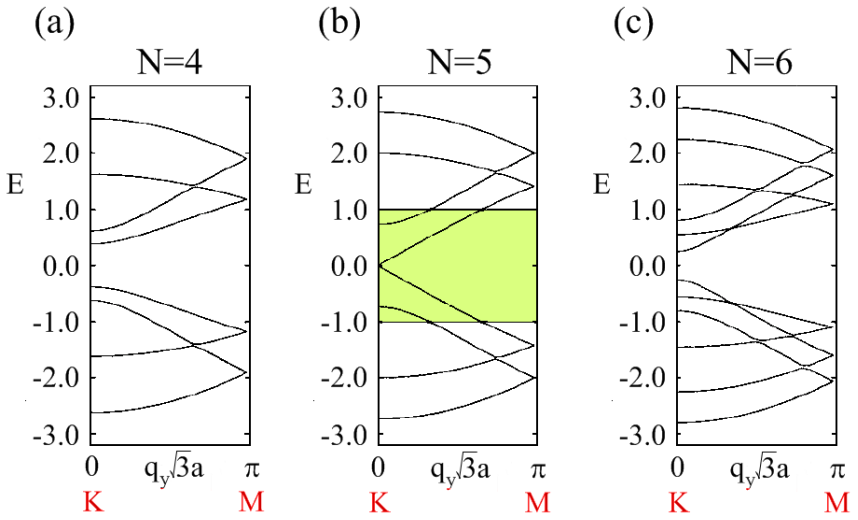

Figure 3.4: Calculated band structure $E(q_y)$ of armchair ribbons of various widths @$N = 4$ (a), 5 (b), and 6 (c). The NN TBM uses $t_0 = 2.7$ eV and is fit to the ± 1.0 eV region shown in light gold. Note that (b) is metallic while (a) and (c) have a semiconducting gap. Adapted from [128].

Now, a more accurate approximation can be obtained from using the NN tight-binding fit to the low energy spectrum in Eqn. (2.33). This takes into account the triagonal warping of the bands which causes the spectrum radially out from the

K points to be lowered, hence decreasing the gap. In respect to the NN STB model, then the *exact* expression for the gap is

$$\begin{aligned}
\delta_a &= \epsilon_{NN}(k_x = 0, k_y = 0) = 0, \qquad \text{for}(N+1) \mod 3 = 0, \qquad (3.13)\\
\delta_a &= |\epsilon^{K'}_{NN}(k_x = \pm\frac{\pi}{3W}, k_y = 0)| \\
&= t_0 \left| 1 - \cos\left(\frac{\pi}{3(N+1)}\right) - \sqrt{3}\sin\left(\frac{\pi}{3(N+1)}\right)\right|, \\
&\qquad\qquad \text{for}(N+1) \mod 3 = 1, 2. \qquad (3.14)
\end{aligned}$$

These semiconducting gaps are illustrated in Fig. 3.5.

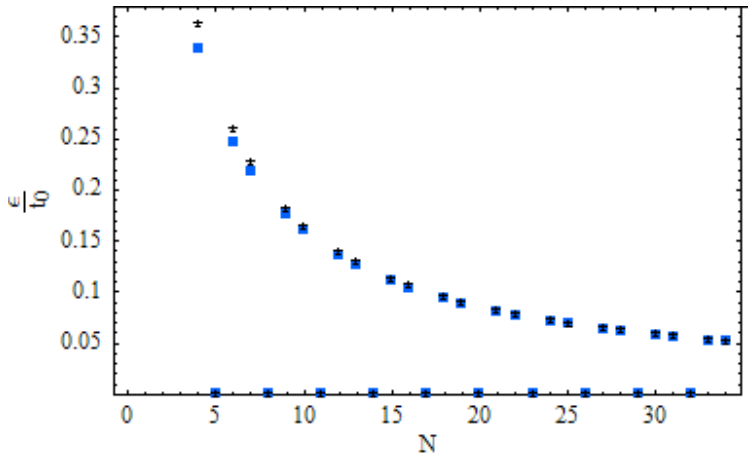

Figure 3.5: The semiconducting gap in AGNR as a function of N. The Dirac approximation [black asterisks] is compared with the *exact* NN tight-binding result as calculated from Eqn. (2.33) [blue boxes]. The gap vanishes for $(N+1)mod3 = 0$.

In review, the AGNRs are well-described by the low energy description near the Dirac points. The spectrum is linear and the wavefunctions are simple plane-waves, there are no edge states. The electronic features are similar to CNTs where a third of the ribbons are metallic and the rest have a semiconducting gap. For very narrow ribbons one might construct a Luttinger liquid theory for the lowest energy band. So at first glance AGNRs offer no new interesting physics, since they are so

similar to CNTs.

3.2 Zigzag Ribbons

Graphene ribbons with zigzag edges, or zigzag graphene nanoribbons (ZGNRs), offer a strikingly different kind of physics than that offered by armchair edges. The simple two band model in graphene ribbons with zigzag edges offers "peculiar localized state" solutions near the Fermi level.[127] These edge state bands continue away from the K' point pass through the M point and then symmetrically back to the K point, thus spanning two-thirds of the Brillouin zone in the x-direction, see Fig. 3.6.

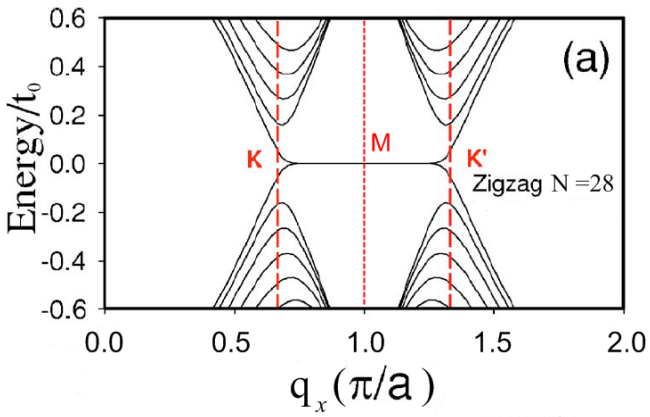

Figure 3.6: The spectrum of a ZGNR with $N = 28$. Note how the K' and K points are projected to different points at $q_x = \frac{2\pi}{3a}$ and $q_x = \frac{4\pi}{3a}$ respectively. The states in the nearly dispersionless band are the peculiar edge states. Adapted from [129].

For the armchair ribbons we could easily construct a continuum model. This is because for every I^{th} column of atoms from the armchair edge, there are both A and B sites and the spacing between columns is a fixed length of $a/2$. The atomic rows of the zigzag ribbon are not so neat. The rows alternate with pure A or B atoms and the distance between atomic rows also alternates between $a/\sqrt{3}$ and $2a/\sqrt{3}$. So a continuum treatment would be cumbersome to calculate with, and a

discrete treatment would a better approach. We will label each horizontal zigzag chain by the label $J = 0, 1, \ldots, N, N+1$. The $J = 0$ and $J = N+1$ chains are not real sites in the simulation, but are where the vanishing amplitude condition applies to the wavefunction. Let's say that there are A sites along the $J = 1$ edge, which then requires B sites along the $J = N+1$ and the vanishing amplitude requirement becomes

$$\psi_B^{K/K'}(J = 0) = 0, \qquad \psi_A^{K/K'}(J = N+1) = 0, \tag{3.15}$$

since the physical wavefunction is a function of oscillating terms with K_x andK'_x; so we expect the different valley solutions to be the same, except that $k_x \to -k_x$. The boundary conditions treat the two sublattices asymmetrically which leads to edge states and gives rise to a single special mode in each valley. Also we see that time reversal symmetry is effectively violated in the sense that we find and imbalance between left-movers and right-movers, as long as there are no short range scatters that mix the valleys.[134]

Consider a ribbon with an edge at $J = 0$ and assume a right moving plane-wave solution along the edge:

$$\psi(J) = \mathrm{e}^{i\, q_x x}\, \phi(J). \tag{3.16}$$

Next, writting out the Schrödinger equation from the tight-binding model gives

$$\epsilon\phi_A(J) \quad = -t_0(\psi_B(J-1) + Q\,\psi_B(J)), \tag{3.17}$$

$$\epsilon\phi_B(J) \quad = -t_0(\psi_A(J+1) + Q\,\psi_A(J)), \tag{3.18}$$

where t_0 is treated as a positive constant, $Q = 2\cos(q_x a/2)$ and these apply for the physical sites at $J = 1 \ldots N$. From these we see that we can recursively relate $\phi_A(J) \sim (\phi_A(1))^J$ and $\phi_B(J) \sim (\phi_B(N))^{-J}$.

3.2.1 Semi-infinite Zigzag Ribbons

From the recursion in a semi-infinite edge state solution as $N \to \infty$ we can take $\phi_B(J) = 0$ for all J and then Eqn. (3.17) also requires that $\epsilon = 0$ for these kind of edge state solutions. Now let us attach amplitudes $|\psi_A(J)|$ to the A sites, as in Fig. 3.7. Then from Eqn. (3.18) we have that

$$x = -2\cos(q_x a/2)\, \mathrm{e}^{i\, q_x (n-1/2)a}, \tag{3.19}$$

$$y = -2\cos(q_x a/2)\, \mathrm{e}^{i\, q_x (n+1/2)a}, \tag{3.20}$$

$$x + y + z = 0, \Rightarrow \tag{3.21}$$

$$z = (2\cos(q_x a/2))^2\, \mathrm{e}^{i\, q_x\, na}. \tag{3.22}$$

By observation, the solution for a semi-infinite ribbon ($J > 0$) is

$$\psi(J) = \begin{pmatrix} (-2\cos(q_x a/2))^{(J-1)} \\ 0 \end{pmatrix} \mathrm{e}^{i\, q_x x}. \tag{3.23}$$

and for this to be normalizable requires that $|2\cos(q_x a/2)| < 1$, which is true for $\frac{2\pi}{3} < |q_x| < \pi$ where indeed the flat bands are seen in Fig. 3.6. In finite width samples there is a small gap near the Dirac points and the edge-state region shrinks a bit, but there are still many localized states near the undoped Fermi level. That there are localized edge states along zigzag edges but not armchair edges is suggested by STM studies on graphite steps.[135]

The wavefunction of the non-vanishing A sublattice sites of a zigzag edge can be normalized on the lattice and we find to be

$$\psi_A(q_x, J) = \sqrt{-1 - 2\cos(q_x a)}(-2\cos(q_x a/2))^{(J-1)} f(q_x) \mathrm{e}^{i\, q_x x}, \tag{3.24}$$

where $f(q_x)$ is some function allowed from a unitary transformation of the wave-

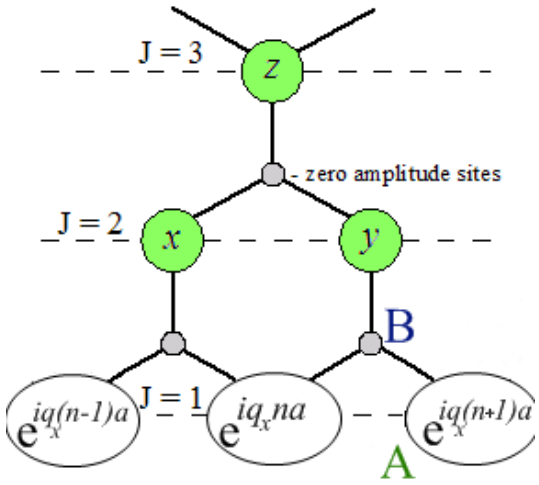

Figure 3.7: Amplitudes on the A sites of a semi-infinite zigzag ribbon.

function (change in basis). We can make use of translational symmetry to partial FT this to get the spatial wavefunction

$$\psi_A(I,J) = \frac{1}{\sqrt{L_x}} \int_{2\pi}^{4\pi} \mathrm{d}\phi \, \mathrm{e}^{i\,\phi I/3} \sqrt{-1-2\cos(\phi/3)} (-2\cos(\phi/6))^{(J-1)} f(\phi), \quad (3.25)$$

where $I = x/a$ and $\phi = 3q_x a$, see Fig. 3.8 for the case of $f(\phi) = 1$. From the TBM, we also find that quite generally for the flat band that if we assume the form $\psi_A(I,J) = (-1)^J \varphi(I,J)$, that we have

$$\varphi(I,J) = \sum_{K=0}^{J} \binom{J}{K} \varphi(I+K-J/2,1). \quad (3.26)$$

Thus, for the flat-band edge states the way the wavefunction falls off into the bulk is completely described by its profile at the edge. It remains to be seen if this can be used to construct a useful solution.

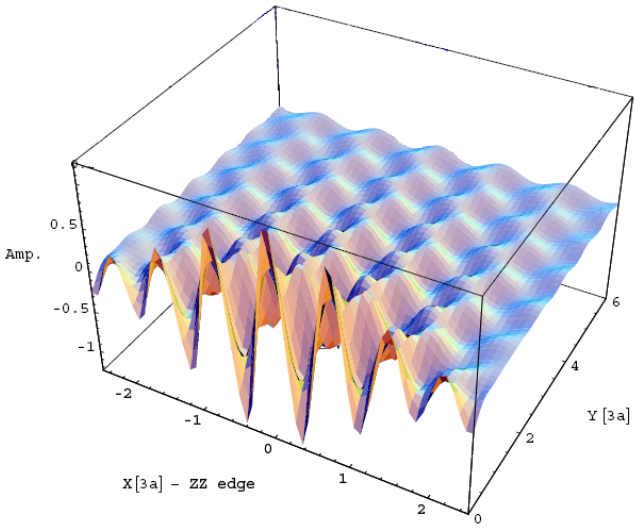

Figure 3.8: A plot of $\psi_A(I, J)$ from Eqn. 3.25.

3.2.2 Zigzag Nanoribbons

A finite-size solution for zigzag nanoribbons has been worked out by Sasaki, et.al.[136] Based on their methods an unnormalized, symmetric solution to Eqns. (3.17) is

$$\psi(J) = (-1)^J \begin{pmatrix} (\sinh\left[\frac{\sqrt{3}}{2}\kappa(N+1-J)a\right] \\ -b\left[\sinh\left(\frac{\sqrt{3}}{2}\kappa Ja\right)\right] \end{pmatrix} \mathrm{e}^{i\,q_x x}. \tag{3.27}$$

The solution for the eigenvalues of the nearly flat bands is

$$\epsilon = \frac{b\,t_0 \sinh\left(\frac{\sqrt{3}}{2}\kappa a\right)}{\sinh\left[\frac{\sqrt{3}}{2}\kappa(N+1)a\right]} \sim b\,t_0\,\mathrm{e}^{-\frac{\sqrt{3}}{2}\kappa Na}, \tag{3.28}$$

which is exponentially vanishing and is zero at the M point and again $b = \pm 1$. Next, the transcendental equation for real κ is

$$Q = \frac{\sinh\left(\frac{\sqrt{3}}{2}\kappa N a\right)}{\sinh\left[\frac{\sqrt{3}}{2}\kappa(N+1)a\right]} \tag{3.29}$$

which as $N \to \infty$ recovers the semi-infinite solution that

$$\mathrm{e}^{-\frac{\sqrt{3}}{2}\kappa a} \to 2\cos\left(q_x a/2\right). \tag{3.30}$$

Near the Dirac points $\kappa \to i\, k_{n,y}$ and the transcendental condition becomes

$$\tau k_x = \frac{k_{n,y}}{\tan\left(\frac{\sqrt{3}}{2}k_{n,y}Na\right)} \quad \Rightarrow \frac{\sqrt{3}}{2}k_{n,y}(k_x = 0) = \frac{n\pi}{N\,a}, \tag{3.31}$$

[129] and the Dirac eigenvalue becomes

$$\epsilon = b\,\hbar v_{\mathrm{F}}\sqrt{k_x^2 + k_{n,y}^2} = \frac{b\,\hbar v_{\mathrm{F}} k_{n,y}}{\sin\left(\frac{\sqrt{3}}{2}k_{n,y}Na\right)} \tag{3.32}$$

So in finite sized ribbons a gap in the zigzag spectrum opens up at the Dirac points with a value

$$\epsilon_{gap} = \epsilon^K(k_x = 0) = \hbar v_{\mathrm{F}}\frac{2\pi}{\sqrt{3}Na}. \tag{3.33}$$

Solutions near the K point are shown in Fig. 3.9 and the energy eigenvalues from the Dirac approximation, Eqn. (3.33), are compared to the tight-binding value in Fig. 3.10. Lastly, Sasaki, et.al.[136] also find that the NNN correction to the zigzag edge state bands is approximately

$$\Delta\epsilon \approx t_1\left(2\cos\left(q_x a\right) + 1\right). \tag{3.34}$$

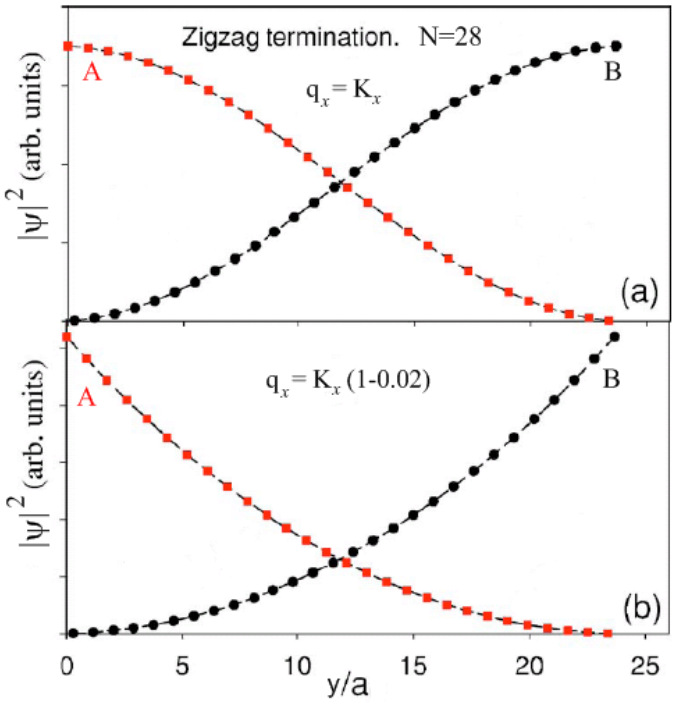

Figure 3.9: Tight-binding solutions of the form of Eqn. (3.27) for a $N = 28$ ZNGR wavefunction amplitude for (a) a bulk state at the K point (b) an edge state at $k_x = K_x(1.0 - 0.02)$. The red (black) circles indicate A(B) sites. Adapted from [129].

3.2.3 Ground State of Zigzag Edge States

One of the most interesting problems with zigzag edge states is to work out the ground state with interactions. The dispersionless bands surely must gains some sort of profile, but the details of its form remain controversial.[137, 126, 138] The almost flat bands should induce magnetic polarization due to electron-electron interactions and lattice distortion due to electron-phonon interaction.[127] Fujita, et.al. first modeled the zigzag ribbon using a mean-field approach by the Hubbard model with an unrestricted Hartree-Fock approximation to glimpse at the overall

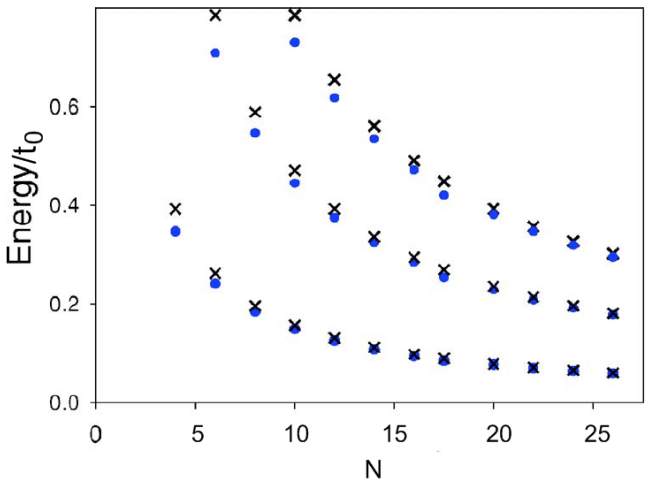

Figure 3.10: Calculated energy eigenvalue at a Dirac point vs N in a ZGNR. The blue dots are tight-binding results, and the black crosses are the results of the Dirac approximation. Adapted from [129].

magnetic structure. Their mean-field Hamiltonian adds a Hubbard-U term:

$$\mathcal{H}_U = U \sum_i \left(\langle n_{i\uparrow} \rangle n_{i\downarrow} + \langle n_{i\downarrow} \rangle n_{i\uparrow} - \langle n_{i\uparrow} \rangle \langle n_{i\downarrow} \rangle \right), \tag{3.35}$$

where the number operator is $n_{i\,s} = c^\dagger_{i,s} c_{i,s}$, and U is the on-site Coulomb repulsion. They found that the sites on the edge have a strong tendency to magnetize, even with small U, see Fig. 3.11. This is not seen in bulk graphite or armchair ribbons. The reason is that the zigzag ribbon has a large density of states at the Fermi level due to the flat edge state bands, so a nonvanishing magnetic moment is possible for arbitrarily low U. For $N = 10$ and $U/t_0 = 0.1$ they found the magnetic profile in Fig. fig:ferrimagneticZZ. This configuration is locally a ferrimagnet, with the different sublattices opposing each other in an unbalance way leaving a net magnetization at the edge, and is globally an antiferromagnet with the magnetization on the different edges is oppositely oriented. This structure forms because only

one sublattice has an amplitude on an edge and opposite edges have amplitudes on opposite sublattices. So in ZGNRs the edge states may have both pseudospin and spin polarization in an interrelated way.[127]

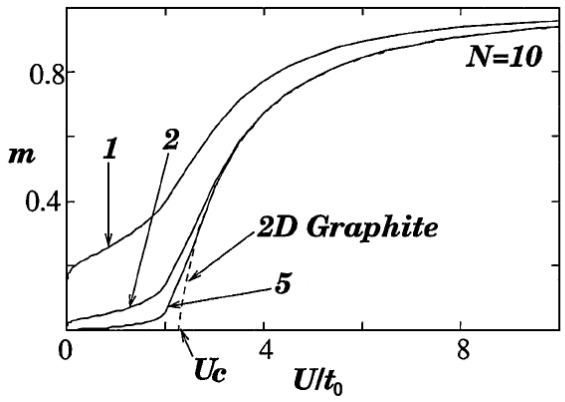

Figure 3.11: The magnetic moment m versus the onsite Coulomb potential U at the $J = 1, 2$ and 5 sites for a ZGNR with $N = 10$. The dashed line shows the result for bulk graphite, were there is no magnetic moment below the critical value of the potential U_c. Note how the magnetic moment persists for the $J = 1$ row even at low U. Adapted from [127].

There have also been a few *ab initio* studies on ZGNRs, with varying results. Son, et.al. have claimed to have found the ground state of undoped ZGNRs to be a half-metal, that is, the carriers all have the same spin.[126] They us an ab initio pseudopotential density functional method to study the spin-resolved electronic structure of ZGNRs. A saw-tooth-type potential perpendicular to the direction of the ribbon edge is used to simulate the external electric fields (E_{ext}) in a supercell. With applied transverse electric fields, the nearly flat edge-state bands associated with one spin orientation close their gap, whereas those associated with the other widen theirs, see Fig 3.13. So they claim that under appropriate field strengths, ZGNRs are forced into a half-metallic state, resulting in an insulating behavior for one spin and a metallic behavior for the other.[126]

Another independent first-principles study of the electronic and magnetic

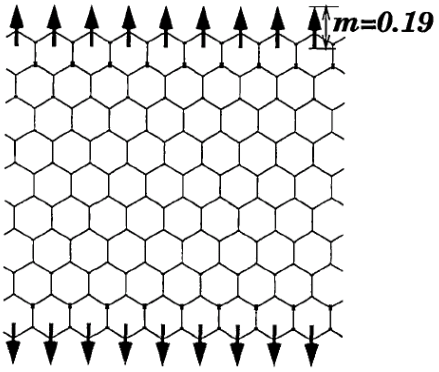

Figure 3.12: The Magnetic texture of a ZGNR with $N = 10$ and $U/t_0 = 0.1$, from [127].

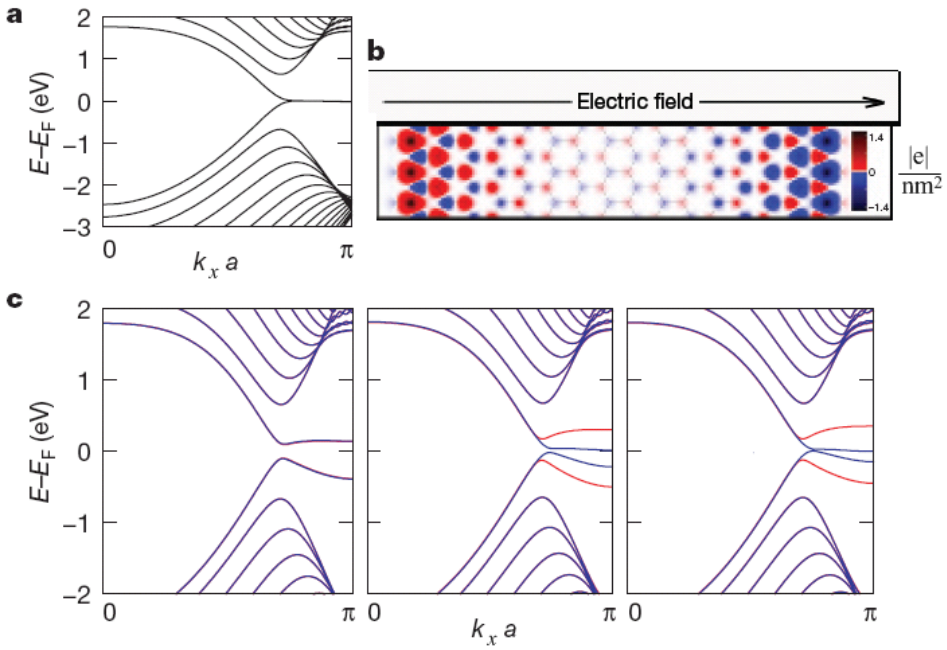

Figure 3.13: In all figures, the Fermi energy (EF) is set to zero. (a) the spin-unpolarized band structure of an $N = 16$ ZGNR. (b) The integrated spatial distribution of the charge difference between the two spin orientations $(\rho_\alpha(r) - \rho_\beta(r))$ for the ground state with no external field. The magnetization per edge atom for is 0.43 μ_B (μ_B = Bohr magneton) with opposite orientations along opposite edges. (c) From left to right, the spin-resolved band structures of an $N = 16$ ZGNR with $E_{ext} = 0.0$, 0.05 and 0.1 V/Å, respectively. The red and blue lines denote the different spin orientations, from [126].

structure of ZGNRs was carried out by Pisani, et.al.[138] The method they chose to use is a hybrid exchange density functional in the B3LYP form which yields an improved quantitative description over other methods. The mixing of non-local and semi-local exchange, present in hybrid-exchange functionals, overcomes the deficiencies of the local density approximation (LDA) and generalized gradient approximation (GGA) in predicting the correct electronic and magnetic ground state in strongly correlated electron systems. In this method they supply the magnetization profile and then solve for the energy of the system. They find for ZGNRs that a solution with magnetization along the edge is always lower in energy that a non-magnetic configuration.[138]

Indeed, in the non-magnetic case they reproduce much of what is known about the zigzag edge states. The electron density is localized mostly at the edges, which peaks at the edges, and decays into the bulk of the ribbon, see Fig. 3.14. By allowing the system to be spin-polarized, they found stable magnetic states, whose spin densities are shown Fig. 3.15. The state depicted in Fig. 3.15(a) is referred to as antiferromagnetic (AF) since the spin moments on one edge are anti-aligned with the spin moments on the opposite edge Fig. 3.15(b) shows the ferromagnetic (FM) configuration where the spin moments on both edges point in the same direction. Both the AF and FM configurations are found to have a total energy lower than the non-magnetic state for all ribbon widths. This is larger for wider ribbons and converges to about 0.38 eV per unit cell at $N \sim 30$.[138]

They find the ground state of the ZGNR to be the AF case, as predicted by the spin alternation rule[139] and formally expressed in Liebs theorem[140] in the framework of a Hubbard model, although the FM case is still relatively stable. Their results extend the validity of the spin alternation rule beyond the approximations of the Hub- bard model. In Fig. 3.16 the band structures of the AF (upper panel) and FM (lower panel) states are presented. The AF solution gives a Slater insulator,

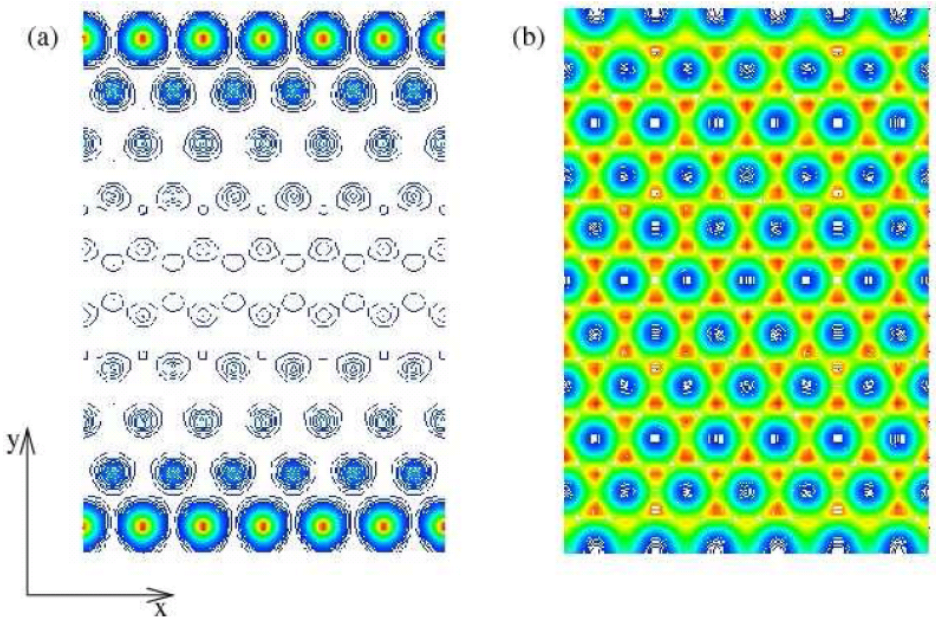

Figure 3.14: Electron density of a non-magnetic $N = 10$ ZGNR for (a) an edge state (b) a bulk state; from [138].

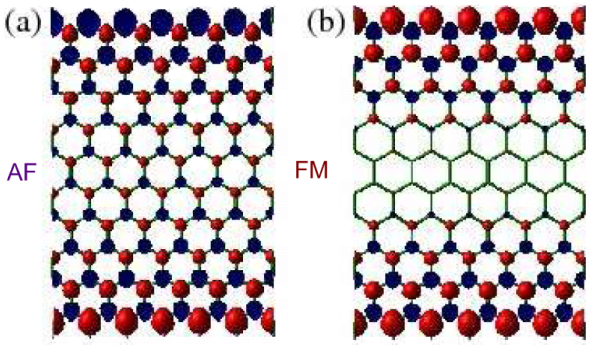

Figure 3.15: The spin density for the antiferromagnetic (AF) case (a) and ferromagnetic (FM) case(b). The red surfaces represents spin up density and the blue surface spin down density, from [138].

and the FM solution gives a Stoner metal.[138]

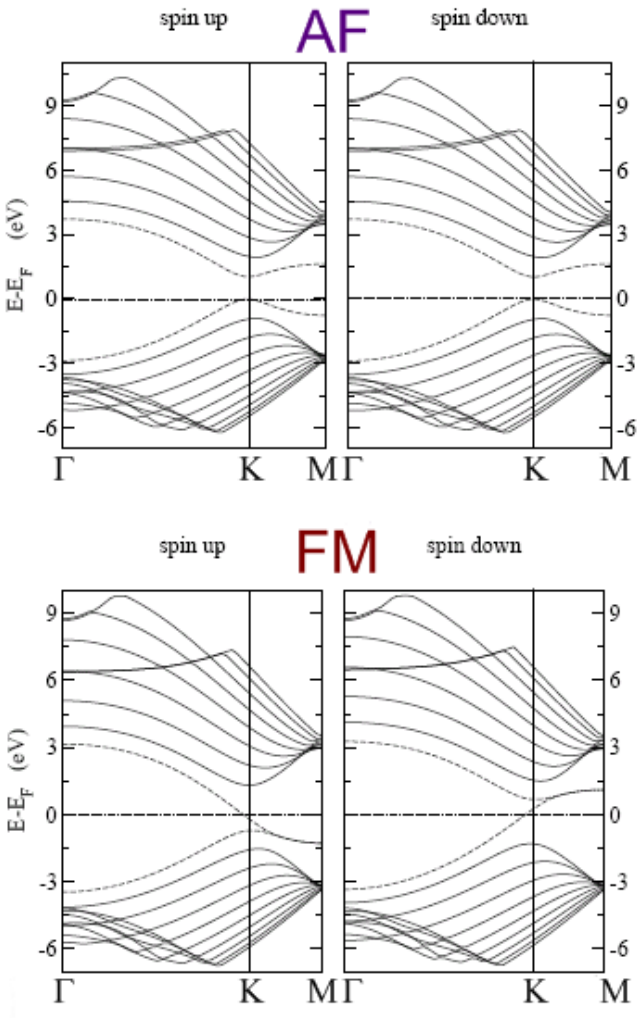

Figure 3.16: Spin polarized band structure of a $N = 10$ ZGNR. The AF case is shown in the upper panels and FM case in the lower panels, from [138].

We (Tami Pereg-Barnea, Murat Taş, Allan MacDonald and myself) have begun a study of the ground state of the zigzag edges states by considering the interactions of the flat-band states, Eqn. (3.24). This is a report of our concrete

work so far. We take the interaction Hamiltonian on the lattice to be

$$\mathcal{H}_v = U_{\rm H} \sum_i n_i n_i + \frac{1}{2} \sum_{i \neq j} V_{ij} n_i n_j, \tag{3.36}$$

where $U_{\rm H}$ is the Hubbard U term which has been studied extensively, V_{ij} is the Couloumb interaction and $n_i = \sum_{i,\sigma} c^\dagger_{i,\sigma} c_{i,\sigma}$ is the charge density on site i and $c_{i,\sigma}$ destroys a spin σ electron on the $i^{\rm th}$ site. Next, assuming that our Hilbert space contains only the zero-energy edge state we can take the lattice annihilation operator as the FT of the flat-band eigenstates:

$$c_{i,\sigma}(k_x, y_i) \to \frac{1}{\sqrt{L_x}} \sum_{k_x} {\rm e}^{ik_x x} \, N(k_x) (-2\cos(k_x a/2))^{y_i} \, c_{k_y,\sigma}, \tag{3.37}$$

where the normalization factor $N(k_x) = \sqrt{-1 - 2\cos(k_x a)}$. Rewriting the Hubbard U part of the Hamiltonian as

$$\begin{aligned} \mathcal{H}_U &= U_{\rm H} \sum_{\sigma,\tau} \sum_{k,p,q} \sum_{y_i} c^\dagger_{i,\sigma}(k, y_i) c_{i,\sigma}(k-q, y_i) c^\dagger_{i,\tau}(p, y_i) c_{i,\tau}(i, y_i) & (3.38) \\ &= \sum_{\sigma,\tau} U(k,p,q) c^\dagger_{k,\sigma} c_{k-q,\sigma} c^\dagger_{p,\tau} c_{p+q,\tau} & (3.39) \end{aligned}$$

where we can explicitly and exactly find the coefficient $U(k,p,q)$ to be given by

$$U(k,p,q) = U_{\rm H} \frac{N(k) N(k-q) N(p) N(p+q)}{1 - 16\cos(ka/2)\cos((k-q)a/2)\cos(pa/2)\cos((p+q)a/2)}. \tag{3.40}$$

We are still endeavoring to use this method to evaluate the Coulomb potential term. If this could be done, then we would be able to project the interaction term on the subspace of zero energy states and diagonalize exactly. In so doing we could solve the ground state of the edge states bands for semi-infinite zigzag ribbons.

3.3 Magnetic field

Continuing the discussion from Sec. 2.6, we now consider a perpendicularly applied magnetic field in graphene nanoribbons. To be concrete let us consider the case of armchair ribbons with $\hat{y}$ along the edge of the ribbon and in this section we will take $x = 0$ being at the center of the ribbon, not from an edge. Doing this we may again choose the Landau gauge for $\mathbf{B} = B\hat{z}$ and $\mathbf{A} = B\,x\,\hat{y}$. Finding the eigenvectors of Eqn. (2.88) then yields the normalized solution

$$\psi^{K}_{\pm n}(\mathbf{r}) = \frac{1}{\sqrt{2\sqrt{A}}} \mathrm{e}^{i\,k_y y} \begin{pmatrix} h_n(x) \\ \pm h_{n-1}(x) \end{pmatrix} \begin{matrix} \text{- A site} \\ \text{- B site} \end{matrix}, \tag{3.41}$$

$$\psi^{K'}_{\pm n}(\mathbf{r}) = \frac{1}{\sqrt{2\sqrt{A}}} \mathrm{e}^{i\,k_y y} \begin{pmatrix} \pm h_{n-1}(x) \\ h_n(x) \end{pmatrix}, \tag{3.42}$$

for a nanoribbon of area A,[141, 142] and

$$h_n(x) = \frac{i^n}{\sqrt{\sqrt{\pi} 2^n n! \ell}} \exp\left[-\frac{1}{2}\left(\frac{x-X}{\ell}\right)^2\right] H_n\left(\frac{x-X}{\ell}\right), \tag{3.43}$$

where again $X = \frac{\hbar k_y}{eB}$, $\ell = \sqrt{\frac{\hbar}{eB}}$,[4] and the n^{th} Hermite polynomial is defined as

$$H_n(\xi) = (-1)^n \mathrm{e}^{\xi^2} \frac{\mathrm{d}^n}{\mathrm{d}\xi^n} \mathrm{e}^{\xi^2}, \tag{3.44}$$

Also, from our tight-binding simulations, we observe that $h_{-1} \neq 0$ or a constant value, but appears as an exponential-like solution, see Fig. 3.17, and we propose the solution:

$$H_{-1}(\xi) = -\mathrm{e}^{\xi^2} \text{“} \left(\frac{\mathrm{d}^{-1}}{\mathrm{d}\xi^{-1}} \mathrm{e}^{\xi^2}\right) \text{”} = -\mathrm{e}^{\xi^2} \int_0^{\xi} \mathrm{d}\zeta\, \mathrm{e}^{\zeta^2} = -\frac{\sqrt{\pi}}{2} \mathrm{e}^{\xi^2}\, \mathrm{Erf}\,\xi, \tag{3.45}$$

which fits the observed wavefunction well. Also, the eigenvalues of the wavefunctions (3.41) and (3.42) are found to be

$$\epsilon_{\pm n}(\xi) = \pm\hbar\omega_c\sqrt{n}, \tag{3.46}$$

which again has the novel $\epsilon_0 = 0$ solution as found earlier in Sec. 2.6.

A perpendicular magnetic field can be included in a tight-binding lattice model of a nanoribbon in a relatively simple way. A nanoribbon can be treated quasi-one-dimensionally, so constructing a magnetic Brillouin zone with plaquetes is *not* necessary. Recall, the Peierls substitution $\mathbf{k} \to -i\boldsymbol{\nabla} - e\mathbf{A}/\hbar$ that transforms a plane-wave solutions as

$$\Psi \to \Psi \exp\left(-i\, 2\pi \mathbf{A}\cdot\mathbf{r}/\phi_0\right),$$

where $\phi_0 = h/e$ is the flux quantum. Now when adding the magnetic field to the tight-binding model, we have to remember that the second quantized form of the tight-binding model, generally speaking, deals with electrons hopping from site i to site j. Let us say that the position of site i is $\mathbf{R}_i$, that of site j is $\mathbf{R}_j$ and thus the hopping vector is $\Delta\mathbf{R} = \mathbf{R}_j - \mathbf{R}_i$. So to add a magnetic field to a nanoribbon calculation requires for each TBM hopping term the additional phase factor:

$$\exp\left[-i\,\frac{2\pi}{\phi_0}\int_0^1 \mathrm{d}\xi\, \Delta\mathbf{R}\cdot\mathbf{A}(\mathbf{R}_i + \xi\Delta\mathbf{R})\right], \tag{3.47}$$

where ξ parameterizes the hopping path from site i to site j.[4] To give a concrete example, the magnetic phase for an armchair graphene nanoribbons becomes

$$\exp\left[-i\,\frac{2\pi B}{\phi_0}\Delta R_y(x_i + \Delta R_x/2)\right]. \tag{3.48}$$

Note, that scaling the width $x \to \xi\, x$ gives the same phase factor as scaling the

magnetic field $B \to \xi\, B$, so simulating macroscopic ribbons is possible by simply increasing the magnetic field accordingly. The magnetic phase and Zeeman splitting are sufficient for an accurate lattice model of graphene nanoribbons in a perpendicular magnetic field. These were used to generate Fig. 3.17.

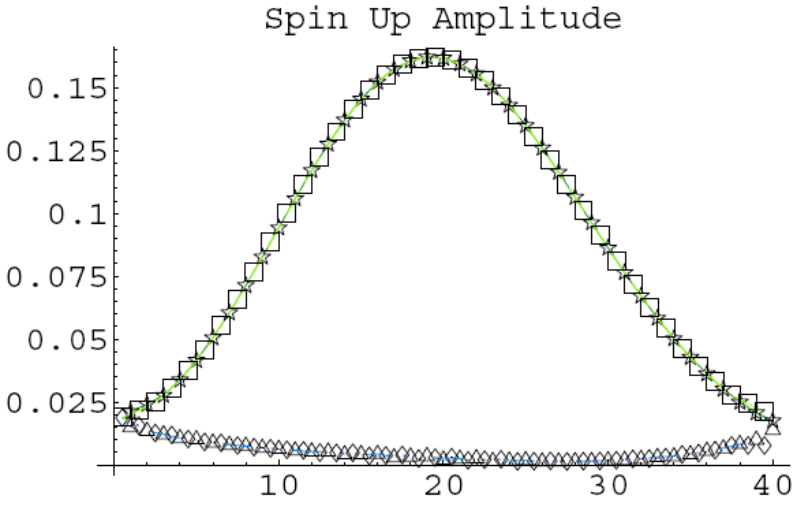

Figure 3.17: The LLL ($n = 0$) wavefunction amplitude in an armchair ribbon near the K point with $B = 100$ T. A sites are connected by green lines and B sites are connected by blue lines. This is at $q_y(\sqrt{3}a) = \pi/15$ and a width of 40 unit cells (N=80).

For zigzag graphene nanoribbons the $A = -B\, y\, \hat{x}$ gauge is prefered and the magnetic phase for the TBM becomes

$$\exp\left[+i\,\frac{2\pi B}{\phi_0}\Delta R_x(y_i + \Delta R_y/2)\right]. \tag{3.49}$$

The dispersion and wavefunction amplitude for a ZGNR flat-band state in the LLL are shown in Figs. 3.18 and 3.19 respectively. Note that the edge state can coexist with the bulk LLL state on different sublattices. This allows for the there to be an electron density at the edge for the LLL states in ZGNRs. Adding the magnetic phase factor, Eqn. (3.49), to the TBM amplitudes for zero energy states, Eqn. (3.19)

gives that the semi-infinite zigzag edge states must obey

$$\psi_A(J+1) = -2\cos\left[\left(q_x - \pi B\, J\, a/(\sqrt{3}\phi_0)\right) a/2\right] \psi_A(J). \tag{3.50}$$

This result means that the flat-bands are mainly affected by a magnetic field in being shifted in and stretched in q_x without changing the localization length much, as shown in Figs. 3.18 and 3.19 (the B sites edges states on the other edge will get shifted differently). This suggests that the conductivity of the edge states in graphene ribbons is not affected as in the same way by a magnetic field as the bulk states.

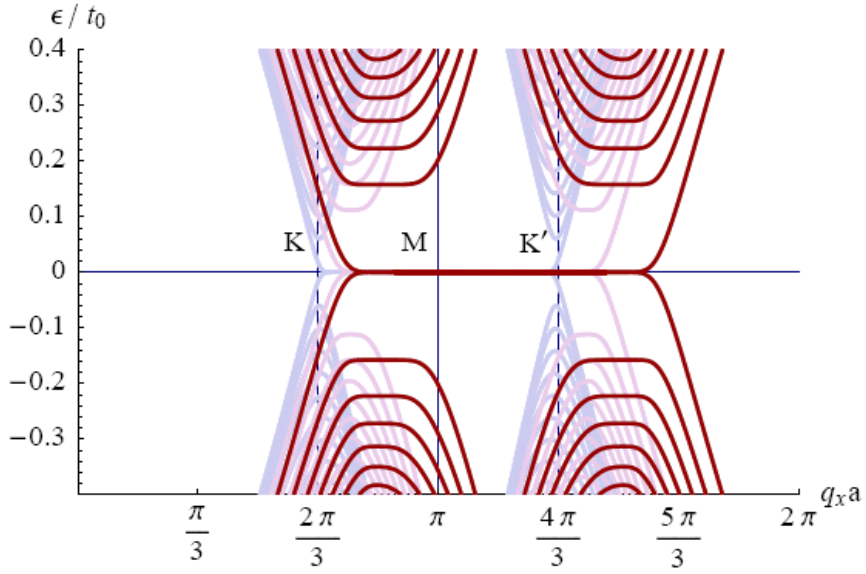

Figure 3.18: The energy bands of an $N = 76$ ZGNR at $B = 1$ T. The dispersions of $B = 0$ T and $B = 0.5$ T are shown in blue and purple pastel colors respectively.

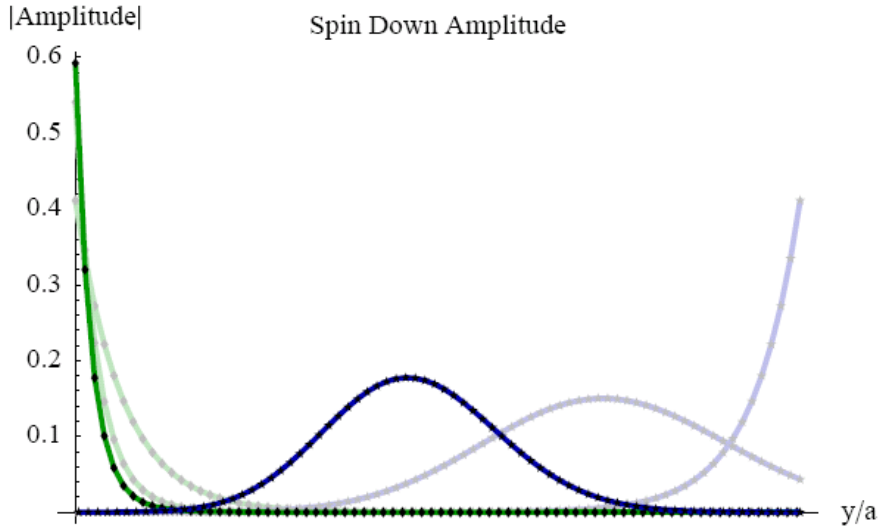

Figure 3.19: The LLL ($n = 0$) wavefunction amplitude in an zigzag ribbon nearer to the K' point with $B = 1$ T. A sites are connected by green lines and B sites are connected by blue lines. This is at $q_x a = 7\pi/6$ (half-way between the M and K' points) and a width of 38 unit cells (N = 76). The wavefunctions of $B = 0$ T and $B = 0.5$ T are shown in pastel colors

3.4 Graphene Devices

Examining the typical armchair and zigzag graphene nanoribbon geometries has revealed a variety of band structures. Graphene nanoribbons are either quasi-one-dimensional metals or semiconductors depending on their edge shape and width. They could be promising candidates for molecular devices, similarly to carbon nanotubes[143], because they have ballistic transport at room temperature.[133] Graphene nanoribbons have some advantages over carbon nanotubes. Two graphene nanoribbon segments with different atomic and electronic structures can be cut out of one source crystal or seamlessly fused together to create metal-metal, metal-semiconductor, or semiconductor-semiconductor junctions without introducing a pentagon and a heptagon (an hence a defect and bound state) into the hexagonal carbon lattice. Also it is relatively easier to add good contacts. Diodes or transistors could be made of graphene nanoribbons, as illustrated in Fig. 3.20. A metal-semiconductor junction made from graphene nanoribbons makes a Schottky barrier and may behave like a Schottky diode. Similarly Schottky gate field-effect transistors, point contacts, quantum dots and Aharonov-Bohm rings may be realized.[133] Graphene rings could even be constructed that form Mobius strips.[144] Graphene strips can also provide efficient field emitters, similar to what has been done with carbon nanotubes. Most applicable to future industry, a complex electronic circuits could be made by etching a larger graphene crystal, most likely epitaxial graphene.

Some work has begun to characterize such devices and so the results seem well undestood, see Figs. 3.21 and 3.22. The observed size of the gap shows good agreement with the expected values. However, the experimental observation shows randomly scattered values around the average E_{gap} corresponding to W with no sign of crystallographic directional dependence. So the detailed edge structure plays a more important role than the overall crystallographic direction in determining the properties of the GNRs. This is consistent with the theory for ideal GNRs that

predicts that E_{gap} depends sensitively on the boundary conditions at the edges. The interplay between the precise width, edge orientation, edge structure, and chemical termination of the edges in GNRs remains a rich area for future research.[145] The main advantage that these graphene devices have over carbon nanotube is the ease to make good quality contacts to each other and the rest of the circuit. A graphene sheet can fan out out to make a good contact with a conventional circuit, nanotubes cannot make good enough contacts to exploit their ballistic transport. It remains an interesting problem to calculate the electronic characteristics of these various graphene devices.[133]

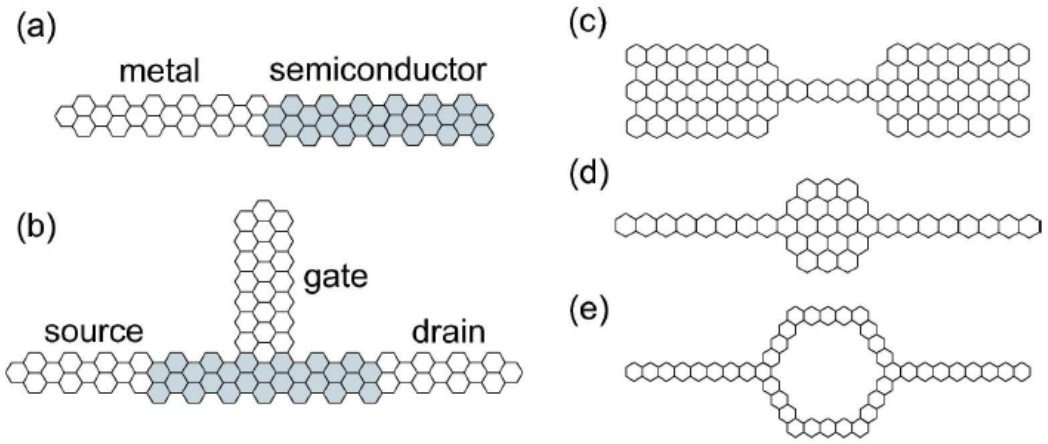

Figure 3.20: Some proposed graphene nanoribbon devices: (a) Metal-semiconductor junction of graphene armchair nanoribbons with different widths (Schottky diode). (b) Transistor composed of the junctions between different nanoribbons (Schottky gate field effect transistor). (c) Point contact. (d) Quantum dot. (e) Aharonov-Bohm ring, from [133].

A further consideration is the macroscopic electrostatics of graphene ribbons in relation to transistor and quantum dot applications. J. Fernández-Rossier *et al.* considered armchair ribbons which can be either semiconducting or metallic.[146] They find that applying a gate voltage V_G equal to only half the band-gap turns semiconducting ribbons into conductors. This affords a on/off ratio much larger

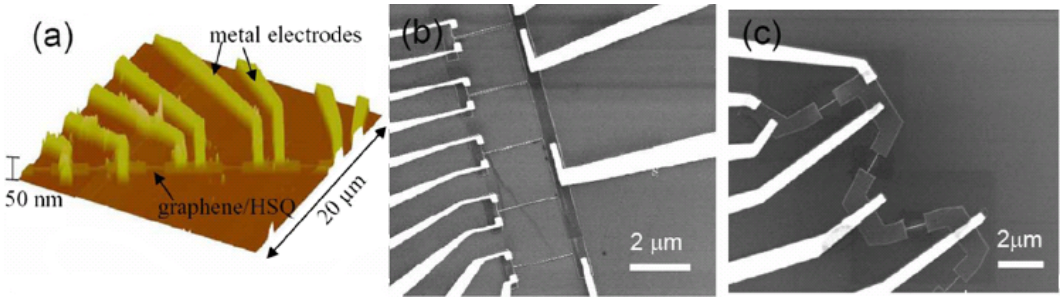

Figure 3.21: (a) Atomic force microscope image of GNRs in device set P3. (b) SEM image of device set P1 with parallel GNRs of varying width. (c) SEM image of device set D2 containing GNRs in different relative crystallographic directions (with relative angle θ) with uniform width, from [145].

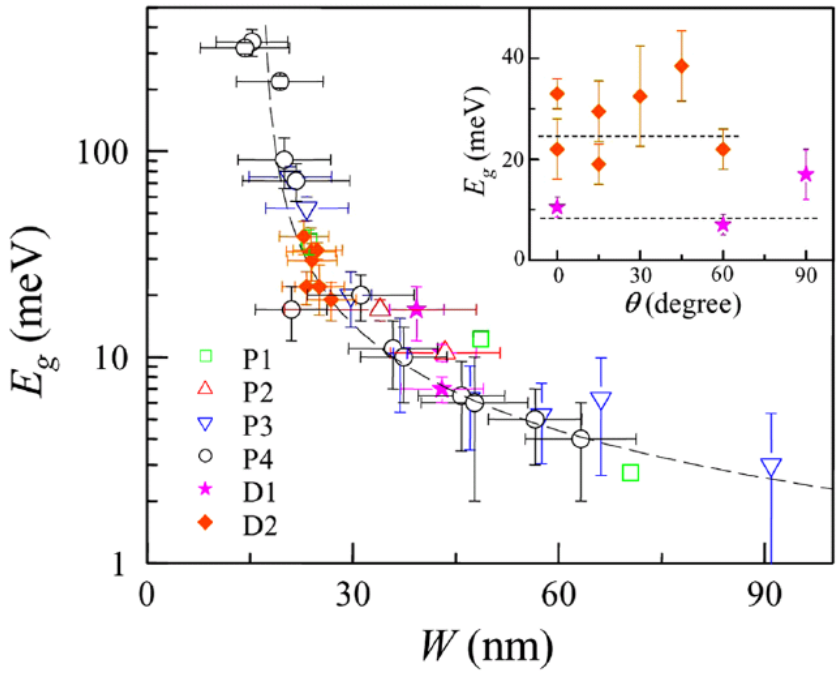

Figure 3.22: E_{gap} vs W for the 6 device sets considered in the study: four (P1P4) of the parallel type and two (D1,D2) with varying orientation. The inset shows E_{gap} vs relative angle θ for the device sets D1 and D2. Dashed lines in the inset show the value of E_{gap} as predicted by the empirical scaling of E_{gap} vs W, from [145].

than that of 2D graphene. In the case of graphene ribbons the classical contribution to capacitance depends on the charge density profile in the ribbon, which can not be measured easily. They find that density of extra carriers is higher in the edges of the ribbons than in the middle. Silvestrov and Efetov have also studied the charge density of gated ribbons find the density from the Poisson equation to be

$$\rho_0 = \frac{\sigma}{\pi\sqrt{(W/2)^2 + x^2}} \tag{3.51}$$

where σ is the two-dimensional average charge density in the ribbon due to the gate potential and x is the transverse direction across the ribbon, see Fig. 3.23.[147] Adding an effective electrostatic potential to the Dirac Hamiltonian $V(x)$ and finding

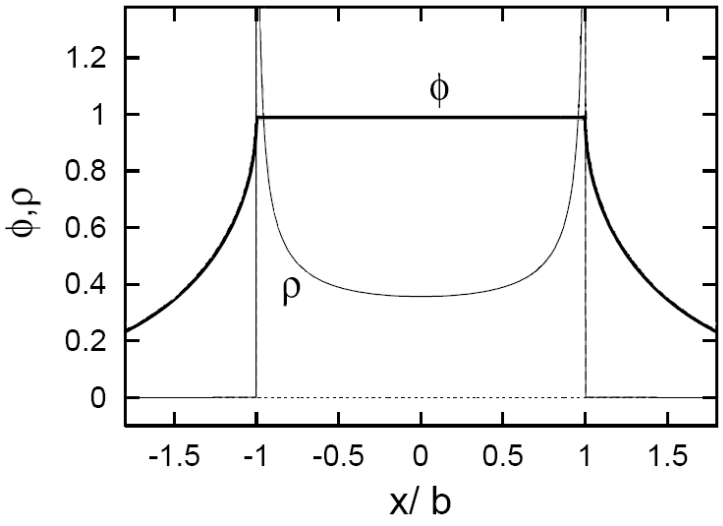

Figure 3.23: Potential (thick lines) and density (thin lines) across the strip of width $W = 0.6$ μm and the gate depth $b = W/2$. A gate voltage $V_G = 100$ V would create in such a ribbon an averaged electron density $\langle n \rangle = 11.6 \times 10^{12}$ cm^{-2}, while an infinite graphene plane gives $n_\infty = 7.2 \times 10^{12}$ cm$^{-}2$, from [147].

the electron density from the Thomas-Fermi approximation implies that

$$V(x) = -\hbar v_{\mathrm{F}} \sqrt{\frac{\sigma}{e\sqrt{(W/2)^2 + x^2}}}. \tag{3.52}$$

A constriction in a biased graphene ribbon works as a quantum dot (QD), see Fig. 3.24. In a perpendicularly applied magnetic field B the Landau level occupation

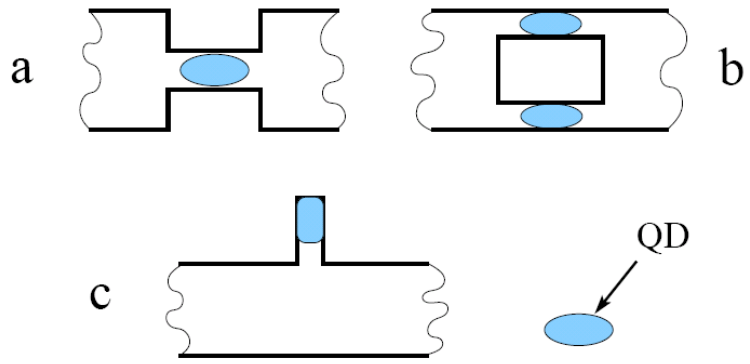

Figure 3.24: Creation of quantum dots via the charge accumulation in narrow constrictions in graphene ribbons. (a). Single QD. (b). Double (parallel) QDs. (c). Side coupled QD. Shaded areas show the puddles of large electron density, from [147].

number goes like

$$N(x) = \frac{\hbar c\, \sigma}{2e^2 B\sqrt{(W/2)^2 + x^2}}. \tag{3.53}$$

Recently, a single electron transistor (SET) made from graphene that operates at room temperature has been made and characterized.[1, 148] The Manchester group used electron-beam lithography and isotropic dry etching to make the transistor, the leads and the gate electrodes all from one sheet of graphene. The SET operates at the smallest possible length scales and manipulating the smallest possible currents, hence is the ultimate realization of a transistor at the nanoscale. The SET is like a quantum dot, with the carriers able to enter and leave the quantum

dot via separate leads. Carriers can only pass through the dot one by one, because of the Coulomb repulsion between the electrons. The SET is switched off by a gate voltage that holds an electron in the quantum dot and is switched on by releasing the electron.[149] A superconducting graphene transistor has also be recently realized by the attachment of two superconducting leads.[125] Monolayer graphene transistors currently have high leakage currents, a problem which may be resolved by either the control of the semiconducting gaps in nanoribbons or by using bilayer graphene.[149]

Lastly, it has been proposed by Kane and Mele that when including the intrinsic spin-orbit coupling (Δ), see Sec. 2.3.6, that graphene can exhibit a spin Hall effect.[106] The spin Hall effect differs from the conventional Hall effect in that it uses an electric field instead of a magnetic field to produce a transverse spin current. Such an effect would allow for the propagation of spin filtered edge states in graphene nanoribbons, which have important consequences for both the transport of charge and spin, especially spintronic applications. For a two terminal geometry (Fig. 3.25(a)), we predict a ballistic two terminal charge conductance $G = 2e^2/h$. For the spin filtered edge states the edge current density is related to the spin density, since both depend on $n_{R\uparrow} - n_{L\downarrow}$. Thus the charge current is accompanied by spin accumulation at the edges. The interplay between charge and spin can be probed in a multiterminal device. In the four terminal geometry of Fig. 3.25(b) a spin current $I^s = eV/4\pi$ flows into the right contact.[106] Importantly, this geometry can be used to measure a spin current. A spin current injected from the left will be split, with the up (down) spins transported to the top (bottom contacts), generating a measurable spin-Hall voltage.[106] The problem to realizing such a useful device in is that the intrinsic spin orbit coupling in graphene is much smaller than that in graphite, which value was initially to support an estimate by Kane and Mele. If there is a way to induce an effective intrinsic spin orbit coupling while simultaneously keeping

the Rashba coupling smaller (see the Sec. 4.4.2), then it would still be possible to utilize the spin-Hall effect in graphene. Presumably the intrinsic spin orbit coupling is greater in graphene bilayers and multilayers, however the existence of spin filtered edge states in such systems remains an outstanding problem.

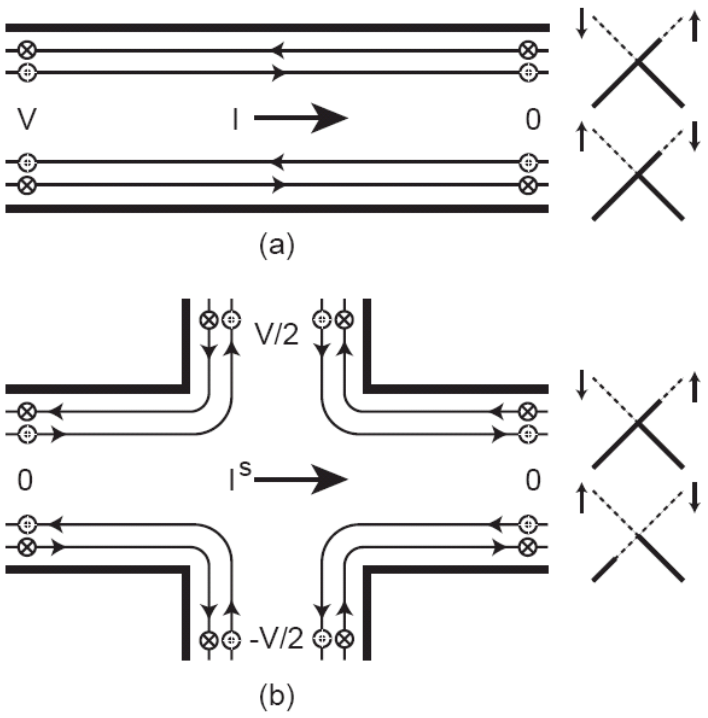

Figure 3.25: Schematic diagrams showing (a) two terminal and (b) four terminal measurement geometries. In (a) a charge current $I = (2e^2/h)V$ flows into the right lead. In (b) a spin current $I^s = (e/4\pi)V$ flows into the right lead. The diagrams to the right indicate how the edge states are populated, from [106].

Chapter 4

Graphene Ribbon Edge States with Spin-Orbit Coupling

The contents of this chapter are partially based on the article: J.E. Hill, Hongki Min, T. Pereg-Barnea, N.A. Sinitsyn, and A.H. MacDonald. "Graphene Ribbon Edge States in Models with Spin-Orbit Coupling", to be published.

4.1 Introduction

Graphene is a honeycomb lattice of carbon atoms in which the low energy quasiparticles can be described by a nearly massless two-dimensional Dirac equation with c replaced by the Fermi velocity v. Interest in graphene has grown because of the sucessful development of techniques which can be used to isolate and contact indivdiual flakes[39, 150, 62, 61] and because of unique electronic properties[106] and high quasiparticle velocities which might make graphene useful as an electronic material.[1] A graphene ribbon can be regarded as a carbon nanotube which has been unwrapped to form a flat ribbon. One interesting aspect of its physics is its edge properties which have been studied for about a decade[127, 128, 137] using

both tight-binding and the continuum limit Dirac models.[132, 151]

Kane and Mele[106] have recently pointed out that the spin Hall effect of a graphene ribbon can be quantizied when a gap is opened in the bulk spectrum by a symmetry allowed intrinsic spin-orbit (ISO) coupling term. The quantized spin Hall effect is related to the properties of edge states which occur at energies inside the bulk gap. (These gaps should be contrasted with the gaps which can appear in very narrow ribbons due to finite width alone[129] and are analogous to the gaps in semiconductor nanotubes.) In this work we study the properties of edge states on both zigzag and armchair edges [see Fig. 4.1] when two different types of spin-orbit coupling terms are added to the Hamiltonian. Both terms create gaps in the bulk which are in some cases accompanied by gapless edge states. We also study for comparison a model with a bulk gap induced by a spin-independent interaction, namely one in which the orbital energies on the honeycomb lattice A and B sites differ. The cases in which edge states do and do not occur for the models we study are summarized in Table 4.1. We have previously presented some preliminary results of this work.[152]

In the following sections we first explain the models we study, and the numerical and analytical edge state solutions that we find and then some topological considerations. We find analytic tight-binding model solutions for zigzag edge states which are dispersive and have amplitudes on both sublattices in the presence of spin-orbit coupling. Using an analytic continuum theory we arrive at solutions for armchair edge states with both intrinsic and Rashba spin-orbit couplings. Finally we discuss the relationship between the existence of edge states and the Chern numbers and Berry curvature distributions of bulk bands.

	$\Delta = 0$ $m = \Lambda = 0$	$\Delta > m$ $\Lambda = 0$	$\Delta < m$ $\Lambda = 0$	$m = 0$ $0 < \|\Lambda\| < \|\Delta\|$
zigzag	✓	✓	✓	✓
armchair	-	✓	-	✓

Table 4.1: Edge state presence (✓) or absence (-) on armchair and zigzag edges for graphene sheets with intrinsic spin-orbit (ISO) coupling Δ, Rashba spin-orbit (RSO) coupling Λ, and a site-dependent energy difference m.

4.2 Spin-orbit coupling models

The π-orbital system in graphene can be described by a one-band tight-binding model on a honeycomb lattice. To explore the new physics introduced by spin-orbit interactions we follow Kane and Mele,[106] by using a tight-binding model (TBM) with spin-dependent next nearest neighbor (NNN) hopping to allow for a phenomenological description of ideal graphene ribbons including spin-orbit coupling. Spin-independent NNN hopping has been neglected. The TBM single-particle Hamiltonian is

$$\begin{aligned} \mathcal{H} &= t_0 \sum_{\langle ij\rangle\alpha,\sigma} c^\dagger_{i\alpha\sigma} c_{j\bar{\alpha}\sigma} \\ &+ \frac{i\Delta}{3\sqrt{3}} \sum_{\langle\langle ij\rangle\rangle\alpha,\sigma\tau} c^\dagger_{i\alpha\sigma} \nu_{ij} s^z_{\sigma\tau} c_{j\alpha\tau} + m \sum_{i,\alpha\beta,\sigma} c^\dagger_{i\alpha\sigma} \sigma^z_{\alpha\beta} c_{i\beta\sigma}, \end{aligned} \tag{4.1}$$

where α and β label the A/B sublattice degree-of-freedom which we refer to as pseudospin, σ and τ indeces label the true spin, $t_0 = -2.7$ eV is the NN tight-binding parameter, and Δ represents the strength of the symmetry allowed spin-orbit coupling term.[106] The factor $\nu_{ij} = \pm 1$ is for second neighbor hops which make a left(right)-hand turn on the honeycomb matrix [see Fig. 4.1]. Here, σ^z and s^z are the Pauli matrices for the A/B pseudospin and true spin respectively. Eqn. (4.1) also includes a *mass* term proportional to m which parameterizes the difference between A and B on-site energies which is not consistent with graphene symmetry

but could in principle arise from weak coupling to a commensurate substrate. It acts like a Zeeman term for the A/B pseudospin (and is equivalent to Semenoff's β).[40] As we shall discuss, the interplay between these two terms has an impact on edge electronic structure.

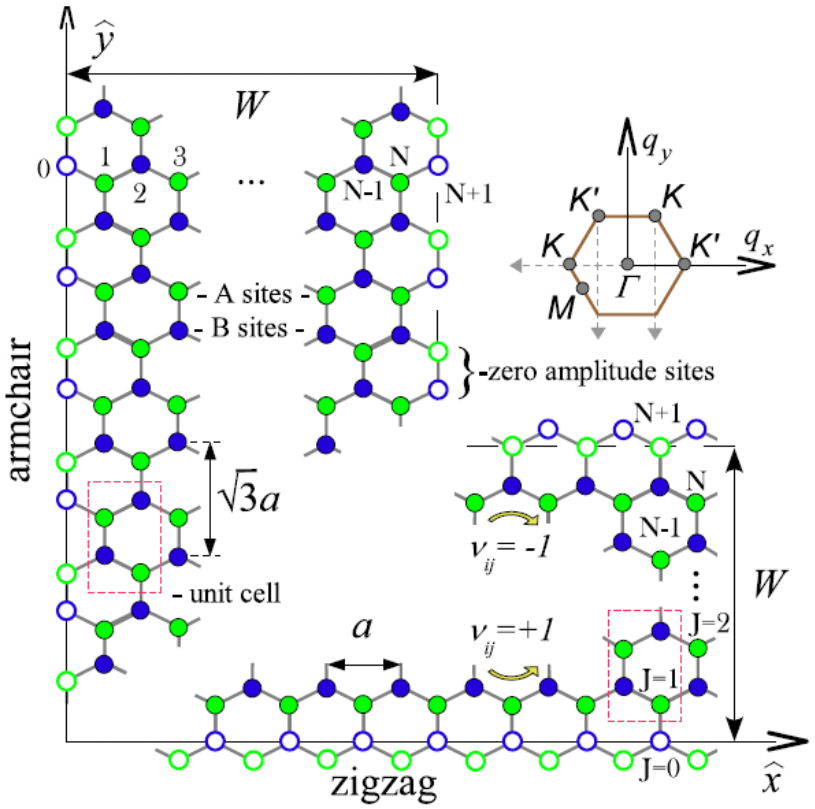

Figure 4.1: Graphene zigzag (armchair) edge and ribbon geometries, where we have chosen a coordinate system such that the $\hat{x}$ ($\hat{y}$) direction is along the edge. The honeycomb lattice Brillouin zone with the same coordinate system orientation is illustrated at the upper right along with the K, K' and M high-symmetry points on its border which are related to important edge state properties. In the intrinsic spin-orbit coupling (ISO) model spin-dependent hopping amplitudes have the opposite sign for right and left-handed second neighbor hops ($\nu_{ij} = \pm 1$). The open circles indicate the closest row of *missing* sites at an edge.

At low energy Eqn. (4.1) reduces to an effective two-valley continuum model

which has the form of a two-dimensional Dirac-like Hamiltonian:

$$\mathcal{H}_D = \sum_{\mathbf{k}} \Psi^\dagger_{\mathbf{k}} \hat{H}_{\rm D}(\mathbf{k}) \Psi_{\mathbf{k}} \tag{4.2}$$

$$\hat{H}_{\rm D} = v(\sigma_x \tau_z \hat{k}_x + \sigma_y \hat{k}_y) + \sigma_z(\Delta \tau_z s_z + m), \tag{4.3}$$

where $\hat{k}_i = -i\nabla_i$, the 8-component wavefunction $\Psi_{\mathbf{k}} = (\Psi^K, \Psi^{K'})$, $\Psi^K = (\Psi^K_A, \Psi^K_B)$ and Ψ^K_A and Ψ^K_B are conventional spinors. Also, $\mathbf{k}$ is measured with respect to $K(K')$ for $\Psi^K(\Psi^{K'})$. Here K and K' are the two inequivalent nodal points of graphene's Brillouin-zone [see Fig. 4.1]. In Eqn. (4.3), the Dirac velocity is $v = (\sqrt{3}/2\hbar)\,|t_0|\,a$ (henceforth $\hbar = 1$), and τ_z is a Pauli matrix distinguishing the K and K' valleys. In calculations we will use the 4-component eigenvector of the upper left (lower right) block of $H_{\rm D}$ and denote it as $\psi^K(\psi^{K'})$.

The dispersion of the bulk states, found by squaring the Hamiltonian, Eqn. (4.3), is

$$\epsilon^2(\mathbf{k}) = (vk)^2 + (s\tau\Delta + m)^2, \tag{4.4}$$

where $\tau = \pm 1$ for the $K(K')$ valley, and $s = \pm 1$ for spin $\uparrow$ ($\downarrow$). The "massless" case is $\Delta = m = 0$. In the presence of ISO only, i.e. $\Delta \neq 0$ and $m = 0$, a gap is added to the bulk Dirac spectrum, while the edge state band become dispersive in the gap [see Figs. 4.2 and 4.3]. When $\Delta = 0$ and $m \neq 0$, a uniform mass is added to the bulk Dirac spectrum, but the m term does *not* result in dispersive edge state bands in the gap. Thus the m term, by itself causes graphene to become a gapped semiconductor. With both the ISO coupling Δ and onsite sublattice potential difference m terms present, the different valleys and different spins have the different mass gaps $|m + s\tau\Delta|$.

Recent estimates, motivated by the ideas of Kane and Mele,[106] suggest that ISO coupling in graphene is extremely weak.[110, 103] For that reason we also consider Rashba spin-orbit coupling, adding terms to the tight-binding model which

are symmetry allowed whenever inversion symmetry in the graphene plane is broken (e.g. by an external electric field generated by the gate-doping routinely employed in the study of graphene systems).

$$\mathcal{H}_R = i\,\frac{2\Lambda}{3}\sum_{\langle ij\rangle\alpha} c^{\dagger}_{i\alpha}\hat{z}\cdot\left(\vec{s}\times\vec{d}_{ij}\right)c_{j\bar{\alpha}}, \tag{4.5}$$

where Λ is the Rashba spin-orbit coupling strength, $\vec{s}$ is the Pauli spin matrix vector and $\vec{d}_{ij}$ is the unit vector that points from the j-site to the i-site.[111] At low energy and to lowest order in Λ the Rasbha Hamiltonian becomes[106]

$$\hat{H}_R = \Lambda(\sigma_x\tau_z s_y - \sigma_y s_x). \tag{4.6}$$

When both Rashba and ISO couplings are included while $m = 0$, the continuum limit bulk spectrum is

$$\epsilon^b_{\pm} = \pm\Lambda + b\sqrt{(vk)^2 + (\Delta \mp \Lambda)^2} \tag{4.7}$$

where $b = \pm 1$ labels the particle/hole bands. By itself, RSO lifts spin degeneracy and when included with ISO it also breaks particle-hole symmetry. When $m = 0$, the gap disappears for $\Lambda \geq \Delta$.

We see that adding the ISO coupling Δ, the RSO coupling Λ, and the sublattice onsite potential m can gap, split and shift the bulk spectrum, yet the low energy theory is still well described by the Dirac model. Now we are ready to investigate the edge states. The full analytic form involving Δ, m and Λ is not tractable. So in Sec. 4.3 we will first consider the case of have no Rasbha coupling, $\Lambda = 0$, while later in Sec. 4.4 we will include Rashba again, while there neglecting the onsite potential, $m = 0$.

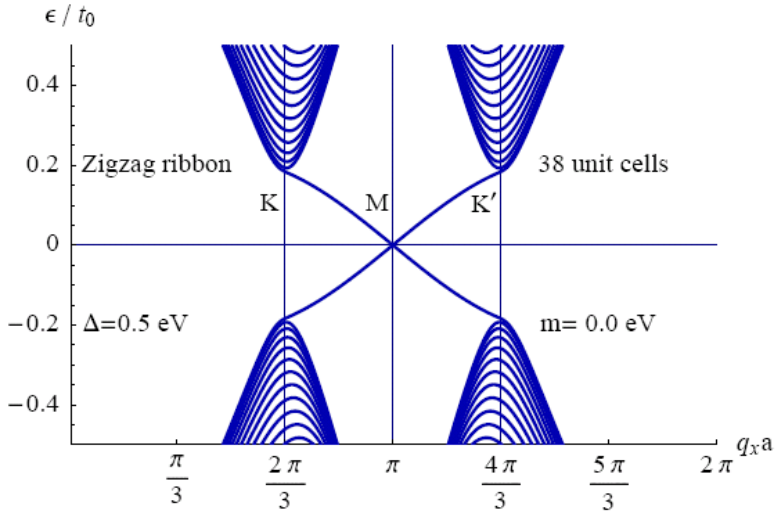

Figure 4.2: The low energy zigzag edge spectrum with $\Delta = 0.5$ eV and $m = 0$ for a 38 unit cell wide ribbon. The edge projections of the K, M and K' points are indicated by the vertical gridlines. Note that for zigzag edges and ribbons the K and K' valleys are distinct, because the x-components of these wavevectors are distinct [see Fig. 4.1]. Edge states exist only within the gap and at low energy their momenta are far from the Dirac points so most edge states cannot be described by the Dirac model.

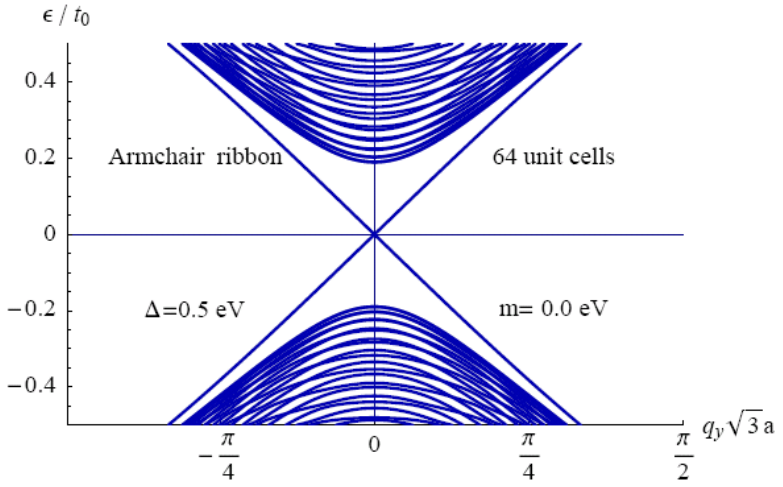

Figure 4.3: The low energy armchair spectrum with $\Delta = 0.5$ eV and $m = 0$ for a 64 unit cell wide ribbon. For armchair edges and ribbons the inequivalent K and K' points are taken instead along the q_x axis [see Fig. 4.1] and they project to identical edge wavevectors at $q_y = 0$. Here both project to the gridline which goes through the origin. Notice how the edge state spectrum continues outside of the gap. Edge states close to $q_y = 0$ including those in the middle of the gap can be described by the Dirac model if Δ is not too large.

4.3 Graphene Ribbon Edge State Properties

4.3.1 Numerical tight-binding model of graphene ribbons

We begin by implementing the NN TBM, Eqn. (4.1), to our two ribbon geometries [see Fig. 4.1] for the case of no RSO, $\Lambda = 0$. This will allow us to showcase the different solution methods before going on to the more difficult Rashba problem. In Figs. 4.2 and 4.3 we show the spectra of the TBM, Eqn. (4.1) plotted as a function of the wavevector along the sample edge for zigzag and armchair edged ribbons respectively. These calulations are for $\Delta = .5$ eV and $m = 0$. Both spectra show clear edge state branches, but the character of the localized states and their dispersion along the edge is quite different in the two cases. These spectra were obtained by solving the TBM numerically for a graphene ribbon that is infinitely extended along parallel edges.

Kane and Mele observed that edge state bands appear when ISO is added to the TBM of a zigzag ribbon.[106] This is reproduced here in Fig. 4.2. Fig. 4.2 also shows that most zigzag edge states exist at wavevectors that are far from the projected K points, even when spin-orbit interactions are weak. It follows that their physics can never be completely captured by the Dirac equation (4.3). Since the zigzag edge state bands extent far from the Dirac point at low energy, it is necessary to consider the discrete microscopic TBM in order to achieve some understanding of them. In Sec. 4.3.4, we will discuss how edge solutions can be obtained using the TBM directly, quite simply in the case of semi-infinite ribbons, without appealing to the Dirac equation limit.

In Fig. 4.3 we see that all low energy armchair edge states occur in the Dirac valleys so that analytical solutions are directly found within the Dirac model Hamiltonian, Eqn. (4.9), supplemented by appropriate boundary conditions on the eigenvectors. As we will show first, in Sec. 4.3.3, the armchair edge bands can be described well by the Dirac model of semi-infinite ribbons because at low energy the

edge state band is always near the Dirac points. Next, we must discuss some details of the boundary conditions before we can continue on to these solutions.

4.3.2 Continuum model boundary conditions

We will consider the necessary boundary conditions (BCs) to find a semi-infinite armchair edge state solution with its edge at $x = 0$, which is well described by the continuum Dirac model, Eqn. 4.3. As it turns out, to describe the unnormalized solution of the two 4-spinors ψ^K and $\psi^{K'}$ of an armchair graphene ribbon edge state requires 16 real constraints. Since the valleys are decoupled in respect to the Hamiltonian, the eigenvalue equation supplies four equations that relate the pseudospin components.

The physical low energy electronic wavefunction in the Dirac description is

$$\Psi_{\text{phys}}(\mathbf{r}) = \psi^K(\mathbf{r})\, \mathrm{e}^{i\,\mathbf{K}\cdot\mathbf{r}} + \psi^{K'}(\mathbf{r})\, \mathrm{e}^{i\,\mathbf{K}'\cdot\mathbf{r}}. \tag{4.8}$$

Thus the requirement that $\Psi_{\text{phys}}(x = 0) = 0$ gives generally for armchair low energy states:

$$\psi^K_{\alpha,s}(x = 0) = -\psi^{K'}_{\alpha,s}(x = 0), \tag{4.9}$$

which gives four more equations that relate the wavefunctions in each valley.

4.3.3 Armchair edge states - Continuum Dirac theory, semi-infinite system ($\Lambda = 0$)

In this section we solve the linearized graphene Hamiltonian in Eqn. (4.3) for an armchair semi-infinite sheet. We seek edge states by making the *ansatz* that the wavefunction depends on the $\hat{x}$ coordinate only through a decaying exponent $\mathrm{e}^{-\lambda x}$, where λ is the inverse localization length, which should be positive definite as required by normalization on a half-infinite plane. This amounts to taking $k_x \to i\,\lambda$

in Eqn. (4.3). The resulting relationship between the localization length, the edge momentum and the energy is:

$$(v\lambda_s)^2 = (s\,\Delta + m)^2 + (vk_y)^2 - \epsilon^2, \tag{4.10}$$

$$(v\lambda'_s)^2 = (s\,\Delta - m)^2 + (vk_y)^2 - \epsilon^2, \tag{4.11}$$

(As we discuss later in Sec. 4.3.4, it is possible to find continuum model zig-zag edge solutions over a limited regime of edge wavevectors near the Dirac points. We will there contrast some of the armchair edge considerations which are the main focus of this section with corresponding zigzag edge considerations.) As can be seen from the above equations, when $m \neq 0$ the localization lengths near distinct Dirac points differ.

Let us make an *ansatz* of the K and K' components of the unnormalized wavefunction that satisfies the amplitude boundary conditions, Eqn. (4.9):

$$\psi_s^K(\mathbf{r}) = +\mathrm{e}^{i\,\varphi_s}\mathrm{e}^{r\,i\,k_y y}\mathrm{e}^{-\lambda x}\begin{pmatrix} 1 & \text{- A site} \\ i\,\zeta_s & \text{- B site} \end{pmatrix}, \tag{4.12}$$

$$\psi_s^{K'}(\mathbf{r}) = -\mathrm{e}^{i\,\varphi_s}\mathrm{e}^{r\,i\,k_y y}\mathrm{e}^{-\lambda' x}\begin{pmatrix} 1 \\ i\,\zeta_s \end{pmatrix}, \tag{4.13}$$

where ζ_s is determined from the eigenvalue problem[151] and $r = \pm$ denotes right(left)-movers and φ_s is an undetermined phase. For the edge states there is also the condition that the current normal to the edge vanishes at the edge for each valley and spin. This condition is not necessary, but it does ensure that ζ_s is a real constant. Solving the eigenvalue problem with the Dirac Hamiltonian, Eqn. (4.3), gives the

eight real equations:

$$v(r\,k_y - \lambda\,)\zeta_s = \epsilon - s\Delta - m, \tag{4.14}$$

$$v(r\,k_y + \lambda')\zeta_s = \epsilon + s\Delta - m, \tag{4.15}$$

$$(\epsilon + s\Delta + m)\zeta_s = v(r\,k_y + \lambda\,), \tag{4.16}$$

$$(\epsilon - s\Delta + m)\zeta_s = v(r\,k_y - \lambda'). \tag{4.17}$$

Using Eqns. (4.17) implies that the edge dispersion is simply linear:

$$\epsilon = r\,vk_y, \qquad \zeta_s = r. \tag{4.18}$$

Notice from Eqns. (4.10) and (4.11) that the mathematical requirement for the existence of edge states is that $(s\,\Delta - m)^2 > \epsilon^2 - (vk_y)^2$, which is automatically satisfied here by a linear dispersion. Next, knowing a linear dispersion, it also follows from Eqns. (4.10) and (4.11) that the inverse localization lengths are

$$v\lambda = r(s\,\Delta + m), \quad v\lambda' = r(s\,\Delta - m). \tag{4.19}$$

Here we explicitly see "spin-filtered" edge states where the requirement for positive λ implies different spins for right movers and left movers on the $x = 0$ edge. The relationship between this finding and the counter-propagating spin states along opposite edges (of finite-sized ribbons) was discussed by Kane and Mele in connection with the spin-Hall effect.[106] For the case of $m = 0$ the above result for armchair ribbons has been presented by us[152] and by others.[154] Note that that when $m < \Delta$ the edge state band's dispersion is the same as the lowest energy bulk band's dispersion in the massless case ($\Delta = m = 0$)[see Fig. 4.3]; Based on this result we posit that

the correct dispersion of the NN TBM edge states is

$$\epsilon(k_y) = r\frac{4}{\sqrt{3}\,a}\sin\left(\frac{\sqrt{3}\,k_y a}{4}\right). \tag{4.20}$$

Indeed we do find that this form *exactly* fits the numerics as it goes farther from a Dirac point and as long as $m < \Delta$.

Also, $\Delta = m$ is a special point where the total wavefunction becomes delocalized, since either λ or λ' vanishes. Numerics verify that the bulk band's gap closes when $\Delta = m$. For finite width ribbons when $\Delta = m$ numerics also show a gap $\sim \pi/W$, which is due to finite size effects. When $\Delta < m$ it is difficult for edge states to exist since λ and λ' have opposite signs, yet the BC, Eqn. (4.9), still needs to be satisfied. This also explains the abscence of edge state bands when $\Delta = 0$ for armchair ribbons.

4.3.4 Zigzag edge states - Discrete TBM, semi-infinite system ($\Lambda = 0$)

As can be seen in Fig. 4.5, in the case of zigzag edge geometry, the low energy edge states are far from the (bulk) nodal points. It is therefore not useful to solve the linearized Dirac model in this case. It is however, possible to find the edge states in a semi-infinite TBM. Edge states have been long known for zigzag ribbons.[127, 128, 106] It is useful to introduce a discrete $\hat{y}$-coordinate label J (this integer labels the zigzag rows in Fig. 4.1).[136, 153] The two rows of zero amplitude sites along $y = 0$ and $y = -a/(2\sqrt{3})$ are collectively labeled by $J = 0$. Next, the first two physical rows of atoms are labeled $J = 1$ and so forth, i.e., the discrete coordinate labels the two alternating sublattice rows that form a zigzag pattern. Since the Hamiltonian

is diagonal in the physical spin, we may write the discrete spin up wavefunction as

$$\psi(x,J) = \mathrm{e}^{i\,p_x x}\phi(J) = \mathrm{e}^{i\,p_x x}\sum_n (z_n)^J \begin{pmatrix} \phi_{A,n}(0) \\ \phi_{B,n}(0) \end{pmatrix}, \tag{4.21}$$

for momentum p_x (measured from π) and (as we will see) $n = 1, 2$ solutions of z_n, where $|z_n| < 1$ ensures normalizability. The *discrete* BC requires that $\phi(J{=}0){=}0$. Let the ISO gap be $\Delta = 3\sqrt{3}\delta$ and from the TBM, Eqn. (4.1), the discrete Schrödinger equation then reads for a spin up right mover

$$\begin{aligned} \epsilon\phi_A(J) &= -\phi_B(J-1) - Q\,\phi_B(J) - m\,\phi_A(J) - \\ &\quad -\delta(V\phi_A(J-1) + V\phi_A(J+1) - R\,\phi_A(J)), \\ \epsilon\phi_B(J) &= -\phi_A(J+1) - Q\,\phi_A(J) + m\,\phi_B(J) \\ &\quad +\delta(V\phi_B(J+1) + V\phi_B(J-1) - R\,\phi_B(J)), \end{aligned} \tag{4.22}$$

for each $J > 0$, where here we take $t_0 \to 1$ and define $Q = 2\cos(p_x a/2)$, $V = 2\sin(p_x a/2)$ and $R = 2\sin(p_x a)$. Substituting the wavefunction, Eqn. (4.21), into Eqn. (4.22) yields

$$\begin{aligned} (1/z + Q)\phi_B(0) + (\epsilon + m + \delta(2Vc - R))\phi_A(0) = 0, \\ (\epsilon - m - \delta(2Vc - R))\phi_B(0) + (z + Q)\phi_A(0) = 0, \end{aligned} \tag{4.23}$$

where we denote $c = (z + 1/z)/2$. By Cramer's rule, this matrix equation has a non-trivial solution for each n only when

$$\begin{vmatrix} 1/z + Q & (\epsilon + m + \delta(2Vc - R)) \\ (\epsilon - m - \delta(2Vc - R)) & z + Q \end{vmatrix} = 0, \tag{4.24}$$

which leads to the relation between the energy ϵ and the eigenvalues z

$$\epsilon^2 - [m + \delta(2Vc - R)]^2 = Q^2 + 1 + 2Q\,c. \tag{4.25}$$

Up to this point no approximations have been made. Physically, however, we are interested in energies close to half filling with weak ISO coupling $\delta, m \ll 1$. Keeping up to second order in δ and m in the solutions to Eqn. (4.25) we find two solutions which are physical and localized near $J = 0$ (i.e. for $|z| < 1$):

$$\begin{aligned} z_1 &\approx -Q + \tfrac{\epsilon^2 Q^2 - (\delta(V + Q(R + QV)) - Qm)^2}{Q(Q^2-1)}, \\ z_2 &\approx -\delta^2 V^2/Q; \end{aligned} \tag{4.26}$$

with (unnormalized) eigenvectors

$$\begin{aligned} u_1 &= \begin{pmatrix} \epsilon - m + \delta(V\frac{1+Q^2}{Q} + R) \\ -z_1 - Q \end{pmatrix}, \\ u_2 &= \begin{pmatrix} -Q/V \\ \delta Q \end{pmatrix}. \end{aligned} \tag{4.27}$$

Generally, the localized edge state has the form

$$\phi(J) = C_1\,(z_1)^J\,u_1 + C_2\,(z_2)^J\,u_2 \tag{4.28}$$

with some coefficients C_1 and C_2 that should be fixed by the BC and normalization. Since the BC requires that $\phi(J = 0) = 0$, we can apply Cramer's rule to the eigenvectors:

$$\begin{vmatrix} \epsilon - m + \delta(V\frac{1+Q^2}{Q} + R) & -Q/(V) \\ -z_1 - Q & \delta Q \end{vmatrix} = 0 \tag{4.29}$$

which leads to the conditions on ϵ for spin up right movers

$$\epsilon = -m + 3\delta R = -m + \frac{2\Delta}{\sqrt{3}} \sin(p_x a), \tag{4.30}$$

while the spin down left movers have the same expression except with $-m \to +m$ and $+\Delta \to -\Delta$. Our numerics [see Figs. 4.4 and 4.5] confirm this expression for the edge state dispersion in the ISO-gap. As the gap closes, the edge states are pushed to higher energy and become degenerate with bulk states at different momenta [see Fig. 4.5].

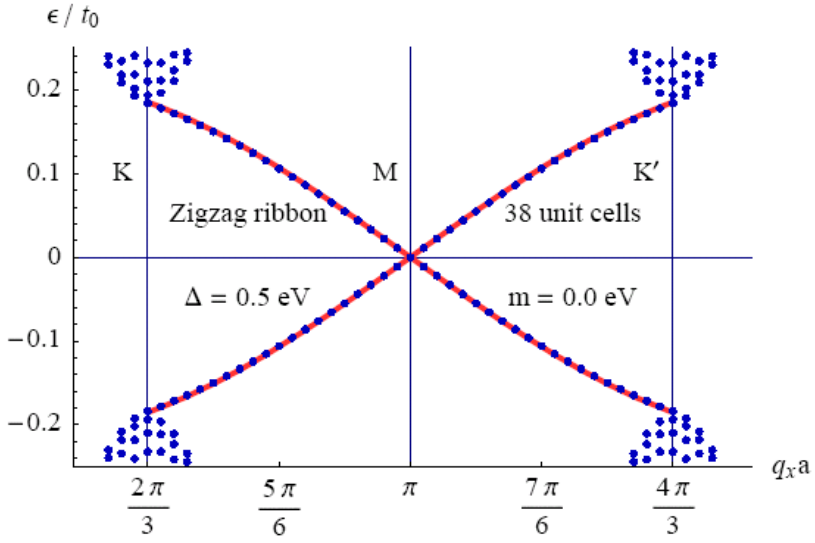

Figure 4.4: The zigzag spectrum with $\Delta = 0.5$ eV and $m = 0$. The (blue) dots are the numeric solution to the TBM (the same data was shown in Fig. 4.2) and the dispersion, Eqn. (4.30), is shown by the (red) solid line.

We plot the inverse localization length in Fig. 4.7 for several values of Δ in the non-Dirac region. Note how Δ divides the peak near $q_x a = \pi$, where the states are maximally localized. We can also find the localization length near the K points. The total momentum there is $\mathbf{q} = \mathbf{K} + \mathbf{k}$. Following the same method as for the armchair case, we find the same expressions for the inverse localization length as

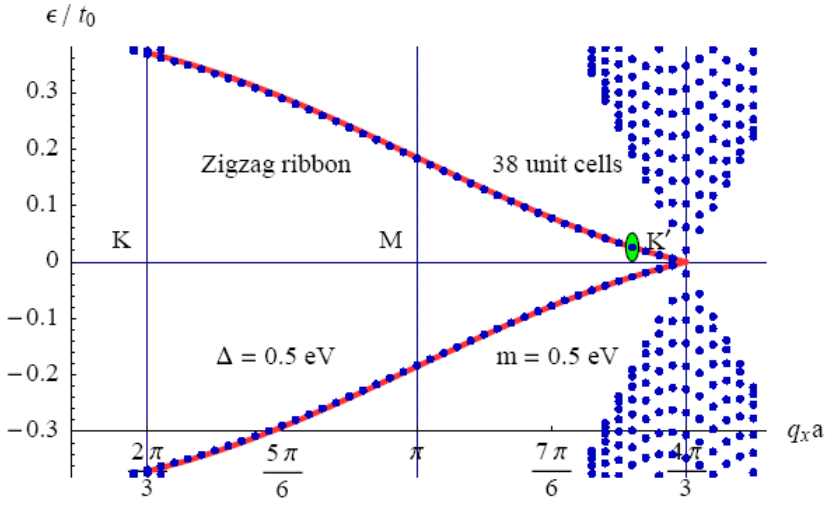

Figure 4.5: The zigzag spectrum with $\Delta = 0.5$ eV and $m = 0.5$ eV for up spins. The TBM solution is shown by the (blue) dots and Eqn. (4.30) is shown by the (red) line.

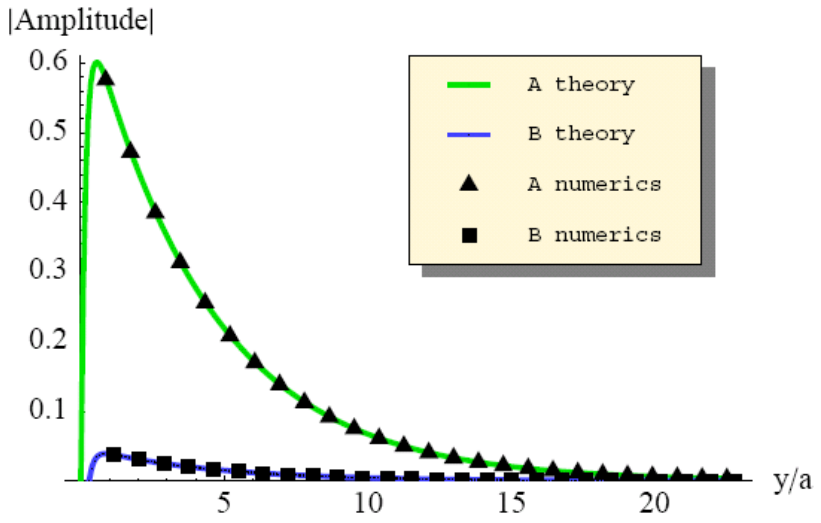

Figure 4.6: The zigzag wavefunction amplitude with $\Delta = m = 0.5$ eV for a spin up left mover at $q_x a = K'_x a - \pi/15$ [the green circle in Fig. 4.5]. Theory (solid lines) refers the spin up part of the wavefunction described by Eqn. 4.28 and the numerics (points) refers to the TBM in Eqn. 4.1. Note that z_1 is the dominating term for the theoretical solution and that the vanishing boundary condition is met.

Eqns. (4.10) and (4.11). Using the fact that $\epsilon = b|s\tau\Delta + m|$, with $b = \pm 1$ for the conduction(valence) band and $\tau = \pm 1$ for the $K(K')$ point, we find that the inverse localization length is $(v\lambda)^2 = (v\lambda')^2 = (vk_y)^2$. Therefore, the zigzag edge states are delocalized at the Dirac points. So unlike armchair ribbons, the localization length for zigzag ribbons is sensitive to small changes in momentum.

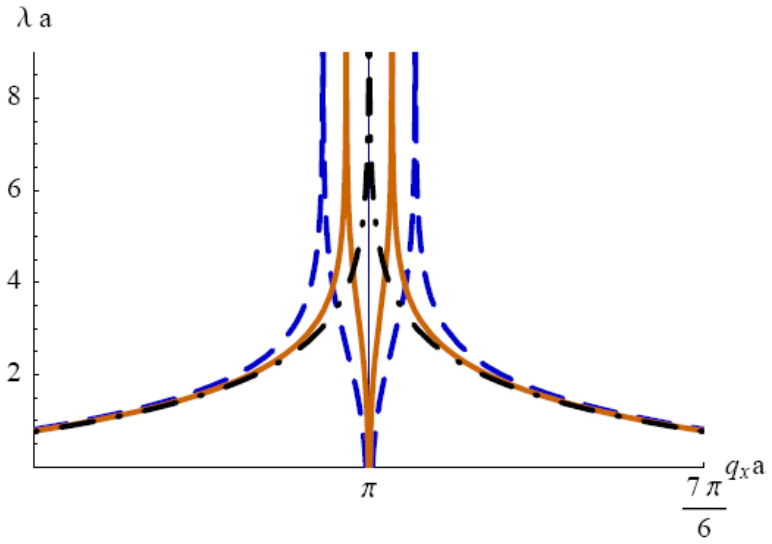

Figure 4.7: The inverse localization length versus momentum as derived from the dominant term z_1 in Eqn. (4.26), for $\Delta = 0$ (black dot-dashed line), $\Delta = 0.25$ eV (orange solid line), and $\Delta = 0.5$ eV (blue dashed line). An onsite term $m < \Delta$ does not significantly change these profiles. The peaks are observed to be $\pm 0.7(\Delta/\text{eV})$ away from π (the M point).

4.4 Edge States for systems with Rashba Spin-Orbit Coupling

4.4.1 Armchair edge states - Continuum Dirac theory, semi-infinite system ($m = 0$)

In the semi-infinite treatment, the four unnormalized, edge state eigenvectors of the Dirac-Rashba Hamiltonian, the sum of Eqns. (4.3) and (4.6) with $m = 0$ are

$$\psi_{\pm}^{K}(\mathbf{r}) = \quad \mathrm{e}^{-\lambda_{\pm} x}\mathrm{e}^{i\,k_y y}\begin{pmatrix} v(k_y - \lambda_{\pm}) \\ \mp(\epsilon - \Delta) \\ +i(\epsilon - \Delta) \\ \mp iv(k_y + \lambda_{\pm}) \end{pmatrix} \begin{matrix} \text{- A } \uparrow \\ \text{- A } \downarrow \\ \text{- B } \uparrow \\ \text{- B } \downarrow \end{matrix}, \tag{4.31}$$

$$\psi_{\pm}^{K'}(\mathbf{r}) = -\mathrm{e}^{-\lambda_{\pm} x}\mathrm{e}^{i\,k_y y}\begin{pmatrix} (\epsilon - \Delta) \\ \pm v(k_y + \lambda_{\pm}) \\ iv(k_y - \lambda_{\pm}) \\ \pm i(\epsilon - \Delta) \end{pmatrix}, \tag{4.32}$$

where there are two possible inverse localization lengths

$$(v\lambda_{\pm})^2 = (vk_y)^2 - (\epsilon - \Delta)(\epsilon + \Delta \mp 2\Lambda). \tag{4.33}$$

Here, since the spin is no longer a good quantum number, we must keep all four components of the wavefunction. The vanishing amplitude BC, Eqn. (4.9), is imposed by applying Cramer's rule to a 4×4 matrix with the four eigenfunctions in Eqns. (4.31) and (4.32) forming its the columns. The determinant polynomial yields five roots for the energy, but only two are physical and non-trivial solutions with

positive real definite $\lambda_{\pm}$'s. These two edge state bands have the dispersion

$$\epsilon_r = \frac{1}{2}(r\,vk_y + \Delta) + \frac{(vk_y)^2 + \Lambda^2 - \sqrt{(\Delta^2 - \Lambda^2)^2 + (2vk_y\Lambda)^2}}{2(r\,vk_y + \Delta)}, \tag{4.34}$$

where again $r = \pm 1$ for right(left)-movers. At the limit $\Lambda \to 0$, Eqn. (4.34) reduces to $\epsilon_r = r\,vk_y$, which is our previous result. Note that $\epsilon_r(k_y = 0) = \Lambda^2/\Delta$, which illustrates how the particle-hole symmetry is broken. We plot the inverse localization length in Fig. 4.8 for several values of Λ. This illustrates how Rasbha lenghtens and shortens the localization lengths in armchair edges.

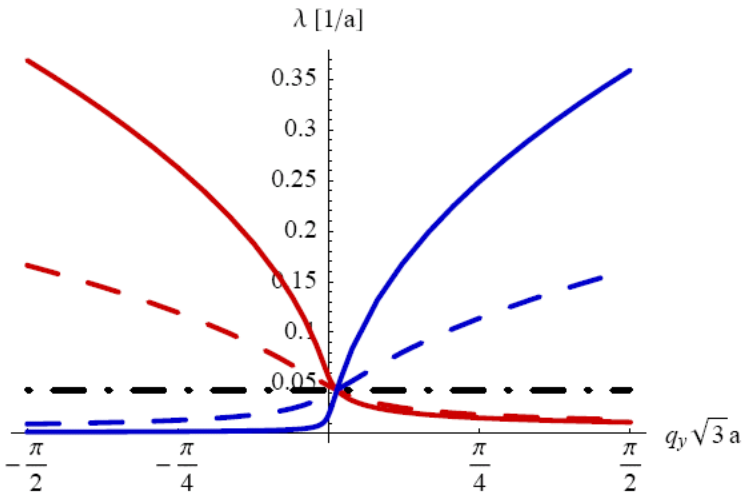

Figure 4.8: The armchair edge inverse localization length versus momentum as derived from Eqns. (4.33) and (4.34) where $\lambda_{\pm}$ is plotted by a red(blue) line. All curves are for $\Delta = 0.1$ eV and individually $\Lambda = 0$ (black dot-dashed line), $\Lambda = 0.01$ eV (dashed lines), and $\Lambda = 0.05$ eV (solid line).

4.4.2 Armchair edge states - Continuum Dirac theory, finite ribbons ($m = 0$)

For further insight, consider a finite size treatment of armchair nanoribbons with ISO and RSO; where it is now more convenient to set $x = 0$ to be along the *center* of the ribbon. By the symmetry of $\hat{H} = \hat{H}_D + \hat{H}_R$ the eigenvalue equation gives the form of the four possible total wavefunctions:

$$\psi_K(\mathbf{r}) = \begin{pmatrix} +f(+x) \\ \pm\, g(-x) \\ -i\, g(+x) \\ \mp\, i\, f(-x) \end{pmatrix} \mathrm{e}^{i\, k_y y}, \tag{4.35}$$

$$\psi_{K'}(\mathbf{r}) = -r \begin{pmatrix} -\, g(+x) \\ \mp\, f(-x) \\ +i\, f(+x) \\ \pm\, i\, g(-x) \end{pmatrix} \mathrm{e}^{i\, k_y y}, \tag{4.36}$$

where $g(x)$ and $f(x)$ are real functions. For armchair nanoribbons we have that $W = (N+1)(a/2)$, where N is the number of columns of atoms across the ribbon, and for metallic ribbons $N+1$ is a multiple of 3. Recall that semiconducting ribbons have a small gap in the bulk. Numerics show that the ISO coupling Δ does shrink the gap δ_a, but notably it is never closed for semiconducting ribbons. So even the edges states in the semiconducting armchair ribbons have a gap. For metallic armchair nanoribbons the vanishing amplitude BC on the ribbon edges imposes that

$$\begin{aligned} f_{\mathrm{even}}\,(W/2) &= -r\, g_{\mathrm{even}}\,(W/2)\,, \\ f_{\mathrm{odd}}\,(W/2) &= -r\, g_{\mathrm{odd}}\,(W/2)\,, \end{aligned} \tag{4.37}$$

where $r = \pm 1$ is for right(left) movers.

From the eigenvalue equation we find the relations

$$(\epsilon - \Delta) f(x) = -v(\partial_x + k_y) g(x) \tag{4.38}$$

$$(\epsilon^2 - \Delta^2 - (vk_y)^2) g(x) \mp 2\Lambda g(-x) = -v^2 \partial_x^2 g(x) \tag{4.39}$$

This unusual result means that the DE's for the even and odd parts of $g(x)$ are distinct, and this distinction is controlled by the Rashba coupling Λ. We now can take the solution for $g(x)$ as

$$g(x) = (\epsilon - \Delta) \left[A \cos(k_\pm x) - B \sin(k_\mp x) \right], \tag{4.40}$$

where the two solutions for k_x are

$$(vk_\pm)^2 = (\epsilon - \Delta)(\epsilon + \Delta \mp 2\Lambda) - (vk_y)^2, \tag{4.41}$$

which is similar to Eqn. (4.33). Observe that if $\Lambda = 0$ or $\epsilon = \Delta$ then $k_+ = k_-$.

Next we will determine the criteria for the existence of edge states. They exist when *both* k_+ and k_- are pure imaginary. Note that when $\Lambda \neq 0$ then the lowest particle band can have one $k_\pm$ real and the other pure imaginary, these are summarized in Table 4.2. We see that at low enough energy, near $\epsilon(k_y = 0)$, there are always edge states when $\Lambda < \Delta/2$. Unlike the case with no Rashba, for large enough k_y the edge states vanish.

	$\Delta < \epsilon$	$\epsilon, \Lambda \leq \Delta$
k_+	$2\Lambda(\epsilon - \Delta) > \epsilon^2 - (vk_y)^2 - \Delta^2$	always
k_-	never	$\Lambda < (\epsilon + \Delta)/2$

Table 4.2: The conditions for k_+ or k_- to be pure imaginary when $\Lambda \neq 0$.

Continuing, from Eqns. (4.38) and (4.40) as well as the BCs in Eqn. (4.37)

we find the conditions on the coefficients

$$-\rho_s v k_\pm \, A = [v k_y - r(\epsilon - \Delta)] \, B, \tag{4.42}$$

$$v k_\mp \, B = \rho_c \, [v k_y - r(\epsilon - \Delta)] \, A, \tag{4.43}$$

where $\rho_c = \cos(k_\pm W/2)/\cos(k_\mp W/2)$ and $\rho_s = \sin(k_\pm W/2)/\sin(k_\mp W/2)$. Finally, combining Eqns. (4.42) and (4.43) gives the trancendental equation:

$$[v k_y - r(\epsilon - \Delta)]^2 = -v^2 k_\pm k_\mp \rho_t, \tag{4.44}$$

where $\rho_t = \tan(k_+ W)/\tan(k_- W)$. When $k_\pm W \ll 1$, or equivalently Δ, $\Lambda < t_0/N$, then for the energy bands that cross $\epsilon = 0$ we may approximate

$$v^2 k_\pm k_\mp \rho_t \approx (v k_\pm)^2.$$

Thus, the dispersion for the lowest energy bands approximates to $\epsilon \cong \pm\Lambda + r v k_y$. It is interesting to note that the RSO polarization opposes the localization and polarization due to the ISO edge states. So when both ISO and RSO are present a given spin component is somewhat localized to *both* edges in finite-sized ribbons. As we introduce and increase the Rasbha coupling on a pure ISO edge state, the RSO delocalizes the state across the ribbon and increases the polarization along the opposite edge as well (see Fig. 4.10). These effects mean that the spin current can no longer be dissipationless where these finite size effects matter.

We have shown that we can find the chiral edge state solutions in the gap for semi-infinite armchair edges and finite sized armchair ribbons without RSO, $\Lambda = 0$, and with RSO, $\Lambda \neq 0$. This can be done by simply using the effective low energy theory of the system, a two dimensional Dirac-like Hamiltonian. This is because these edge state bands are centered on the Dirac points at low energy.

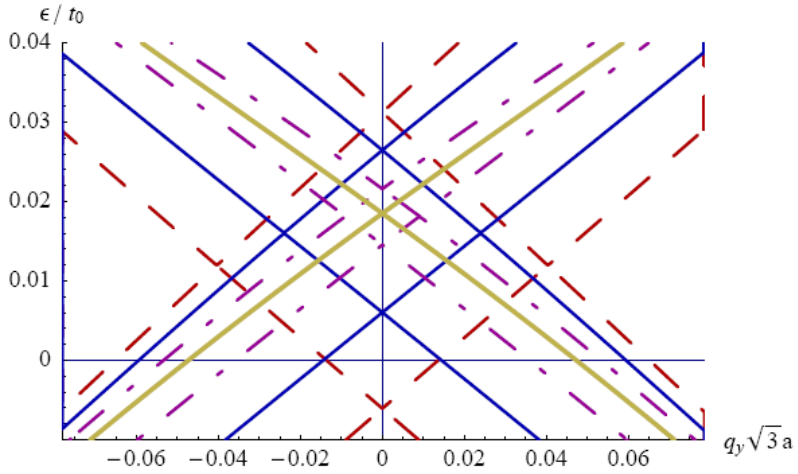

Figure 4.9: The armchair spectrum for $\Delta = 0.2$ eV and $\Lambda = 0.1$ eV ($k_{\pm}W < 1$ is not satisfied here, so there is an upward shift). The three split curves are from the TBM numerics: 25 unit cells - (red dashed line), 40 unit cells - (blue solid line) and 67 unit cells (purple dotted-dashed line). The analytic curve from the semi-infinite result, Eqn. (4.34), is a (gold) thick solid line. This also illustrates how the particle-hole symmetry is broken.

4.5 Existence of edges states – topological considerations

The Chern number is a bulk topological number.[155] There is a theorem that relates the bulk topological Chern number to the edge topological winding number.[156] If to a system known to have edge states we add another interaction, as long as the Chern number remains conserved then this theorem assures us that the edge states still exist. However, one cannot calculate the Chern number when a non-zero Rashba coupling is included.

Some detailed topological studies of the $\mathcal{H}_{\mathcal{D}} + \mathcal{H}_{\mathcal{R}}$ Hamiltonian have been recently done which introduce another topological number instead of the Chern number.[157] When in a material spin-orbit generates a gap for the bulk spectrum, yet allows the edge states to exist in the gap, this material is called a topological

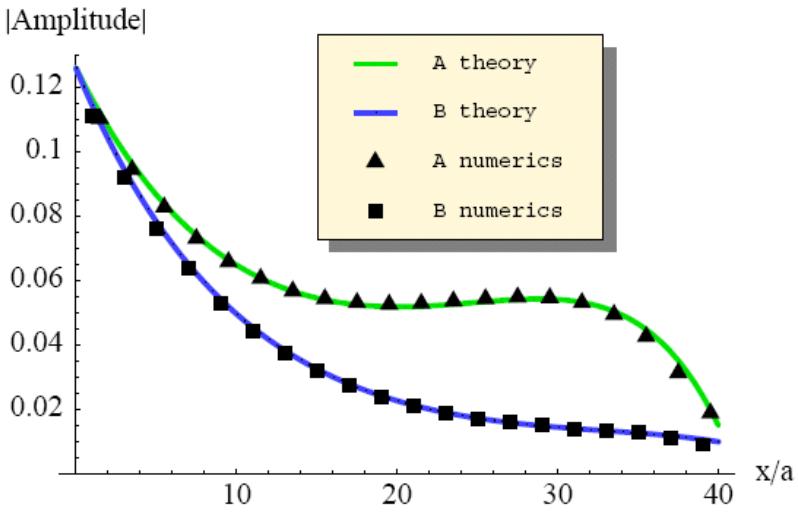

Figure 4.10: An illustration of a state with $\Delta = 0.2$ eV and $\Lambda = 0.1$ eV at $q_y(\sqrt{3}a) = \pi/15$ for the up spin K valley component of the wavefunction; for an armchair ribbon width of 40 unit cells. Theory (solid lines) refers the spin up part of the wavefunction described in subsection 4.4.2 and the numerics (points) refers to the TBM in Eqn. 4.5. Recall that contributions from both valleys are required to satisfy the vanishing boundary condition, Eqn. 4.9, at the edges.

insulator.[158] Graphene is a topological insulator when $|2\Delta - m| > \sqrt{m^2 + 4\Lambda^2}$.[157] The establishment of a more general edge-bulk correspondence is still an open problem here.

We can calculate the Chern number if we introduce a small Zeeman spitting. The Chern number is defined by the intergration of the Berry curvature $\Omega_z(\mathbf{q})$ over the first Brillouin zone (FBZ). The Berry curvature[159] in the $\hat{z}$-direction is defined as

$$\Omega_z(\mathbf{q}) \equiv i \left[\left\langle \frac{\partial\psi(\mathbf{q})}{\partial q_x} \middle| \frac{\partial\psi(\mathbf{q})}{\partial q_y} \right\rangle - \left\langle \frac{\partial\psi(\mathbf{q})}{\partial q_y} \middle| \frac{\partial\psi(\mathbf{q})}{\partial q_x} \right\rangle \right].$$

We determine the proper values for the Berry curvature from the TBM. Notably, contributions can *also* be found near the Γ and M points, as well as the K points [see Figs. 4.11, 4.12 and 4.13]. With only ISO, there is a finite Lorentzian peak about the K-point, that is well described by the Dirac theory.[106] However, when including RSO, we see that the Berry curvature is distributed in singular peaks among all three crystallographic points. So a purely Dirac treatment of Berry curvature in graphene with ISO and Rashba fails to fully characterize the Berry Curvature.

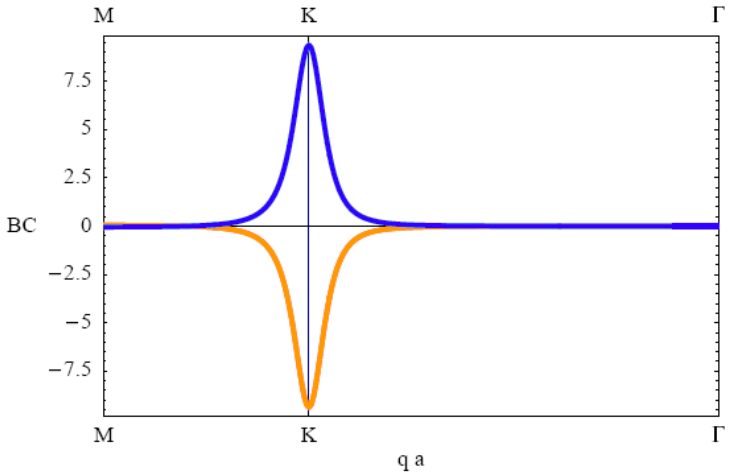

Figure 4.11: The Berry curvature profile for graphene valence band (or π band in orange) and conduction band (or π^* band in blue) for $\Delta = 0.2t_0$ and a Zeeman splitting of $0.001t_0$.

We calculated the Chern number numerically, see Tabs. 4.3-4.5. In the FBZ, there is one K, K' and Γ point and three M points. The weighted contribution approximately gives the total Chern number for each band (labelled 1-4), as seen in Tab. 4.3. Comparing the case without Rashba, Tab. 4.3, with the cases with Rashba, Tabs. 4.4 and 4.5, implies that including Rashba generates a $+\frac{1}{2}$ phase shift to the Berry curvature of the "spin-down-like" bands E_1 and E_3 and a $-\frac{1}{2}$ phase shift to the Berry curvature of the "spin-up-like" bands E_2 and E_4, yet the overall sign of the Chern number remains the same. Changing the sign of the Zeeman splitting univerally changes the sign of the Chern number contributions, due to a relabeling of the bands. In the presence of the Rashba coupling, the Chern number contributions at the K points do not give the full Chern number by standard calculations, namely, the low energy Dirac model fails to give the complete value of the Chern number of each band unless one invent the proper regularization of this anomaly.

Orbital[t_0]	$C_n(K)$	$C_n(\Gamma)$	$C_n(M)$	C_n
$E_1^K = -0.201$	-0.413	-2.8e-5	-0.038	-1
$E_2^K = -0.199$	+0.413	+2.8e-5	+0.038	+1
$E_3^K = +0.199$	+0.413	+2.8e-5	+0.038	+1
$E_4^K = +0.201$	-0.413	-2.8e-5	-0.038	-1

Table 4.3: Chern number contribution from each symmetry point when $\Delta = 0.2t_0$, $\Lambda = 0.0t_0$ and Zeeman splitting of $0.001t_0$. The radius for the Berry curvature integration is chosen as $\frac{1}{2}\overline{KM}$. The K valley contribution $C_n(K)$ here is tending toward ± 0.5; $C_n = [2C_n(K) + C_n(\Gamma) + 3C_n(M)]$.

Note that each Chern number remains the same as long as the energy gap is open, i.e. $\Delta > \Lambda$. Thus, this affirms that the edge states then also exist. What is interesting about this is that the effective Dirac model describes these edge state bands well when $\Delta > \Lambda > 0$, yet fails (as is expected) to describe the bulk Berry curvature calculations. Here we see that when $\Lambda \neq 0$ there are Berry curvature contributions at the M and Γ points as well, which can never be provided by a

Orbital[t_0]	$C_n(K)$	$C_n(\Gamma)$	$C_n(M)$	C_n
$E_1^K = -0.220$	-0.044	+0.415	-0.450	-1
$E_2^K = -0.180$	+0.044	-0.415	+0.450	+1
$E_3^K = +0.199$	+0.870	+0.415	-0.396	+1
$E_4^K = +0.201$	-0.870	-0.415	+0.396	-1

Table 4.4: Chern number contribution from each symmetry point when $\Delta = 0.2t_0$, $\Lambda = 0.01t_0$ and Zeeman splitting of $0.001t_0$. The radius for the Berry curvature integration is chosen as $\frac{1}{2}\overline{KM}$; $C_n = [2C_n(K) + C_n(\Gamma) + 3C_n(M)]$.

Orbital	$C_n(K)$	$C_n(\Gamma)$	$C_n(M)$	C_n
$E_1^K = -0.400$	-0.004	+0.491	-0.495	-1
$E_2^K = +0.000$	+0.004	-0.491	+0.495	+1
$E_3^K = +0.199$	+0.987	+0.491	-0.490	+1
$E_4^K = +0.201$	-0.987	-0.491	+0.490	-1

Table 4.5: Chern number contribution from each symmetry point when $\Delta = 0.2t_0$, $\Lambda = 0.1t_0$ and Zeeman splitting of $0.001t_0$. The radius for the Berry curvature integration is chosen as $\frac{1}{2}\overline{KM}$; $C_n = [2C_n(K) + C_n(\Gamma) + 3C_n(M)]$.

Dirac-like model. Appearently, for graphene armchair ribbons one does not need to know the details of the high-energy theory to prove the existance of the edge state bands in the gap.

The authors are grateful for useful discussions with Di Xiao, Murat Taş, Yafis Barlas and Paul B. Wiegmann.

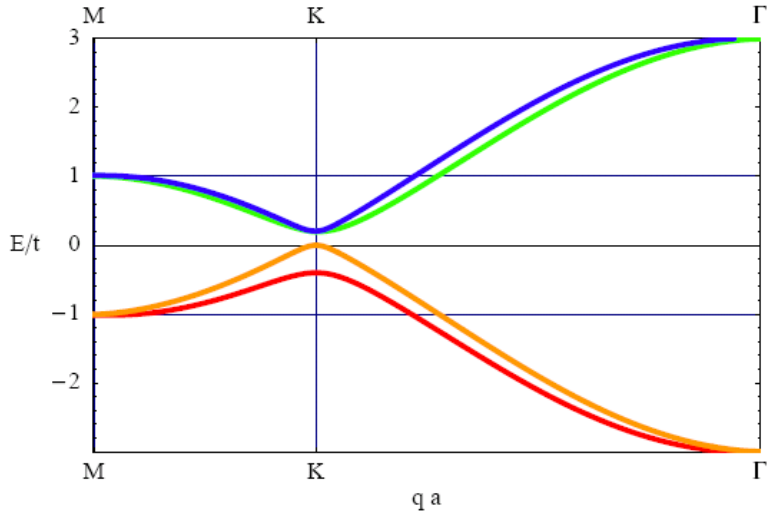

Figure 4.12: The dispersion for two-dimensional graphene with $\Delta = 0.2t_0$ and $\Lambda = 0.1t_0$. Observe how the conduction and valence bands are split and that there are still degeneracy points near the three crystallographic points.

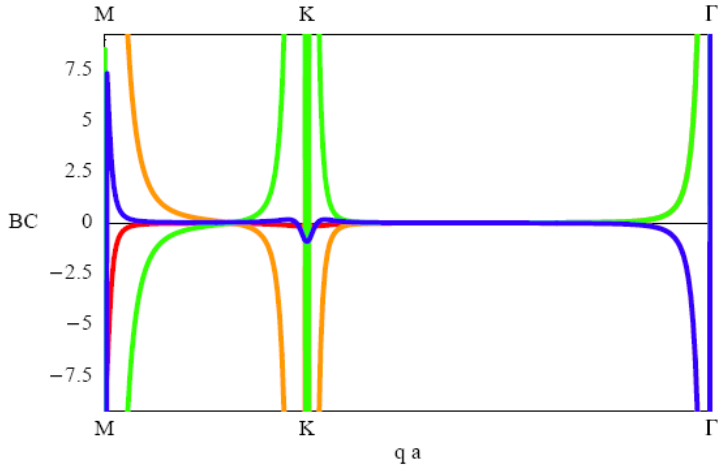

Figure 4.13: The Berry curvature profile for graphene valence bands (in red and orange) and conduction bands (in green and blue) for $\Delta = 0.2t_0$, $\Lambda = 0.1t_0$ and a Zeeman splitting of $0.001t_0$.

Chapter 5

Conclusion

The history, chemistry and introductory physics of graphitic forms has been presented. The basic theory of bulk graphene and graphene edges has been introduced. We review the peculiar edge state found in gzigzag graphene nanoribbons. We examine these zigzag flat-band edge states and then propose a route of studying the ground state of these bands by attempting to exactly diagonalize the interaction terms of the Hamiltonian with the Fourier transform of the non-interacting edge states. This method is illustrated with the Hubbard U potential, but is still being developed for the Coulomb potential. The way to carry out an efficient TBM for graphene nanoribbons, including spin-orbit coupling and an external magnetic field is laid out. We find that the full analytic solution for nanoribbons in magnetic fields is lacking, and that the edge states are affected differetly from the bulk states in a magnetic field.

We have examined edge states in graphene ribbons, especially the spin-Hall edge states of recent interest. It has been shown that the edge states in armchair and zigzag ribbons are both quantitatively and qualitatively different. At low-energy the armchair dispersion can be treated linearly by the effective continuous Dirac model, while the zigzag dispersion is demonstrably non-linear and must be described by

the more general TBM. The armchair edge states have slowly varying localization lengths, while the zigzag edge states have strongly varying localization lengths [see Figs. 4.7 and 4.8]. Also when we include an spin-independent onsite potential that differs for each sublattice, the m term, there is a topological phase transition when $\Delta = m$ for $\Lambda = 0$. This is because the gap closes there. Indeed we see that the armchair edge states disappear altogether for $\Delta < m$.

Rashba SO in graphene is found to have some novel features of its own. We have illustrated how RSO can be used to modify the spin polarization at the edges in a less dramatic yet opposing way to ISO. In finite ribbons, RSO delocalizes the pure ISO edge states, splits the bands, but does not destroy the topology of the bands (remove Chern number conservation when including a small Zeeman splitting) until $\Delta = \Lambda$. We also find the analytic solution for semi-infinite amd finite-size armchair edge states using the effective Dirac model, as long as $\Delta > \Lambda$.

Interestingly, the low energy Hamiltonian with RSO near K and K' points is sufficient to deduce the existence of edge states in the gap of the bulk spectrum and even correctly predict their dispersions and wavefunction profiles. In contrast to this good description of the edge states, the effective Dirac Hamiltonian with RSO fails to predict the topological numbers of the bands via the standard Berry curvature calculations. There are contributions that arise on the other crystallographic points, see Sec. 4.5. Therefore, armchair edge states provide an interesting example where the effective low energy theory is sufficient to prove the existence of edge states in the gap, yet not be able to calculate the bulk properties. This suggests that sometimes there exists an alternative approach in the search of topological insulators. Instead of working with the entire band, in which parameters can be not completely known, one can restrict the search only to the low energy part of the spectrum and look for the existence of chiral gapless edge states.

There are many open questions and problems about graphene edge states

that remain to be studied. How well can we theoretically describe the ground states of zigzag edges? How do carriers propagated in graphene nanoribbons in a magnetic field. What about edge states in graphene bilayers or trilayers? A study on zigzag bilayer edge states has recently been posted.[160] The ground states and magnetic questions can be repeated for these multilayers. Furthermore, it should be expected that the ISO would be much strong in graphene bilayers than monolayers, and probably quite bulk-like in trilayers. So these same methods could be applied to these potential useful multilayer systems which have tunable gaps already. Ten years ago these were all purely academic problems, but now with the discovery of graphene and the beginning of the experimention with it and the exploration its different physics these issues have been pushed to the forefront of condensed matter physics, and with the semiconducting industry beginning to invests real capital in developing device applications from graphene the future is bright for this line of research. We may soon be approaching the age of carbon.

Bibliography

[1] Andre K. Geim and K.S. Novoselov, "The rise of graphene." *Nature Materials* **6**, 3 (March 2007); figures taken from the preprint: cond-mat/0702595.

[2] Andre K. Geim, Director of the Centre for Mesoscience & Nanotechnology University at Manchester, UK. A recently interview with ESI Special Topics, see http://www.esi-topics.com/fmf/2006/november06-AndreGeim.html (November 2006).

[3] B.T. Kelly. *Physics of Graphite*, Applied Science Publishers LTD, 1981.

[4] R. Saito, G. Dresselhaus, and M.S. Dresselhaus. *Physical Properties of Carbon Nanotubes*, Imperial College Press, World Scientific, 1998.

[5] S. Thompson and J. Staley. *Orbitals and Molecular Representation*, An education module developed under a grant from FIPSE, United States Department of Education. Orbitals.pdf.

[6] Linus Pauling. *J. Am. Chem. Soc.* **53**, 1367 (1931).

[7] M. Meyyappan Ed. *Carbon Nanotubes: Science and Applications*, CRC press, 2005.

[8] http://invsee.asu.edu/nmodules/Carbonmod/bonding.html

[9] http://www.wellesley.edu/Chemistry/chem120/hybrids.html

[10] McMurray and Fay. *Chemistry* 4$^{\text{th}}$ ed., Prentice-Hall, 2004.

[11] M.A. Prela, G. Popovici, and L.K. Bigelow, Eds. *Handbook of Industrial Diamonds and Diamond Films*, Marcel Dekker, New York, 1997.

[12] Henry Petroski. *The Pencil: A History of Design and Circumstance*, Alfred A. Knopf, 1986.

[13] J.A.L. Robertson. *Decide The Nuclear Issues for Yourself: Nuclear need not be Unclear*, J.A.L. Robertson, 2006.

[14] C. Allardice and E.R. Trapnell. *The First Reactor*, the U.S Department of Energy, 1982.

[15] F.P. Bundy. *Physica A* **156**, 169 (1989).

[16] A.W. Moore, A.R. Ubbelohde, and D.A. Young. *British J. Appl. Phys.* **13**, 393 (1962); L.C.F. Blackman and A.R. Ubbelohde *Proc. Royal Soc.* **A266**, 20 (1962).

[17] Mildred S. Dresselhaus & G. Dresselhaus. "Intercalation compounds of graphite", *Adv. Phys.* **51**, 1-186 (2002).

[18] C. Durkan. Nanoscience and the Engineering Dept., Cambridge, UK; see http://www.eng.cam.ac.uk/∼cd229/.

[19] W.N. Reynolds. *Physical Properties of Graphite*, Great Britain: Elsevier Publishing Company, 1968.

[20] J.C. Charlier and J.P. Michenaud, "First-Principle study of the electronic properties of simple hexagonal graphite" *Phys. Rev. B* **46**, 8: 4531-38 (15 Aug 1992).

[21] A.W. Hull. *Phys. Rev.* **10**, 611 (1917).

[22] J.D. Bernal. *Proc. Phys. Soc.* **A106**, 749 (1924).

[23] R.W.G. Wyckoff. *Crystal Structures*, Vol I, p. 26, John Wiley & Sons, 1963.

[24] M. Dienwiebel, *et.al.* "Superlubricity of Graphite", *Phys. Rev. Lett.* **92**, 12: 126101-4 (2004).

[25] Micheal P. Marder. *Condensed Matter Physics*, John Wiley & Sons, 2000.

[26] F.E. Fujita and K.J. Izui. *J. Phys. Soc. Japan* **16**, 1032 (1961).

[27] P.A. Thower and R.M. Mayer. *Phys. Status Solidi* **47**, 11 (1978).

[28] Glasstone and Sesonke. *Nuclear Reactor Engineering*, Springer, 1994.

[29] C. Kirby, H.W. Kroto and D.R.M. Walton. "The Microwave-Spectrum of cyanohaxatriyne, H-C=C-C=C-C=C-C=N", *J. of Molecular Spectroscopy* **83**, 2: 261-265 (1980).

[30] C.P. Ewels, R.H. Telling, A.A. El-Barbary, M.I. Heggie, and P.R. Briddon. *Phys. Rev. Lett.* **91**, 025505 (2003)

[31] Bernd Eggen, "The Discovery of Fullerenes" SEED foundation, see http://www.seed.slb.com/en/scictr/watch/fullerenes/index.htm.

[32] W.D. Callister. *Material Science and Engineering. An Introduction* , John Wiley & Sons, 2000.

[33] Thomas Alva Edison. U.S. Patent# 470,925, issued March 15, 1892.

[34] Sumio Iijima. *Nature* (London) **354**, 56 (1991).

[35] Ray Baughman. *et. al. Nature* (London) **423**, 703 (2003).

[36] M.S. Dresselhaus. personal quote, Dept. of Physics and the Dept. of Electrical Engineering and Computer Science, MIT.

[37] Teri Wang Odom *et al.* "Scanning Probe Microscopy Studies of Carbon Nanotubes" *Topics in Appl. Phys.* **80**, 173-211 (2001).

[38] J. Han *et. al. Phys. Rev. B* **57** 14983 (1998); J. Han, *Elecrochemical Soc. Proc.* **98**, 8, pp.875-884 (1998); J. Han, *Chem. Phys. Lett.* **282**, 187 (1998); J. Lu and J. Han. *Int. J. High Speed Elec. Sys.* **9**, 101 (1998); J. Han and R. Jaffe, *J. Chem. Phys.*, **108**, 2817 (1998).

[39] K.S. Novoselov, A.K. Geim, S.V. Morozov, D. Jiang, Y. Zhang, S.V. Dubonos, I.V. Grigorieva, A.A. Firsov. "Electric field effect in atomically thin carbon films", *Science* **306**, 666-669 (2004).

[40] Gordon W. Semenoff, "Condensed-matter simulation of a three-dimensional anomaly", *Phys. Rev. Lett.* **53**, 2449-2452 (1984).

[41] E. Fradkin. "Critical behavior of disordered degenerate semiconductors", *Phys. Rev. B* **33**, 3263-3268 (1986).

[42] F.D.M. Haldane. "Model for a quantum Hall effect without Landau levels: Condensed-matter realization of the parity anomaly ", *Phys. Rev. Lett.* **61**, 2015-2018 (1988).

[43] Jonathan Wood. "The excitement of two dimensions (Editorial)", Material Today **10**, 7-8 (July-August 2007).

[44] Alessandra Lanzara. "1-2-3-∞: From single layer graphene to graphite", Condensed Matter Physics Seminar at the University of Texas at Austin, Spring 2007.

[45] Philip Richard Wallace. "The band theory of graphite", *Phy. Rev.* **71**, 622-634 (1947).

[46] Alvin M. Weinberg and Eugene P. Wigner. *Physical Theory of Neutron Chain Reactors*, University of Chicago Press, 1958.

[47] P.R. Wallace and J. LeCaine. "Elementary Approximation in the Theory of Neutron Diffusion", *Nucleonics* **4** 2,pp. 30-35; **4**, 3 pp. 48-67 (1949).

[48] M.M.R. Williams. The development of nuclear reactor theory in the Montreal Laboratory of the National Research Council of Canada (Division of Atomic Energy) 1943-1946, *Prog. Nucl. Energy*, 36, 239-322 (2000).

[49] C.A. Coulson, *Nature, Lond.* **159**, 265 (1947).

[50] F.J. Corbató. Ph.D. Thesis, MIT, Cambridge, Massachusetts (1956); "Proceedings of the Third Conference on Carbon", New York: Pergamon Press, p.173 (1959);

[51] F. Bassani, & G. Pastori Parravicini, *Nuovo Cim. B*, **50** 95 (1967); E. Doni, & G. Pastori Parravicini. *Nouvo Cim. B*, **64**, 117 (1969).

[52] G.S. Painter & D.E. Ellis. *Phys. Rev. B* **1**, 4747 (1970).

[53] Stephanie Reich, Christian Thomsen, & Janina Maultzsch. *Carbon Nanotubes: Basic Concepts and Physical Properties*, Wiley-VCH, January 2004.

[54] J.W. McClure. "Diamagnetism in graphite", *Phys. Rev.* **104**, 666-671 (1956); J.C. Slonczewski & P.R. Weiss "Band structure of graphite." *Phys. Rev.* **109**, 272-279 (1958).

[55] L.G. Johnson & G. Dresselhaus. *Phys. Rev. B* **7**, 2275 (1973).

[56] R.E. Peierls. "Quelques proprietes typiques des corpses solides", *Ann. I.H. Poincare* **5**, 177-222 (1935); L.D. Landau. "Zur Theorie der phasenumwandlungen II", Phys. Z. Sowjetunion **11**, 26-35 (1937).

[57] L.D. Landau and E.M. Lifshitz. *Statistical Physics, Part I*, Pergamon Press, Oxford, 1980.

[58] N.D. Mermin. "Crystalline order in two dimensions", *Phys. Rev.* **176**, 250-254 (1968).

[59] J.A. Venables, G.D.T. Spiller, and M. Hanbucken. "Nucleation and growth of thin films", *Rep. Prog. Phys.* **47**, 399-459 (1984); J.W. Evans, P.A. Thiel, and M.C. Bartelt. "Morphological evolution during epitaxial thin film growth: Formation of 2D islands and 3D mounds", *Sur. Sci. Rep.* **61**, 1-128 (2006).

[60] K.S. Novoselov, D. Jiang, T. Booth, V.V. Khotkevich, S.M. Morozov, Andre K. Geim. "Two-dimensional atomic crystals", *Proc. Natl Acad. Sci. USA* **102**, 10451-10453 (2005).

[61] K.S. Novoselov, Andre K. Geim, S.V. Morozov, D. Jiang, M.I. Katsnelson, I.V. Grigorieva, S.V. Dubonos, A.A. Firsov. "Two-dimensional gas of massless Dirac fermions in graphene", *Nature* **438**, 197-200 (2005).

[62] Yuanbo Zhang, J.W. Tan, H.L. Stormer, Philip Kim. "Experimental observation of the quantum Hall effect and Berry's phase in graphene", *Nature* **438**, 201-204 (2005).

[63] S. Stankovich. *et al.* "Graphene-based composite materials", *Nature* **442**, 282-286 (2006).

[64] Jannik C. Meyer, Andre K. Geim, M.I. Katsnelson, K.S. Novoselov, T.J. Booth, S. Roth."The structure of suspended graphene sheets", *Nature* **446**, 60-63 (2007).

[65] D.R. Nelson, T. Piran, and S. Weinberg. *Statistical Mechanics of Membranes and Surfaces*, World Scientific, Singapore, 2004.

[66] Philip Kim of Columbia University speaking at the Spring 2007 meeting of the European Materials Research Society (EMRS).

[67] Y. Ohashi, T. Hironaka, T. Kubo, and K. Shiiki. "Size Effect in the in-plane electrical resistivity of very thin graphite crystals", *TANSO* 235-238 (1997); Y. Ohashi, T. Hironaka, T. Kubo, and K. Shiiki, *TANSO* 410 (2000).

[68] J.S. Bunch, Y. Yaish, M. Brink, K. Bolotin, & Paul L. McEuen. "Coulomb oscillations and Hall effect in quasi-2D graphite quantum dots", *Nano Lett.* **5**, 287-290 (2005).

[69] Yuanbo Zhang, student of Philip Kim at Columbia University Center for Integrated Science & Engineering. "The Nanopencil: New Methodology for Exploring Conduction Phenomena in Nanoscale Materials", http://www.cise.columbia.edu/nsec/research/nuggets.php?subsection=kim.

[70] A.C. Ferrari, *et al.* "Raman spectrum of graphene and graphene layers", *Phys. Rev. Lett.* **97**, 187401 (2006); A. Gupta, G. Chen, P. Joshi, S. Tadigadapa, & P.C. Eklund, "Raman scattering from high-frequency phonons in supported n-graphene layer films", *Nano Lett.* **6**, 2667-2673 (2006).

[71] Chuhei Oshimayx & Ayato Nagashima. "Ultra-thin epitaxial films of graphite and hexagonal boron nitride on solid surfaces", *J. Phys.: Condens. Matter* **9** 120 (1997)

[72] W.M. Hess & L.L. Ban. *Proc. 6th Int. Congress on Electron Microscopy (Kyoto)* Vol. 1, p 569, 1966; A.E. Karu & M. Beer. *J. Appl. Phys.* **37**, 2179 (1966).

[73] A. Nagashima. Ph.D. Thesis, Waseda University, 1995.

[74] C.F. McConville, D.P. Woodruff, S.D. Kevan, M. Weinert & J.W. Davenport. "Electronic structure of the $(2 \times 2)C$ $\rho 4g$ carbidic phase on Ni100",

Phys. Rev. B **34**, 2199-2206 (1986); E. Rokuta, Y. Hasegawa, A. Itoh, K. Yamashita, T. Tanaka, S. Otani, and C. Oshima. *Surf. Sci.* **97**, 427428 (1999).

[75] T.A. Land, T. Michely, R.J. Behm, J.C. Hemminger, G. Comsa. "STM investigation of single layer graphite structures produced on Pt(111) by hydrocarbon decomposition", *Sur. Sci.* **264**, 261-270 (1992).

[76] A. Nagashima, *et al.* "Electronic states of monolayer graphite formed on TiC(111) surface"' *Surf. Sci.* **291**, 93-98 (1993).

[77] Affonne in 2001, from [44].

[78] A.J. van Bommel, J.E. Crombeen, A. van Tooren. "LEED and Auger electron observations of the SiC(0001) surface", *Surf. Sci.* **48**, 463-472 (1975); I. Forbeaux, J.-M. Themlin, J.M. Debever, "Heteroepitaxial graphite on 6H-SiC(0001): Interface formation through conduction-band electronic structure", *Phys. Rev. B* **58**, 16396-16406 (1998); T. Ohta, A. Bostwick, T. Seyller, K. Horn, E. Rotenberg. "Controlling the electronic structure of bilayer graphene", *Science* **313**, 951 - 954 (2006).

[79] Claire Berger, Zhimin Song, Tianbo Li, Xuebin Li, Asmerom Y. Ogbazghi, Rui Feng, Zhenting Dai, Alexei N. Marchenkov, Edward H. Conrad, Phillip N. First, and Walt A. de Heer. "Ultrathin epitaxial graphite: 2D electron gas properties and a route toward graphene-based nanoelectronics", *J. Phys. Chem. B* **108**, 19912-19916 (2004); Claire Berger, Z.M. Song, X.B. Li, X.S. Wu, N. Brown, C. Naud, D. Mayo, T.B. Li, J. Hass, Alexei N. Marchenkov, Edward H. Conrad, Phillip N. First, Walt A. de Heer. "Electronic confinement and coherence in patterned epitaxial graphene", *Science* **312**, 1191-1196 (2006).

[80] J.M. Blakely & J.C. Shelton, Eds. *Surface Physics of Crystalline Materials*,

New York, 1975; L.C. Isett & J.M. Blakely. *Surf. Sci.* **58**, 397 (1976); M. Eizenberg & J.M. Blakely. *Surf. Sci.* **82**, 228 (1979).

[81] A.V. Bommel, J. Crombeen, and A.V. Tooren, *Surf. Sci.* **48**, 463 (1975).

[82] I. Forbeaux, J.-M. Themlin, and J.-M. Debever. "Heteroepitaxial graphite on $6H$-SiC(0001): Interface formation through conduction-band electronic structure" *Phys. Rev. B* **58**, 16396-16406 (1998); I. Forbeaux, J.M. Themlin, A. Charrier, F. Thibaudau, J.M. Debever, *Appl. Surf. Sci.* **162**, 406412 (2000); A. Charrier, A. Coati, T. Argunova, F. Thibaudau, Y. Garreau, R. Pinchaux, I. Forbeaux, J.M. Debever, M. Sauvage-Simkin, J.M. Themlin, *J. Appl. Phys.* **92**, 5 pp24792484 (2002).

[83] S.Y. Zhou, G.-H. Gweon, & A. Lanzara, "Low energy excitations in graphite: The role of dimensionality and lattice defects", *Annals of Physics* **321**, 1730 (2006).

[84] Walt A. de Heer, Claire Berger, Xiaosong Wu, Phillip N. First, Edward H. Conrad, Xuebin Li, Tianbo Li, Michael Sprinkle, Joanna Hass, Marcin L. Sadowski, Marek Potemski, Gerard Martinez. "Epitaxial graphene", preprint: arxiv.org/abs/0704.0285.

[85] F. Varchon, R. Feng, Joanna Hass, Xuebin Li, B. Ngoc Nguyen, C. Naud, P. Mallet, J.-Y. Veuillen, Claire Berger, Edward H. Conrad, & L. Magaud. "Electronic structure of epitaxial graphene layers on SiC: effect of the substrate.", preprint: cond-mat/0702311.

[86] H. Shioyama. "Cleavage of graphite to graphene", *J. Mat. Sci. Lett.* **20**, 499-500 (2001); Viculis, L. M., Mack, J. J., & R.B. Kaner. "A chemical route to carbon nanoscrolls", *Science* **299**, 1361 (2003).

[87] S. Horiuchi. *et al.* "Single graphene sheet detected in a carbon nanofilm", *Appl. Phys. Lett.* **84**, 2403-2405 (2004).

[88] P. Schaffaütl. *J. prakt Chem.* **21**, 155 (1841).

[89] U. Hoffmann & A. Frenzel. *Z. Elektrochem.* **37**, 613 (1931); A. Schleede and M. Wellmann. *Z. phys. Chem.* **18**, 1 (1932).

[90] A. Krishnan *et al.* "Graphitic cones and the nucleation of curved carbon surfaces", *Nature* **388**, 451-454 (1997); E. Dujardin *et al.* Appl. Phys. Lett. **79**, 2474-2476 (2001).

[91] S. Morozov, K. Novoselov, M. Katsnelson, F. Schedin, D. Jiang, & A.K. Geim. "Strong Suppression of Weak Localization in Graphene", *Phys. Rev. Lett.* **97**, 016801 (2006).

[92] F. Bloch. "The quantum mechanics of electrons in crystal lattices", *Zeitschrift für Physik*, **52**, 555-600 [in German] (1928).

[93] G.H. Wannier. "The structure or electronic exitation levels in insulating crystals", *Physical Review* **52**, 191-197 (1937).

[94] A review article: M. C. Payne, M. P. Teter, D. C. Allan, T. A. Arias, and J. D. Joannopoulos. Iterative minimization techniques for *ab initio* total energy calculations: molecular dynamics and conjugate gradients, *Reviews of Modern Physics* **64**, 1045 (1992).

[95] F. Hund & B. Mrowka. *Ber. verk. Akad. Wiss. Lpz. math. phys. Kl.* **87**, 185, 325 (1937).

[96] S. Reich, J. Maultzsch, C. Thomsen, & P. Ordejón. "Tight-binding description of graphene", *Phys. Rev. B* **66**, 035412 (2002).

[97] Christian Schönenberger. "Bandstructure of Graphene and Carbon Nanotubes: An Exercise in Condensed Matter Physics", online publication as LCAO-NT.pdf.

[98] M. Ali Omar. *Elementary Solid State Physics: Priciples and Applications*, Addison-Wesley Pub. Co., 1975.

[99] Tsuneya Ando. "Exotic electronic and transport properties of graphene", *Physica E* (in press 2007).

[100] Byron P. Roe. *Particle Physics at the New Millennium*, Springer, 1996.

[101] E. McCann, K. Kechedzhi, V.I. Falko, H. Suzuura, T. Ando, & B.L. Altshuler. "Weak-Localization Magnetoresistance and Valley Symmetry in Graphene", *Phys. Rev. Lett.* **97**, 146805 (2006).

[102] P. Esquinazi, D. Spemann, R. Höhne, A. Setzer, K.-H. Han, & T. Butz, "Induced Magnetic Ordering by Proton Irradiation in Graphite" *Phys. Rev. Lett.* **91**, 227201 (2003).

[103] Daniel Huertas-Hernando, F. Guinea, & Arne Brataas. "Spin-orbit coupling in curved graphene, fullerenes, nanotubes, and nanotube caps", *Phys. Rev. B* **74**, 155426 (2006).

[104] G. Dresselhaus and M.S. Dresselhaus. *Phys. Rev.* **140**, A401 (1965).

[105] J.W. McClure and Y. Yafet. *Proc. Fifth Biennial Carbon Conference*, Vol. 1, Pergamon Press, New York (1963).

[106] C.L. Kane and E.J. Mele. *Phys. Rev. Lett.* **95**, 226801 (2005); N.A. Sinitsyn, J.E. Hill, Hongki Min, Jairo Sinova, A.H. MacDonald, *Phys. Rev. Lett.* **97**, 106804 (2006).

[107] G. Dresselhaus, *Phys. Rev.* **100**, 580 (1955).

[108] J.C. Slonczewski. Ph.D. thesis, Rutgers University, 1955.

[109] Hongki Min, J.E. Hill, Nikolas A. Sinitsyn, B.R. Sahu, Leonard Kleinman, and Allan H. MacDonald. " " *Phys. Rev. B* **74** 165310 (2006).

[110] Y. Yao, F. Ye, X.-L. Qi, S.-C. Zhang & Z. Fang, *Phys. Rev. B* **75**, 041401 (R) (2007).

[111] D.N. Sheng, Z.Y. Weng, L. Sheng, F.D.M. Haldane, *Phys. Rev. Lett.* **97** 036808 (2006).

[112] M.V. Berry. *Proc. Roy. Soc. London* **A392**, 45 (1984).

[113] Tsuneya Ando and Takeshi Nakanishi. "Impurity Scattering in Carbon Nanotubes - The Absence of Back Scattering", *J. Phys. Soc. Jpn.* **67**, 1704-1713 (1998); Tsuneya Ando, Takeshi Nakanishi, & Riichiro Saito. "Berry's Phase and Absence of Back Scattering in Carbon Nanotubes",*J. Phys. Soc. Jpn.* **67**, 2857-2862 (1998); Tsuneya Ando, *J. Phys. Soc. Jpn.* **74**, 777 (2005).

[114] Freeman J. Dyson. *J. Math. Phys.* **3**, 140 (1962).

[115] Hidekatsu Suzuura and Tsuneya Ando. "Crossover from Symplectic to Orthogonal Class in a Two-Dimensional Honeycomb Lattice",*Phys. Rev. Lett.* **89**, 266603 (2002).

[116] Tsuneya Ando and Koichi Akimoto."Effects of Short-Range Scatterers on Perfect Channel in Metallic Carbon Nanotubes" *J. Phys. Soc. Jpn.* **73**, 18951901 (2004).

[117] Koichi Akimoto and Tsuneya Ando. "Effects of Trigonal Warping on Perfect Channel in Metallic Carbon Nanotubes",*J. Phys. Soc. Jpn.* **73**, 21942200 (2004).

[118] J. Linderberg. *Arkiv Fysik* **30**, 557 (1965); J. Linderberg & K.V. Makila. *Solid State Comm.* **5**, 353 (1967).

[119] J.W. McClure. *IBM, J. Res. Dev.* **8**, 225 (1964).

[120] Marco Polini, Reza Asgari, Yafis Barlas, Tami Pereg-Barnea, Allan H. MacDonald. "Graphene: A Pseudochiral Fermi Liquid", preprint: arXiv:0704.3786v1 [cond-mat.mes-hall] 28 Apr 2007.

[121] J. Gonzalez, F. Guinea, and M.A.H. Vozmediano. "Marginal-Fermi-liquid behavior from two-dimensional Coulomb interaction", *Phys. Rev. B* **59**, R2474 (1999).

[122] C.L. Kane and E.J. Mele. " Electron Interactions and Scaling Relations for Optical Excitations in Carbon Nanotubes" *Phys. Rev. Lett.* **93**, 197402 (2004).

[123] J.W. McClure. "Diamagnetism in graphite", *Phys. Rev.* **104**, 666-671 (1956); H.J. Fischbeck, *Phys. Status Solidi* **38**, 11 (1970).

[124] Ken-ichi Sasaki, Jie Jiang, Riichiro Saito, Seiichiro Onari, & Yukio Tanaka. "Theory of Superconductivity of Carbon Nanotubes and Graphene", *J. Phys. Soc. Japan* **76**, No. 3, (March 2007).

[125] H. Heersche, P. Jarillo-Herrero, J.B. Oostinga, L.M.K. Vandersypen, & A.F. Morpurgo, *Nature* **446**, 5659 (2007).

[126] Young-Woo Son, Marvin L. Cohen & Steven G. Louie. "Half-metallic graphene nanoribbons", *Nature* **444** 347 (16 November 2006)

[127] M. Fujita, K. Wakabayashi, K. Nakada, and K. Kusakabe, "Peculiar Localized State at Zigzag Graphite Edge", *J. Phys. Soc. Japan* **65**, 7 pp. 1920-1923 (1996).

[128] K. Nakada, M. Fujita, G. Dresselhaus and M.S. Dresselhaus. "Edge state in graphene ribbons: Nanometer size effect and edge shape dependence", *Phys. Rev. B* **54**, 17954-17961 (1996).

[129] Luis Brey and H.A. Fertig. "Electronic states of graphene nanoribbons studied with the Dirac equation", *Phys. Rev. B* **73**, 235411 (2006);

[130] Luis Brey and H.A. Fertig. "Edge states and the quantized Hall effect in graphene", *Phys. Rev. B* **73**, 195408 (2006)

[131] Tsuneya Ando. "Theory of Electronic States and Transport in Carbon Nanotubes", *J. Phys. Soc. Jpn.* **74**, 777 (2005).

[132] Edward McCann and Vladimir I. Fal'ko. "Symmetry of boundary conditions of the Dirac equation for electrons in carbon nanotubes", *J. Phys.:Condens. Matter* **16** 2371 (2004).

[133] Motohiko Ezawa. "Peculiar Band Gap Structure of Graphene Nanoribbons", *Physica Status Solidi (c)* **4** No.2, 489 (2007).

[134] Katsunori Wakabayashi, Yositake Takane, and Manfred Sigrist."Perfectly Conducting Channel and Universality Crossover in Disordered Nano-Graphene Ribbons", preprint cond-mat/0702230v1.

[135] Y. Niimi, T. Matsui, H. Kambara, K. Tagami, M. Tsukada, & Hiroshi Fukuyama. " Scanning tunneling microscopy and spectroscopy of the electronic local density of states of graphite surfaces near monoatomic step edges", *Phys. Rev. B* **73**, 085421 (2006).

[136] Ken-ichi Sasaki, Shuichi Murakami & Riichiro Saito. "Stabilization mechanism of edge states in graphene", *App. Phys. Lett.* **88**, 113110 (2006)

[137] Toshiya Hikihara, Xiao Hu, Hsiu-Hau Lin, Chung-Yu Mou. "Ground-state properties of nanographite systems with zigzag edges", *Phys. Rev. B* **68**, 035432 (2003).

[138] L. Pisani, J.A. Chan, B. Montanari, and N.M. Harrison. "Electronic structure and magnetic properties of graphitic ribbons", *Phys. Rev. B* **75**, 064418 (2007).

[139] J.A. Chan, B. Montanari, J.D. Gale, S.M. Bennington, J.W. Taylor, and N.M. Harrison. " Magnetic properties of polymerized C_60: The influence of defects and hydrogen" *Phys. Rev. B* **70**, 041403(R) (2004).

[140] Elliot H. Lieb. "Two theorems on the Hubbard model", *Phys. Rev. Lett.* **62**, 1201 (1989).

[141] Nguyen Hong Shon and Tsuneya Ando. "Quantum Transport in Two-dimensional Graphite System", *J. Phys. Soc. Jpn.* **67** No. 7 pp. 2421-2429 (1998).

[142] Yisong Zheng and Tsuneya Ando. "Hall conductivity of a two dimensional graphite system", *Phys. Rev. B* **65**, 245420 (2002).

[143] Zhen Yao, Henk W.Ch. Postma, Leon Balents and Cees Dekker. "Carbon nanotube intramolecular junctions", *Nature* **402**, 273 (1999).

[144] Katsunori Wakabayashi, and Kikuo Harigaya. "Magnetic Structure of Nano-Graphite Möbius Ribbon", *J. Phys. Soc. Jpn.* **72** No. 5 pp. 998-1001 (2003)

[145] Melinda Y. Han, Barbaros Özyilmaz, Yuanbo Zhang, & Philip Kim. "Energy Band-Gap Engineering of Graphene Nanoribbons", *Phys. Rev.Lett.* **98**, 206805 (2007).

[146] J. Fernández-Rossier1 , J.J. Palacios, & L. Brey. "Electronic Structure of gated graphene and graphene ribbons", preprint cond-mat/0702473v1.

[147] P.G. Silvestrov and K.B. Efetov. "Electrostatics of Graphene Strips", preprint arXiv:0707.3463v1.

[148] Leonid A. Ponomarenko, Fredrik Schedin, K.S. Novoselov and A. K. Geim, (manuscript in preparation 2007).

[149] Jeroen van den Brink. "Graphene: From strength to strength", *Nature Nanotech.* **2** 199 (April 2007).

[150] Yuanbo Zhang, Joshua P. Small, Michael E.S. Amori, and Philip Kim. " Electric Field Modulation of Galvanomagnetic Properties of Mesoscopic Graphite", *Phys. Rev. Lett.* **94**, 176803 (2005).

[151] Michael J. Gruber and Marianne Leitner. "Spontaneous edge currents for the Dirac equation in two space dimensions", *Lett. Math. Phys.* **75.1** (2004), 25-37.

[152] N. Sinitsyn, J. Hill, H. Min, A.H. MacDonald, Abstract: G46.00001 APS March Meeting (2006).

[153] Ken-ichi Sasaki, Shuichi Murakami & Riichiro Saito. "Gauge Field for Edge State in Graphene", *J. Phys. Soc. Jpn.* **75** 074713 Appendix B (2006).

[154] K. Sengupta, Rahul Roy, & Moitri Maiti. "Spin-Hall effect in triplet chiral superconductors and graphene. ", *Phys. Rev. B* **74**, 094505 (2006).

[155] D.J. Thouless, M. Kohmoto, M.P. Nightingale, and M. den Nijs. "Quantized Hall Conductance in a Two-Dimensional Periodic Potential", *Phys. Rev. Lett.* **49**, 405 (1982).

[156] D.J. Thouless, "Edge voltages and distributed currents in the quantum Hall effect", *Phys. Rev. Lett.* **71**, 1879 (1993); Y. Hatsugai, "Chern number and

edge states in the integer quantum Hall effect", *Phys. Rev. Lett.* **71**, 3697 (1993); H. Schulz-Baldes, J. Kellendonk, T. Richter, "Simultaneous quantization of edge and bulk Hall conductivity", *J. Phys. A: Math. Gen.* **33**, L27 (2000).

[157] C.L. Kane, E.J. Mele, "Z_2 Topological Order and the Quantum Spin Hall Effect" *Phys. Rev. Lett.* **95** 146802 (2005); D.N. Sheng, Z.Y. Weng, L. Sheng, & F.D.M. Haldane, " Quantum Spin-Hall Effect and Topologically Invariant Chern Numbers", *Phys. Rev. Lett.* **97** 036808 (2006); Shuichi Murakami, " Quantum Spin Hall Effect and Enhanced Magnetic Response by Spin-Orbit Coupling", *Phys. Rev. Lett.* **97** 236805 (2006); Takahiro Fukui and Yasuhiro Hatsugai, "Topological aspects of quantum spin Hall effect in graphene: Z_2 topological order and spin Chern number", preprint:cond-mat/0607484 (July 2006); Congjun Wu, B. Andrei Bernevig, & Shou-Cheng Zhang, "Helical Liquid and the Edge of Quantum Spin Hall Systems", *Phys. Rev. Lett.* **96** 106401 (2006).

[158] Liang Fu and C.L. Kane. "Topological insulators with inversion symmetry", *Phys. Rev. B* **76**, 045302 (2007).

[159] M.V. Berry, Proc. R. Soc. London A **392**, 45 (1984); Barry Simon, "Holonomy, the Quantum Adiabatic Theorem, and Berry's Phase", *Phys. Rev. Lett.* **51**, 2167 (1983); M.C. Chang and Q. Niu, "Berry Phase, Hyperorbits, and the Hofstadter's Spectrum ", *Phys. Rev. Lett.* **75**, 1348-1351 (1995).

[160] Eduardo V. Castro, N.M.R. Peres, ; J.M.B. Lopes dos Santos, Antonio H. Castro Neto; Francisco Guinea. "Localized states at zigzag edges of bilayer graphene", preprint arXiv:0707.3819.

Vita

Jason Edward Hill was born in Shelbyville, Tennessee, USA on July 9$^{\text{th}}$, 1978 to Mr. and Mrs. Eddie E. Hill. He obtained a Bs. Sc. in Physics from the Departmert of Physics and Astronomy at Middle Tennesee State University in 2000.

Publications:

N.A. Sinitsyn, J.E. Hill, Hongki Min, Jairo Sinova, A.H. MacDonald, *Phys. Rev. Lett.* **97**, 106804 (2006). Hongki Min, J.E. Hill, N.A. Sinitsyn, B.R. Sahu, Leonard Kleinman, A.H. MacDonald, *Phys. Rev.* B **74**, 165310 (2006). J.E. Hill, Hongki Min, T. Pereg-Barnea, N.A. Sinitsyn, and A.H. MacDonald, "Graphene Ribbon Edge States in Models with Spin-Orbit Coupling", to be published.

Permanent Address: The University of Texas at Austin, Physics Dept.
1 University Station C1600,
Austin, TX 78712

This dissertation was typeset with LaTeX 2_ε[1] by the author.

[1] LaTeX 2_ε is an extension of LaTeX. LaTeX is a collection of macros for TeX. TeX is a trademark of the American Mathematical Society. The macros used in formatting this dissertation were written by Dinesh Das, Department of Computer Sciences, The University of Texas at Austin, and extended by Bert Kay, James A. Bednar, and Ayman El-Khashab.